COUPLED FLUID FLOW AND GEOMECHANICAL MODELING FOR EVALUATING UNCONVENTIONAL WELL PERFORMANCE AND SEISMICITY RISKS

A Dissertation

by

RONGQIANG CHEN

Submitted to the Office of Graduate and Professional Studies of
Texas A&M University
in partial fulfillment of the requirements for the degree of

DOCTOR OF PHILOSOPHY

Chair of Committee,	Akhil Datta-Gupta
Committee Members,	Michael J. King
	Eduardo Gildin
	Debjyoti Banerjee
Head of Department,	Jeff Spath

May 2020

Major Subject: Petroleum Engineering

ABSTRACT

The success of unconventional shale applications in the oil and gas industry often require the understanding of pore pressure and stress/strain changes due to both injection and production. In order to evaluate the complex phenomena associated with both pore pressure and stress change, coupled fluid flow and geomechanical models are necessary, especially in unconventional applications that involved fluid extraction and injection. In this dissertation, we utilize coupled fluid flow and geomechanical simulation to reveal the mechanisms of induced seismicity and to understand the characteristics of hydraulic fractures under different completion designs.

First, we perform a site specific study of the mechanics of induced seismicity in the Azle area, North Texas, using a coupled 3-D fluid flow and poroelastic simulation model. The results show no fluid movement or pressure increase in the crystalline basement, although there is plastic strain accumulation for the weaker elements along the fault in the basement. The accumulation of plastic strain change appears to be caused by the unbalanced loading on different sides of the fault due to the differential in fluid injection and production. Even though the low-permeability faults in the basement are not in pressure communication with the Ellenburger formation, the poroelastic stresses transmitted to the basement can trigger seismicity without elevated pore pressure.

Second, we extend the first part of the dissertation to include a detailed discontinuous fault to model the natural behavior of fault slips. We develop the workflow to couple the finite difference and finite element simulations to explicitly model fault slips

and dissipated energy in the Azle site. The results suggest that the slips can occur at the location where there is no pressure change. The radiated energy from observed seismic events is about 20% of the dissipated energy calculated from the simulation results.

Third, we investigate the impact of cluster spacing on hydraulic fracture design using the Eagle Ford field data. We first identify the fracture geometry by history matching the field injection treatment pressure. Then, we history match the well production data using the rapid Fast Marching Method based flow simulation. The results suggest that most fractures are planar in Eagle Ford because of the high stress anisotropy. The well with tighter cluster spacing tends to develop shorter fractures. The well with tighter cluster spacing has better SRV permeability in the Eagle Ford, leading to better drainage volume and production performance. The tighter cluster spacing completion is more favorable in the Eagle Ford formation because there is minimal fracture interference.

DEDICATION

To my wife, daughters and parents for their endless love and support.

ACKNOWLEDGEMENTS

I would like to thank my committee chair, Dr. Datta-Gupta for his guidance and financial support throughout my Ph.D. study. He has helped me overcome many obstacles in my life and research.

I would like to thank Dr. Michael J. King for his valuable ideas and technical input through my Ph.D. study. I am grateful to my other committee members, Dr. Eduardo Gildin and Dr. Debjyoti Banerjee for their comments and suggestions to improve the quality of this work.

Thanks also go to my friends and colleagues in MCERI group, petroleum department and Texas A&M University for making my time at Texas A&M University a great experience.

Finally, thanks to my wife, daughters, and parents for their encouragement for their endless love and support.

CONTRIBUTORS AND FUNDING SOURCES

Contributors

This work was supervised by a dissertation committee consisting of Professors Akhil Datta-Gupta (advisor), Michael J. King, and Eduardo Gildin of the Department of Petroleum Engineering and Professor Debjyoti Banerjee of the Department of Mechanical Engineering.

The work for Section 2 was in collaboration with Xu Xue and Jaeyoung Park and was published in 2018. Xu contributed to the history matching and Jaeyoung contributed to building the geologic model. The work for Section 3 was in collaboration with Jaeyoung Park. He contributed to building models in ABAQUS. Section 4 of this dissertation was in collaboration with Xu Xue and was published in 2019. He contributed to the fracture geometry history matching.

All other work conducted for this dissertation was completed by the student independently.

Funding Sources

This work was made possible by the financial support of the member companies of the Model Calibration and Efficient Reservoir Imaging (MCERI) consortium.

TABLE OF CONTENTS

Page

LIST OF FIGURES

Page

LIST OF TABLES

Page

1. INTRODUCTION

1.1. Introduction

The success of unconventional shale development in the oil and gas industry often require the understanding of pore pressure and stress/strain changes due to both injection and production. In order to evaluate the complex phenomena associated with both pore pressure and stress change, coupled fluid flow and geomechanical models are necessary, especially in unconventional applications that involved fluid extraction and injection. Common geomechanics related issues include hydraulic fracture propagation, fracture closure, subsidence, reservoir compaction drive, casing failure, wellbore stability, sand production, fault activation, and pore collapse failure. These issues may be difficult to be explained and analyzed using traditional reservoir fluid flow simulation packages. Many of the issues can be better examined with the help of the coupled fluid flow and geomechanical modeling. This dissertation utilizes the coupled fluid flow and geomechanical modeling to address two important challenges in unconventional development: the risks of induced seismicity due to excessive fluid extraction and injection in unconventional plays and the impact of cluster spacing on unconventional well fracture propagation and production performance.

1.2. Induced Seismicity

Induced seismicity typically refers to low magnitude earthquakes as a result of human activity that alters the pore pressure and stress/strain response in the subsurface. Human activities may include: waste water disposal, carbon capture and storage (carbon

dioxide CO_2 sequestration), geothermal energy development, hydraulic fracturing, mining, and hydrocarbon extraction and storage. Different human activities can exist at different phase of the unconventional development. Prior to production, multistage hydraulic fracturing is required to stimulate these low permeability reservoirs. During production, large amount of hydrocarbon is extracted from the reservoir. Meanwhile, significant amount of water is produced along with the hydrocarbon and much of it is injected back to the subsurface using salt water disposal wells.

Ellsworth (2013) mentioned that induced seismicity can be driven by either direct increase of pore pressure along the faults or indirect change in stresses on fault. Figure 1-1 below illustrates different mechanisms of inducing earthquakes. On the left portion of the figure, fluid injection near a fault in a high permeability region increases the pore pressure and lowers the effective stress, leading to fault activation. On the right portion of the figure, an indirect loading due to fluid injection and extraction above the fault causes near fault stress change. The stress alteration could lead to the fault slip without direct hydrologic connection.

The nature of human induced seismicity often involves pore pressure and stress/strain variations in a reservoir system with underlying faults, undergoing fluid injection and extraction. A coupled fluid flow and geomechanical simulation is necessary to fully capture the pressure and stress/strain response and to evaluate the risks of seismicity. This dissertation focuses on evaluating the driving mechanisms of seismicity in the Azle area, north Texas. The previous study by Hornbach et al. (2015) used pore pressure simulation to model the pressure change after production and injection activities

in the Azle area. They conclude that the pore pressure increase from wastewater disposal can be the likely cause for a series of earthquakes along a fault system near Azle, Texas. However, the coupled flow and poroelastic effects as well as the seismic moment magnitude were not included in the study and the majority of seismicity events were recorded in the basement underneath the simulation zone. To evaluate the driving mechanism of seismicity in the Azle area, we build a coupled fluid flow and poroelastic techniques model to study the pressure and stress/strain variations for the overburden, injection and production zone, and the basement. The models are calibrated using injection pressure and seismicity events and the calibrated models are used to evaluate the causal factors of Azle seismicity.

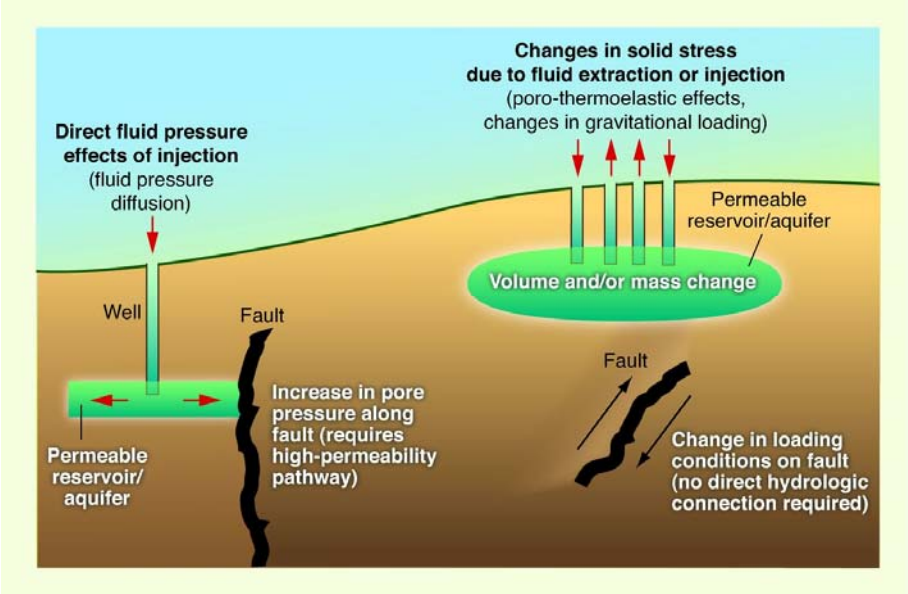

Figure 1-1. Schematic diagram of induced seismicity mechanisms reprinted from Ellsworth (2013).

1.3. Impact of Cluster Spacing

Multi-stage hydraulic fracturing is an integral part of unconventional shale reservoir development. A major outstanding challenge in designing a multi-stage hydraulic fracturing job is to determine the optimal cluster spacing. The current trend of optimal fracturing design has been reducing cluster spacing while increasing fluid and proppant usage (Evans et al., 2018; Pioneer Natural Resources Company, 2018). Many simulation results also suggest an improved well performance using a tighter cluster spacing design (Cipolla et al., 2009; Lolon et al., 2009; Zhu et al., 2017). However, researchers also found that if the cluster spacing is below some threshold values, the well productivity may decrease (Miller et al., 2011). Therefore, it is crucial to understand the characteristics of fracture networks under different cluster spacing designs and their impacts on production performance.

The traditional reservoir fluid flow simulation packages oftentimes have to assume that the fracture geometry is known. In most cases, in the absence of explicit fracture propagation modeling, the fractures are assumed to be planar. Meanwhile, the completion pressure and rate data are not included in the calibration process. To better understand the characteristic of hydraulic fractures, it is important to include coupled flow and geomechanical modeling to simulate complex hydraulic fracture network propagation with multiple propagation branches.

In this dissertation, we utilize Unconventional Fracture Model (UFM) to model the impact of cluster spacing on multi-fractured horizontal well performance using a unique set of Eagle Ford well data. We explicitly model hydraulic fracture propagation and

production for wells using different cluster spacing designs and calibrate the models with both completion and production data. The calibrated models are used to evaluate the characteristics of fracture geometry and production performance under different cluster spacing designs.

2. NEW INSIGHTS INTO THE MECHANISMS OF SEISMICITY IN THE AZLE AREA, NORTH TEXAS[*]

2.1. Overview

We have performed a site specific study of the mechanics of induced seismicity in the Azle area, North Texas, using a coupled 3-D fluid flow and poroelastic simulation model, extending from the overburden into the crystalline basement. The distinguishing feature of this study is that we account for the combined impact of water disposal injection and gas and water production on the pore pressure and stress distribution in this area. The model is calibrated using observed injection well head pressures and the location, timing, and magnitude of seismic events. We utilized a stochastic multi-objective optimization approach to obtain estimated ranges of fluid flow and poroelastic parameters, calibrated to the pressure, rate and seismic event data. Mechanisms for induced seismicity were examined using these calibrated models. The calibrated models show no fluid movement or pressure increase in the crystalline basement, although there is plastic strain accumulation for the weaker elements along the fault in the basement. The accumulation of strain change appears to be caused by the unbalanced loading on different sides of the fault due to the differential in fluid injection and production. Previous studies ignored the produced gas volume, which is almost an order of magnitude larger than the produced water volume under reservoir conditions, and which significantly impacts the pore pressure in the sedimentary formations and the stress distribution in the basement. A

[*] Part of this section is reprinted with permission from "New insights into the mechanisms of seismicity in the Azle area, North Texas" by Chen, R., X. Xue, J. Park, A. Datta-Gupta, and M. J. King,. (2020), paper published in Geophysics, 85, EN1-EN15. Copyright [2020] Society of Exploration Geophysicists.

quantitative analysis shows that the poroelastic stress changes dominate in the basement with no noticeable change in pore pressure. Even though the low-permeability faults in the basement are not in pressure communication with the Ellenburger formation, the poroelastic stresses transmitted to the basement can trigger seismicity without elevated pore pressure.

2.2. Introduction

The number of seismic events in the Fort Worth Basin has been increasing since 2007. Near the Azle area, a cluster of seismic events were recorded from late 2013 to early 2014, including two widely felt Mw3.6 events. No significant earthquake had been felt prior to 2007 based on more than 40 years of seismic monitoring (Frohlich et al., 2011; Frohlich et al., 2016). There have been several studies to investigate the cause of the more recent seismic events and many of them conclude that the injection of wastewater into the subsurface near faults and reactivation of the faults are the primary contributing factors (Frohlich et al., 2011; Gono et al., 2015; Hornbach et al., 2015; Frohlich et al., 2016; Schwab et al., 2017). Gono et al. (2015) investigated the relationship between disposal water injection and seismic events in the Fort Worth Basin. Using single phase fluid flow simulation and historical earthquake data, they found that there is a spatial and temporal correlation between pore pressure increase and seismic events. Hornbach et al. (2015) considered several factors that could lead to seismic events near Azle such as lake-level variations, natural tectonic stress and stress changes associated with oil and gas production activities. Hornbach et al. (2015) constructed single phase flow models for the Ellenburger

formation, a shallowly dipping dolomitic limestone that overlies the crystalline basement and has been used for disposal of large volumes of saline oilfield wastewater (Sullivan et al., 2006; Pollastro et al., 2007b). They observed that with different parameter combinations excess pore pressure at the fault could range from 0.01MPa to 0.14MPa. The predicted pore pressure increases at the fault were found to be sufficient to trigger earthquakes when faults are critically stressed (Reasenberg and Simpson, 1992; Stein, 1999).

Previous studies at Azle did not solve the coupled fluid flow and geomechanical (poroelastic stress) equations to explicitly model the plastic deformation and the resulting implications for fault activation and induced seismicity, though there have been previous efforts to include geomechanical effects to analyze the potential linkage between fluid injection and seismic events. Fan et al. (2016) investigated a Mw4.8 earthquake near Timpson, east Texas, relating the event to geomechanical response of the adjacent fault after nearby wastewater injection. They conducted coupled fluid flow and poroelastic simulations to compute stress and pore pressure along the fault associated with the wastewater injection. Based on the Mohr-Coulomb failure criteria, they assessed fault slip with the estimated in-situ stress magnitude and direction, fault strike and dip, and permeability of the layer where fluid was injected. Chang and Yoon (2018) performed 3-D fully coupled poroelastic modeling of induced seismicity along multiple faults to predict magnitude, rate, and location of potential seismic events. They concluded that the use of 3-D coupled poroelastic modeling helps reduce the uncertainty in the seismic hazard prediction by considering hydraulic and mechanical interaction between faults and

bounding formations. Zhai and Shirzaei (2018) used a basin-wide fluid flow and geomechanical model to investigate seismic hazards in the Barnett shale, Texas. They related the Coulomb failure stress change with seismicity rate and used it as a representation of seismic hazard. They concluded that the contribution of poroelastic stresses to Coulomb failure stress change is around 10% of that of pore pressure. However, the model was not calibrated with historical pressure data and the stress change from gas production was not considered. The physical mechanisms behind induced seismicity on faults have also been investigated and discussed in several previous studies (Segall, 1989; Segall et al., 1994; Ellsworth, 2013; Segall and Lu, 2015; Chang and Segall, 2016a; Chang and Segall, 2016b).

In this study, we focus on the seismicity in the Azle area in North Texas, which experienced a series of seismic events from November 2013 through April 2014. We utilize coupled fluid flow and geomechanical simulation to numerically solve for the 3-D stress/strain field and the pore pressure distribution. In our study, for the first time we account for the reservoir withdrawal created by the gas production. We also calibrate the simulation model to observed injection well pressure data as well as the magnitude and timing of the seismic events, to constrain the range of uncertain fluid flow and poroelastic parameters. We utilize a stochastic multi-objective model calibration which yields an ensemble of models that are consistent with the historical data. All of these models seem to indicate that unbalanced loading on different sides of the critically stressed fault in the crystalline basement resulted in accumulation of plastic strain change, leading to stress changes capable of causing the observed earthquakes in the area.

2.3. Methodology

2.3.1. Overall Workflow

In this study, we focus on the seismicity in the Azle area in North Texas. The events occurred along two NE-striking, steeply dipping conjugate faults. To assess potential linkage between the seismic events and the nearby oil and gas field operations, we built a 3-D coupled fluid flow and geomechanical model consisting of the overburden, the Marble Falls, the Barnett, the Ellenburger and the crystalline basement. In the simulation model, we include two injection wells in the Ellenburger and 70 production wells in the Barnett, a shale gas producing formation. A stochastic multi-objective optimization is used to generate an ensemble of models calibrated with injection well pressure data and seismic events (see Appendix A for details). The calibrated models are then used to analyze the mechanisms of induced seismicity at the Azle site. The overall workflow is illustrated in Figure 2-1.

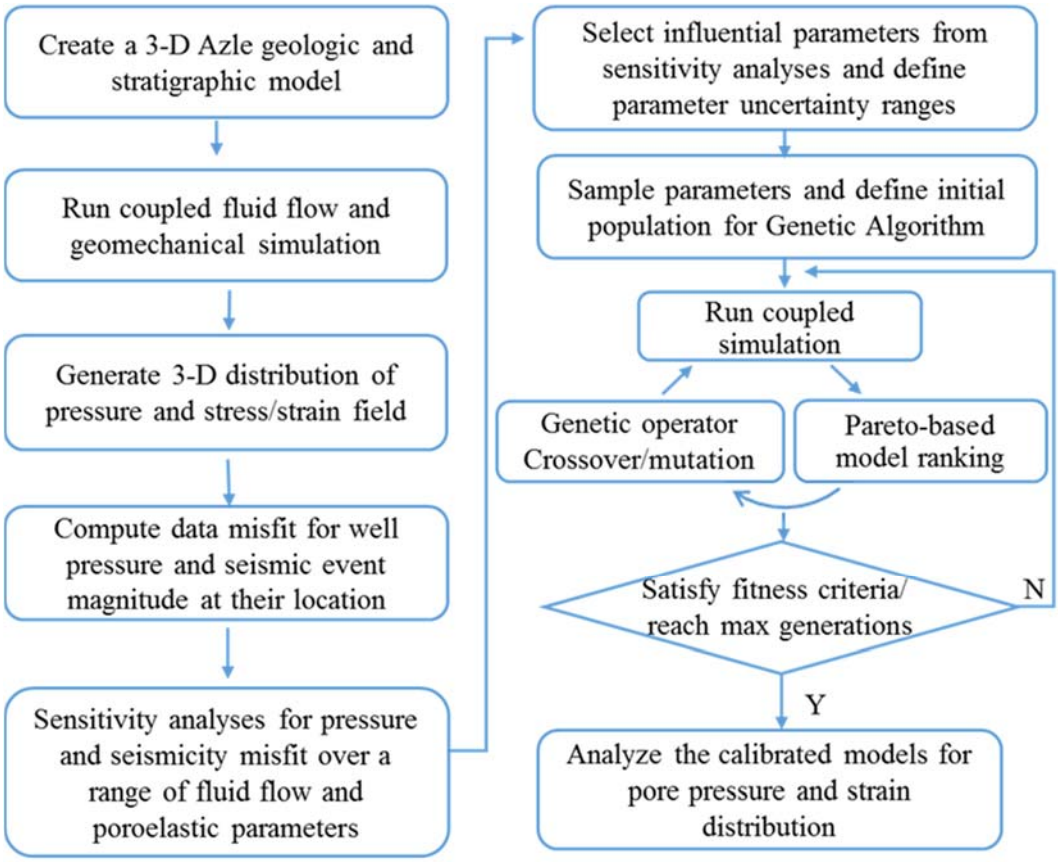

Figure 2-1. Workflow for Azle seismicity study using coupled flow and geomechanical modeling.

2.3.2. Model Data Sources

In order to understand the mechanism of seismicity in the Azle area, our study integrates a wide range of data to build and calibrate the 3-D coupled fluid flow and geomechanical model. The geologic model is built following the previous studies (Hornbach et al., 2015; Hennings et al., 2016). The faults were constructed using fault interpretations of Hornbach et al. (2015) and the public records from the Railroad Commission of Texas (Railroad Commission of Texas, 2015a, b). The dynamic injection data of rate and pressure of the two SWD disposal wells is available through the H-10

form in the Railroad Commission of Texas website (Railroad Commission of Texas, 2018a). As in the previous study of Hornbach et al. (2015), our study includes only two SWD disposal wells. This is justified because an estimate of the average pressure change in the Azle area due to the two local injectors is found to be almost an order of magnitude higher than the basin scale average pressure change from all the injectors based on a flowing material balance calculation (Dake, 1983; Hornbach et al., 2016).

The dynamic production data consists of gas and water production from 70 producing wells. The gas production data is available in the Railroad Commission of Texas website (Railroad Commission of Texas, 2018b). The water production data is obtained from the "DrillingInfo" data base (Drillinginfo, 2018). Seismic event data including the event time, magnitude, hypocenter location, as well as the location uncertainty are obtained from SMU catalogs (Hornbach et al., 2015; DeShon et al., 2018).

2.3.3. Geologic Model: Background

The Azle geologic and fault model used in this study follows the previous study by Hornbach et al. (2015) with additional details from the Texas Bureau of Economic Geology (Hennings et al., 2016). We have extended the geologic model to include the overburden and the crystalline basement where most of the earthquakes have occurred. The structural model consists of two steeply dipping conjugate faults around which most of the earthquakes were recorded.

Faults in the region were constrained by an integrating analysis of stratigraphic mapping, structural interpretation, earthquake hypocenters (Hornbach et al., 2015), and

review of public records from the Railroad Commission of Texas (Railroad Commission of Texas 2015). Our model includes two NE-striking normal faults in the model: Azle and Azle Antithetic. These faults are part of the Llano Fault System in the Fort Worth Basin as described by Ewing (1991). The lateral extent, strike, and general dip of the faults was constrained by 3-D interpretation and earthquake hypocenter location.

The Newark East Gas Field (NEGF) is the major gas-producing field in the Fort Worth Basin. Hydraulic fracturing is routinely applied to produce gas from the low permeability Barnett shale. Some hydraulically fractured wells can unintentionally produce significant volumes of water from the underlying high permeability Ellenburger formation (Hornbach et al., 2016). Produced water is reinjected through disposal wells completed in the Ellenburger formation. Low permeability Precambrian granite basement underlies the Ellenburger and the majority of the Azle earthquake events have occurred in this unit. The seismic events ($Mw \geq 2$) are shown in Figure 2-2. Out of 32 seismic events, 25 events are adjacent to the faults, lying within the hypocenter uncertainty range provided by the SMU seismic catalog (Hornbach et al., 2015; DeShon et al., 2018). Additional seismic stations deployed by SMU were intended to reduce the location uncertainty after the early 27 earthquakes near the Azle were reported by the United States Geological Survey (USGS). A schematic of the 3-D geologic model is shown in Figure 2-2. In this layer-cake Azle model, fluid flow and poroelastic properties are considered uniform within each zone except at the fault cells.

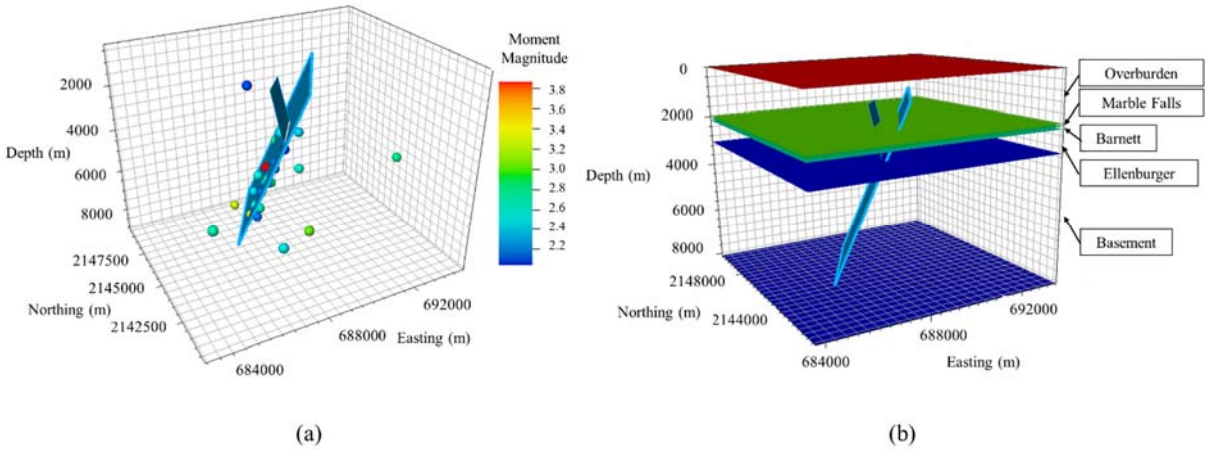

Figure 2-2. (a) Azle area fault location and the locations of the earthquake events (Mw≥2). (b) A schematic of the Azle geologic model.

Table 2.1 shows the fluid flow and poroelastic properties for each zone used in the base case model along with their corresponding sources. Figure 2-3 is the Mohr circle showing the stress state (Lund Snee and Zoback, 2016) and the Mohr-Coulomb failure envelope of the fault for the base case at a depth of 3048 m, which is the top of the basement. As noted by Lund Snee and Zoback (2016) and Quinones et al. (2018), the fault is nearly critically stressed.

Table 2.1. Fluid flow and poroelastic properties for the Azle base case model.

	Overburden	Marble Falls	Barnett	Ellenburger	Basement	Fault	Reference
Permeability (mD)	190	0.01	1.00E-05	30	1.00E-04	1.00E-03	(Hornbach et al., 2015)
Porosity	0.2	0.2	0.06	0.055	0.05	Same as formation	
Pore Pressure	23082 kPa @ 2046 m						(Railroad Commission of Texas, 2015b)
Effective Vertical Stress Gradient	14.7 kPa/m						(Simpson, 1997; Lund Snee and Zoback, 2016)
Effective Minimum Horizontal Stress Gradient	4.5 kPa/m						
Anderson Fault Parameter, A_Φ	0.74						
Direction of Horizontal Stress	N28.8E						
Young's Modulus (kPa)	1.44E+07	6.00E+07	4.00E+07	6.00E+07	4.30E+07	4.00E+07	(Wang, 2000; Tutuncu, 2010; Rutqvist et al., 2013; Sone and Zoback, 2013)
Poisson's Ratio	0.2	0.2	0.23	0.2	0.27	0.25	
Cohesion (kPa)	2.00E+04	2.00E+04	2.00E+04	2.00E+04	2.00E+04	1.00E+03	
Friction Angle (Deg)	30	30	30	30	30	30	

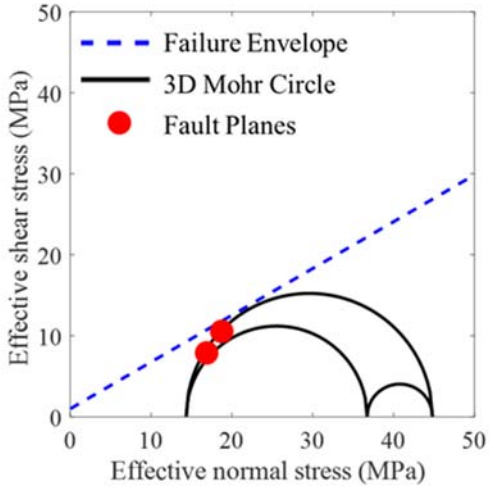

Figure 2-3. Initial stress state and the Mohr-Coulomb failure envelope for the base case Azle model.

2.3.4. Forward Simulation

A coupled fluid flow and geomechnical simulation model is used to compute the evolution of the 3D pressure and stress/strain fields in the Azle area during the period of fluid injection and production. The Azle simulation model consists of uniform grid cells (160m x 160m) areally, and varying cell dimensions vertically, with higher resolution in the Barnett and Ellenburger formations. The model has one layer for the overburden and one layer for the Marble Falls to provide geomechanical loading to the reservoir, five layers for the Barnett, which is the producing zone, five layers for the Ellenburger, which is the injection zone, and ten layers for the crystalline basement where the majority of the earthquake events occurred. The overburden has the lowest vertical resolution of 2000m and the Barnett has the highest vertical resolution of 23m. There are two tilted faults intersecting just below the Ellenburger and the major fault extends down to the bottom of the basement Figure 2-2. The fault cells have distinct fluid flow and poroelastic properties

from the adjacent formations Table 2.1. The base case simulation model consists of 70 producers completed in the Barnett and two SWD disposal wells completed in the Ellenburger (Figure 2-4) with a total simulation study period of 12 years. Hydraulic fractures create high permeability regions near the producers, so the permeability near the producers is enhanced to honor the historical production rates at the wells. The injected wastewater volume and gas production are available in the Railroad Commission of Texas website (Railroad Commission of Texas, 2018b). The water production data is from the "DrillingInfo" data base (Drillinginfo, 2018). The water production data were cross-checked with the data provided by the operator (XTO) for selected wells to ensure accuracy.

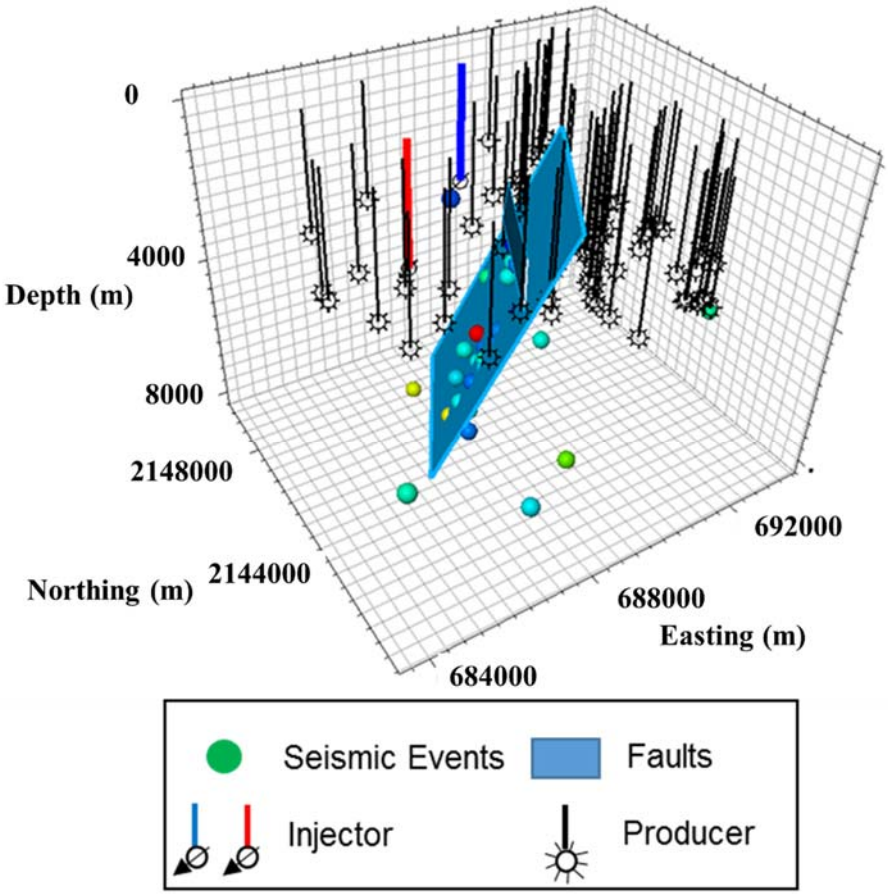

Figure 2-4. Injection/production well locations and seismic event locations with respect to the Azle faults.

Our forward model utilizes coupled fluid flow and poroelastic simulation to numerically solve the continuity and the momentum balance equations in a sequential manner. The continuity equation solves for the formation pore pressure and is given by:

$$\frac{d}{dt}\left[\phi\rho_f\left(1-\varepsilon_v\right)\right]-\nabla\bullet\left[\rho_f\frac{k}{\mu_f}\left(\nabla \mathrm{p}-\rho_f g\nabla \mathrm{D}\right)\right]=Q_f\ , \tag{2.1}$$

where ϕ is the porosity, ρ_f is the density of fluid, ε_v is the volumetric strain, k is the permeability, μ_f is the fluid viscosity, g is the gravitational constant, D is the depth from a reference pressure datum and Q_f is the mass source term.

The momentum balance equation solves for formation displacement and can be expressed as:

$$\nabla\left[\mathbf{C}:\frac{1}{2}\left(\nabla\mathbf{u}+\left(\nabla\mathbf{u}\right)^{T}\right)\right]=-\nabla\left[\alpha\mathrm{p}\right]\mathbf{I}+\mathbf{B}, \tag{2.2}$$

where **C** is the tangential stiffness tensor, **u** is the displacement, α is the Boit's number, p is pressure, **I** is the identity matrix, and **B** is the body force.

The momentum balance equation is solved using a finite-element scheme while the continuity equation is solved using a finite-difference scheme. The two solutions are sequentially coupled (Computer Modeling Group, 2016). We obtain the 3-D stress/strain and pressure distribution for the entire simulation domain at each simulation time step.

The forward simulation model is calibrated to match the observed wellhead pressure data and the magnitude and timing of the seismic events to reduce the range of the uncertain parameters. The simulated well bottom hole pressure (BHP) can be directly obtained from flow simulation and compared with the calculated BHP obtained from the measured wellhead pressure. This requires converting the well head pressure data to the bottom hole conditions, a routine calculations in petroleum reservoir engineering (Govier and Aziz, 1972; Beggs and Brill, 1973; Chen, 1979; Taitel et al., 1982; Bradley, 1987; Ansari et al., 1990; Economides et al., 2013). The details of this calculation are in Appendix B.

The poroelastic simulation calculation checks the failure status for each cell in the 3-D model at every time step and accumulates the plastic strain after the rock failure. The plastic strain/deformation is the strain after a cell reaches Mohr-Coulomb failure and is calculated using the generalized plasticity model based on Mohr-Coulomb yield surface (Vermeer and De Borst, 1984; Computer Modeling Group, 2016). All of the accumulated plastic strains are then used to calculate the seismic moment magnitude (Sanz et al., 2015; Castiñeira et al., 2016; Lele et al., 2016; Park et al., 2016). The computed seismic moment magnitude is compared with the observed seismic event magnitudes during model calibration. The seismic moment tensor is used to model the seismicity induced by fault activation. The seismic moment tensor is represented by the following equation (Aki and Richards, 2002)

$$M_{pq} = \int_V c_{pqrs} \Delta e_{rs} dV \,, \tag{2.3}$$

where the repeated indices indicate summation. Here, c_{pqrs} is the stiffness tensor or the elastic modulus tensor consisting of Young's modulus and Poisson's ratio. Note that during model calibration, we adjust the Young's modulus and Poisson's ratio. Thus, the elastic tensor dynamically evolves. Δe_{rs} is the change of plastic strain by deformation, which is accumulated after a cell reaches the Mohr-Coulomb failure criteria. The L_2 norm of the seismic moment tensor is used to obtain the intensity of the seismic moment, M_0 (Dahm and Krüger, 2014)

$$M_0 = \left\| M_{pq} \right\|_{L_2} . \tag{2.4}$$

The seismic moment magnitude is calculated as follows (Kanamori, 1977)

$$M_w = \frac{\log M_0 - 16.1}{1.5} + 4.667 \,. \tag{2.5}$$

The observed wellhead pressure and seismic data are matched by adjusting fluid flow and poroelastic properties using a multi-objective stochastic optimization method. The details of the model calibration are discussed in the next section and also in Appendix A.

A distinctive feature in the current model compared to previous studies is the inclusion of gas production. Previous studies incorporated the pressure reduction due to brine production from the Ellenburger formation. However, hydrocarbon gas production can contribute to greater reservoir depletion compared to the brine production. The brine is produced from the Ellenburger formation because the hydraulic fractures propagate through the Barnett into the Ellenburger formation (Hornbach et al., 2015). Especially in regions where the Viola shale is absent below the Barnett shale, as in the Azle area, (Pollastro et al., 2007b; Loucks et al., 2009), the producers in the Barnett are in direct pressure communication with the Ellenburger formation. Our results show that ignoring the gas production leads to significant under-estimation of the reservoir fluid withdrawal and reservoir pressure depletion. We convert the surface gas production to bottom hole conditions and use the equivalent reservoir fluid withdrawal rates. The details are presented in Appendix C. Because the pore pressure is primarily impacted by the total reservoir fluid withdrawal of all phases, the equivalent reservoir fluid withdrawal rates help ensure that the material balance is preserved in reservoir conditions for both single-phase and multi-phase flow simulations. Figure 2-5 shows the water production, gas production and the total fluid withdrawal under reservoir conditions. Note that the

reservoir volume of the produced gas is almost one order of magnitude larger than the produced water volume.

It is worth pointing out that the coupled simulation model used here only requires specification of the total fluid withdrawal rate while the individual layer allocations are computed based on the layer productivity indices (Computer Modeling Group, 2016).

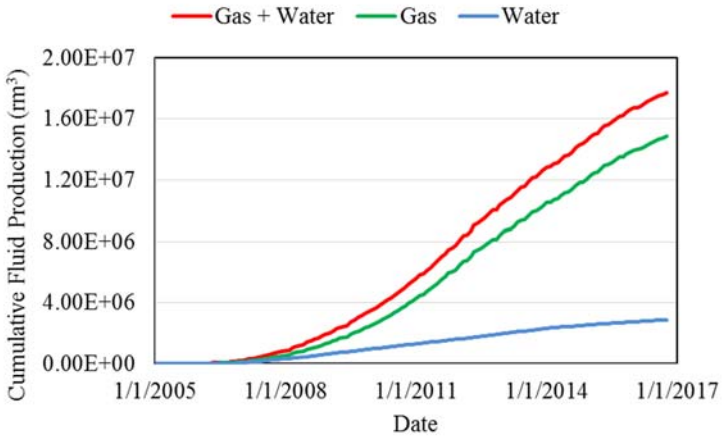

Figure 2-5. Produced fluid volumes used in this study (at reservoir conditions).

2.3.5. Model Calibration and Multi-objective Optimization

In this study, we minimize two objective functions for model calibration: injector bottom hole pressure (BHP) misfit and seismic moment magnitude misfit at their respective locations and times.

The injector BHP misfit is calculated using the following equation:

$$obj_{BHP} = \log\left(\sum_{j=1}^{Nwell} \sqrt{\sum_{i=1}^{Ntime} \left(BHP_{i,j}^{obs} - BHP_{i,j}^{cal}\right)^2}\right), \tag{2.6}$$

where Nwell is the total number of history matching wells, Ntime is the total number of data points for each well, superscript obs indicates observed data, and superscript cal indicates calculated value from the simulation.

The seismic moment magnitude misfit calculation is the difference between seismic moment magnitude based on the plastic strain after rock failure, and the observed seismic event magnitude at the time and location of the observed seismic event. It is given by:

$$obj_{magnitude} = \sqrt{\sum_{i=1}^{Nevent} (Mw_i^{obs} - Mw_i^{cal})^2}\ , \tag{2.7}$$

where N_{event} is the total number of seismic events being matched, Mw_i^{obs} is the observed seismic moment magnitude of event i, and Mw_i^{cal} is the calculated seismic moment magnitude from the simulation within a search radius of seismic event i. Here the search radius is given by the average earthquake epicenter uncertainty in the SMU catalog (Hornbach et al., 2015; DeShon et al., 2018). For the events reported in the SMU catalog, the mean epicenter major axes length is 570±362 m, minor axes length is 310±228 m and the depth uncertainty is 346±171m. At each simulation time step, we check every grid cell within the search radius of each observed seismic event to determine whether it meets the Mohr-Coulomb failure criteria. Once a cell fails, plastic strain accumulation starts for this cell. The cell with the minimum misfit within the search radius of each observed seismic event is used for the objective function calculation. We assume that all the plastic strain within the cell may release seismically as one single event which may not always be the case (Bourouis and Bernard, 2007; Guglielmi et al., 2015; McGarr and Barbour, 2017). We use this approach as there is no specific data available for the Azle area to distinguish between seismic and aseismic deformation.

To calibrate the forward model using available injector pressure and seismic moment data, we use a Pareto-based stochastic multi-objective history matching algorithm.

Instead of aggregating different misfit functions, the Pareto-based approach ranks the models based on the concept of dominance (see Appendix A). For a minimization problem involving *n* objectives defined by objective functions *fn*, solution *a* dominates solution *b* if all objectives represented by *a* are not greater than those of *b*, and at least one objective of *a* is strictly smaller than the corresponding objective of *b.* The genetic algorithm (Goldberg, 1989) is used for updating the uncertain parameters during the calibration. The genetic algorithm (GA) is one of the evolutionary methods for solving optimization problems. It imitates biological principles of evolution: natural selection and survival of the fittest. The evolution starts from a population of randomly generated models with uncertain parameters sampled from a pre-specified uniform distribution defined by their respective minimum and maximum values. In each generation, the fitness of every model (the model rank in our study) in the population is evaluated. Multiple models are stochastically selected from the current population (based on their fitness), and modified (recombined and possibly randomly mutated) to form a new population. The new population is then used in the next iteration of the algorithm. Commonly, the algorithm terminates when either the maximum number of generations is reached or a satisfactory fitness level is attained (Yin et al. 2011). Thus, multiple plausible parameter combinations are generated with low rank populations that match the historical data within a specified tolerance.

2.4. Results: Parameter Sensitivity Analysis and History Matching

2.4.1. Parameter Sensitivity Analysis

The sensitivity analysis involves forward simulations by changing one parameter at a time to identify the key parameters affecting the objective functions for bottom hole pressure and seismic moment magnitude (Yin et al., 2011). The parameters with strong influence on the objective functions are kept for model calibration and the less sensitive parameters are discarded.

Figure 2-6 shows a "tornado plot" illustrating the sensitivity of injector BHP misfit to various parameters. As expected, reservoir fluid flow parameters such as permeability and permeability anisotropy (vertical/horizontal) are the most influential parameters on the list. BHP misfit is also impacted by the Ellenburger poroelastic properties such as the Young's modulus and Poisson's ratio because of their effects on the Ellenburger formation compressibility. The importance of the vertical permeability indicates the impact of pressure communication between the disposal and production intervals. The permeabilities of the Barnett shale and the crystalline basement are very low for the base case. Thus, the injector BHP is not significantly impacted by their permeability, porosity and poroelastic properties. From this sensitivity analysis, permeability anisotropy, Ellenburger permeability, Young's modulus, and Poisson's ratio are identified as the primary tuning parameters for BHP calibration.

Figure 2-7 shows a "tornado plot" illustrating the sensitivity of the misfit between the simulated seismic moment magnitude and the observed earthquake magnitude. Minimum effective horizontal stress and fault cohesion are the most sensitive parameters

here because these determine how close the faults are to a critically stressed state based on the Mohr-Coulomb criteria. The fault Poisson's ratio is important because it is used to construct the stiffness matrix for the moment tensor calculations. The basement permeability is in the nano-Darcy range and there is very little pressure communication from above. Hence, the seismic moment magnitude misfit is mostly affected by its poroelastic parameters. Both the pressure and seismic moment magnitude misfits show very little sensitivity to the fault permeability.

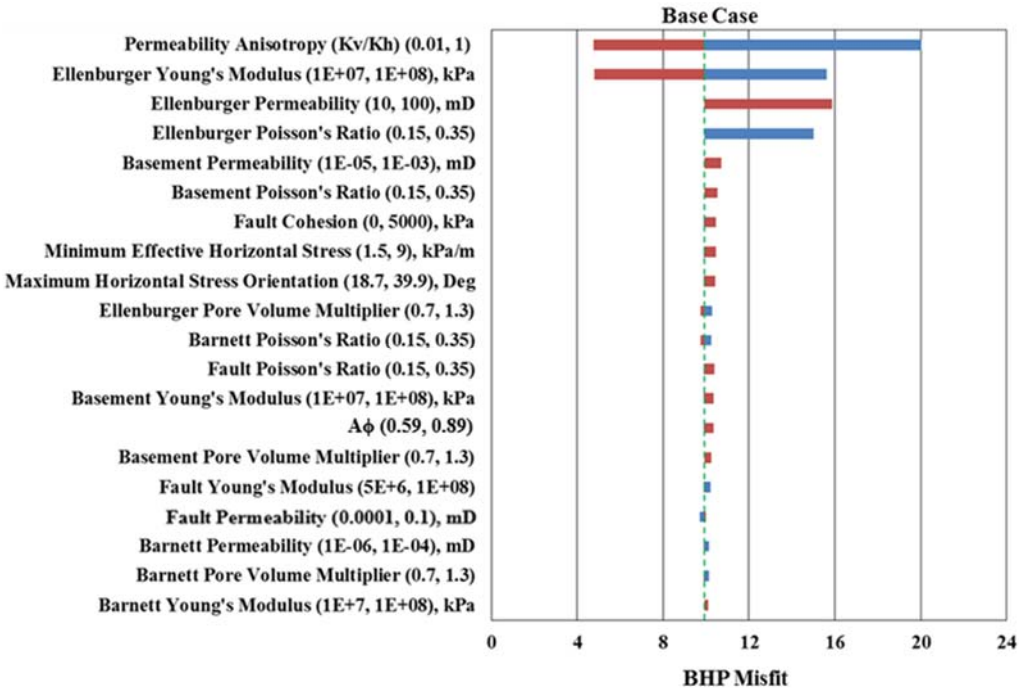

Figure 2-6. Sensitivity of injector bottom hole pressure misfit to various fluid flow and poroelastic parameters and their ranges (in parenthesis).

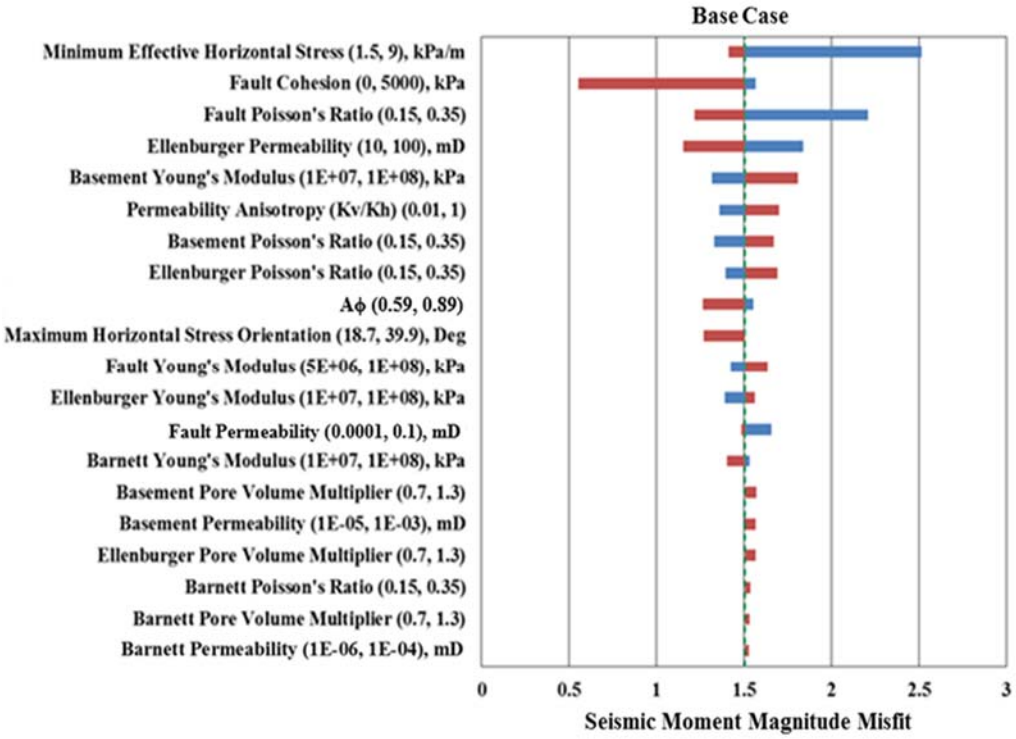

Figure 2-7. Sensitivity of the seismic moment magnitude misfit to various fluid flow and poroelastic parameters and their ranges (in parenthesis).

2.4.2. Multi-objective History Matching and Parameter Uncertainty

Table 2.2 shows the poroelastic and fluid flow parameters with strong influence on objective functions based on the sensitivity analysis and their corresponding ranges. These parameters will be calibrated to match the observed injector bottom hole pressure and the seismic moment magnitude. Most poroelastic properties have relatively high uncertainty ranges because of limited data or prior knowledge. This makes the model calibration imperative for reducing the parameter ranges. Figure 2-8a shows the results of the multi-objective history matching using the genetic algorithm. As expected, the generation 1 population members are scattered to explore the parameter space while the

generation 5 population members move towards the bottom left indicating misfit reduction for both BHP and seismic moment magnitude. We also see the formation of a 'Pareto front' between BHP and seismic magnitude misfits with multiple generations displaying the trade-off between the misfit functions. Figure 2-8b shows the quality of seismic moment magnitude match; the rank 1 matches are moving toward the unit slope line although with some degree of scatter. However, several of the rank 1 matches show lower calculated seismic moment magnitude compared to the observed seismic magnitude especially for the ($Mw \geq 3$) seismic events. This is consistent with the previous findings that the faults are initially in a critically stressed state and already in a state of plasticity (Zoback et al., 2012; Hornbach et al., 2015; Lund Snee and Zoback, 2016; Quinones et al., 2018; Zhai and Shirzaei, 2018). We did not account for any initial strain accumulation in the faults and this might introduce biases in the model calibration. However, the methodology of multi-objective optimization allows us to explore what information may be discerned from the data, despite these short-comings. Further, the use of coupled fluid flow and geomechanical calculation, including Mohr-Coulomb failure, allows us to explore these coupled mechanisms. Figure 2-8c and 2.9d show the BHP history matching result for Injector 1 and Injector 2, respectively. All the rank 1 models show good agreement with historical pressure data and a decreasing pressure trend over the injection period. The intent of the model calibration is to be as quantitative as possible and the ensemble based approach provides error bounds in the parameter estimates. However, the goal here is not to match the observed pressure data exactly given the uncertainty in the field data. Instead,

the calibration results in an ensemble of models that match both the seismic and pressure data adequately.

Table 2.2. History matching parameters and ranges.

	Description	Parameter	Base	Low	High
Poroelastic Properties	Ellenburger Young's Modulus (kPa)	YOUNGE	6.00E+07	1.00E+07	1.00E+08
	Basement Young's Modulus (kPa)	YOUNGB	4.30E+07	1.00E+07	1.00E+08
	Fault Young's Modulus (kPa)	YOUNGF	4.00E+07	1.00E+07	1.00E+08
	Fault Cohesion (kPa)	COHEF	1000	0	5000
	Ellenburger Poisson's Ratio	POISSE	0.27	0.15	0.35
	Fault Poisson's Ratio	POISSF	0.25	0.15	0.35
	Effective Minimum Horizontal Stress	Shmin	4.5	1.5	9
Fluid Flow Properties	Ellenburger Pore Volume Multiplier	PVE	1	0.7	1.3
	Ellenburger Permeability Multiplier	PERME	1	0.1	10
	Permeability Anisotropy	Kv/Kh	0.1	0.01	0.2

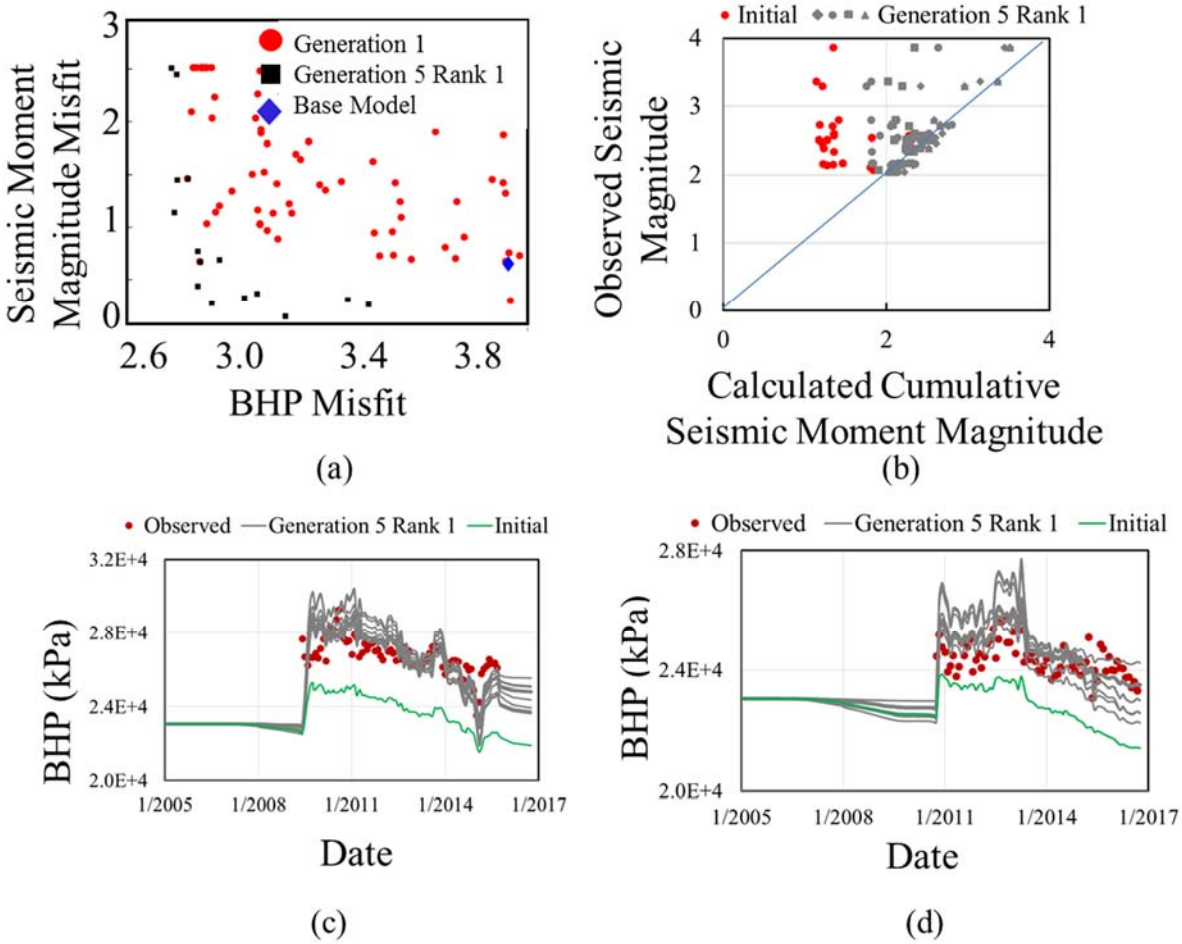

Figure 2-8. Multi-objective history matching results. (a) Trade-off between seismic moment magnitude and BHP misfit. (b) Seismic moment magnitude match: initial versus generation 5 rank 1. (c) Injector 1 bottom hole pressure match: initial versus generation 5 rank 1. (d) Injector 2 bottom hole pressure match: initial versus generation 5 rank 1.

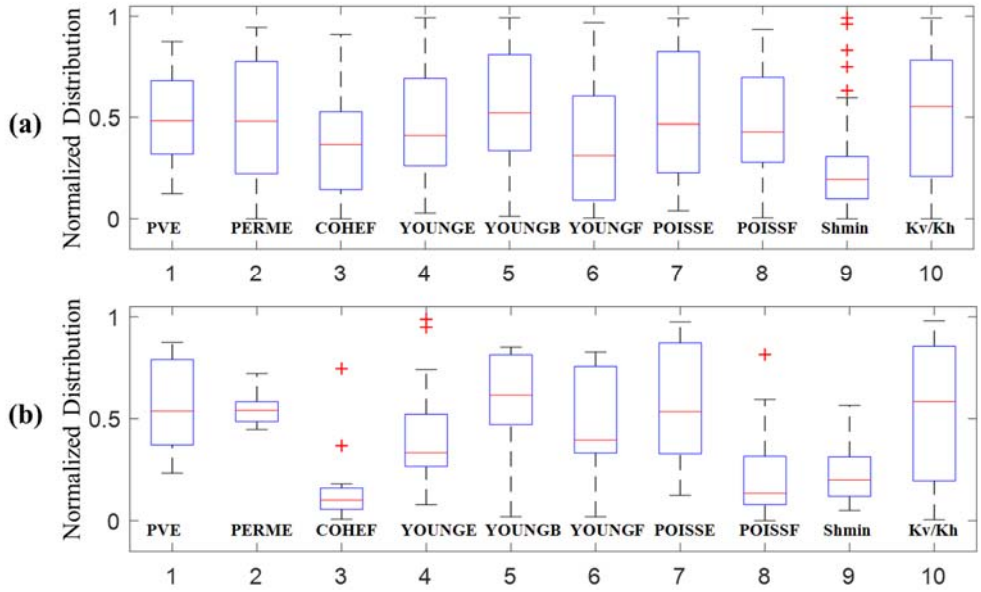

Figure 2-9. History match parameter ranges (a) prior distribution (b) posterior distribution. PVE: Ellenburger pore volume multiplier, PERME: Ellenburger permeability, COHEF: fault cohesion, YOUNGE: Ellenburger Young's modulus, YOUNGB: basement Young's modulus, YOUNGF: fault Young's modulus, POISSE: Ellenburger Poisson's ratio, POISSF: fault Poisson's ratio, Shmin: minimum effective horizontal stress gradient, Kv/Kh: vertical permeability over horizontal permeability anisotropy ratio.

Figure 2-9 shows the parameter ranges before and after history matching. The Ellenburger permeability (#2 PERME), fault cohesion (#3 COHEF), and fault Poisson's ratio (#8 POISSF) show significant reduction in range after history matching. We also observe a reduction in uncertainty range for several other poroelastic parameters. It is important to note that both fault cohesion (#3 COHEF) and minimum horizontal stress (#9 Shmin) move towards lower values, again suggesting that the fault is initially in a critically stressed state (Zoback et al., 2012; Hornbach et al., 2015; Lund Snee and Zoback, 2016; Quinones et al., 2018; Zhai and Shirzaei, 2018). A critically stressed fault can also explain why the matches in Figure 2-8b show lower simulated seismic moment magnitude

compared to the observed seismic event magnitude. If sufficient quantitative data were available to account for the initial plasticity of the fault elements, the matches to the observed seismic events most likely would have improved in Figure 2-8b.

Classification tree analysis is used to evaluate the relative parameter importance (Mishra and Datta-Gupta, 2017). The matched models are split into four groups or clusters based on the misfit function quartiles. Cluster 1 has the lowest misfit and cluster 4 has the highest misfit value. This means that solutions falling into cluster 1 most closely reproduce the observed history, whereas solutions falling into cluster 4 significantly deviate from history.

Figure 2-10 shows the binary classification tree for the seismic moment magnitude misfit and the injector BHP misfit. The binary classification tree is generated by recursively finding the variable splits that best separate the output into groups where a single category dominates (Breiman et al., 1984). The algorithm searches through the variables one by one to find the optimal split within each variable and the splits are compared among all variables to find the best split for that fork. The process is repeated until all groups contain a single category. Thus, the more dominant variables are generally the splits closer to the tree root. In this study, the minimum horizontal stress (Shmin) and fault Poisson's ratio (POISSF) dominate the seismic moment magnitude misfit. BHP misfit is most heavily impacted by the Ellenburger permeability (PERME).

It is important to note that if the effective minimum horizontal stress is higher than a threshold value (4.53 kPa/m), all simulation results will significantly deviate from the seismic event history because of insufficient accumulation of seismic moment magnitude.

The minimum horizontal stress gradient is readily obtained from minifrac tests and plays a critical role in evaluating the potential for induced seismicity.

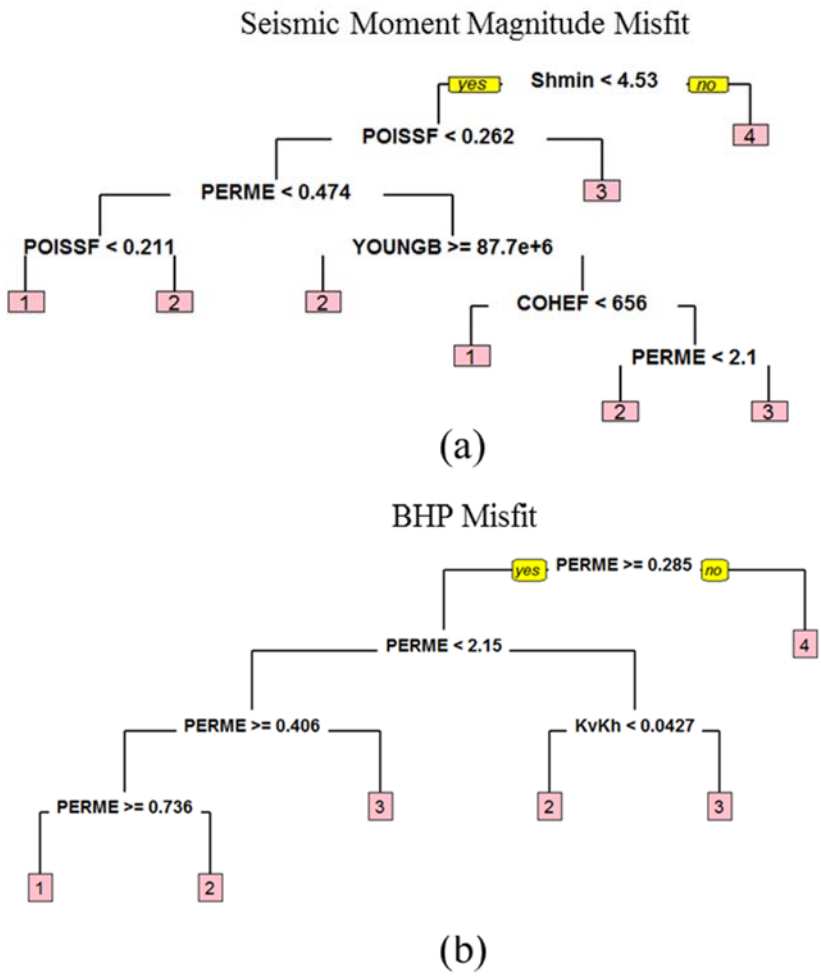

Figure 2-10. Parameter importance analysis using classification tree. (a) Seismic moment magnitude misfit and (b) injector pressure misfit. Shmin: minimum effective horizontal stress gradient, POISSF: fault Poisson's ratio, PERME: Ellenburger permeability, YOUNGB: basement Young's modulus, COHEF: fault cohesion, Kv/Kh: vertical permeability over horizontal permeability anisotropy ratio. Cluster 1 refers to the best model and cluster 4 refers to the worst model based on the data misfit. For example, the important parameter ranges for the best fit models can be understood by following the trail of cluster 1.

2.5. Results and Discussion

Wastewater disposal has been associated with induced seismicity and much of the literature has focused on reservoir pore pressure increase after injection as the primary mechanism for the seismicity (Zhang et al., 2013; Gono et al., 2015; Hornbach et al., 2015; Fan et al., 2016; Zhai and Shirzaei, 2018). However, our results indicate that pore pressure increase is not present in the Azle basement fault, and may not be the primary reason for the seismic events at Azle. Previous studies have suggested that the Barnett and Ellenburger formations are not isolated, and so will experience pressure communication between injection and production intervals (Pollastro et al., 2007b; Loucks et al., 2009; Hornbach et al., 2015). Our well head pressure calibration study reinforces this conclusion. However, when we account for both fluid injection and extraction, including the reservoir withdrawal from gas production, we see differential pressure increase and decrease within the Ellenburger on opposite sides of the Azle fault. However, we see no increase in pore pressure in the Azle fault within the basement.

To further examine the impact of gas production on the reservoir pressure, we performed coupled simulation including only water production. Figure 2-11 compares the injector BHP using the total fluid extraction rate (gas and water) as in this study versus water production rate only as in the previous study (Hornbach et al., 2015). Using only the water production rate, the simulated BHP deviates significantly from the observed pressure history.

The visualization of streamlines (fluid flow paths) from one of the calibrated models is shown in Figure 2-12a. Clearly, fluid flow occurs mostly in the Barnett and

Ellenburger formations and there is no fluid movement into the basement. Thus, there is no pore pressure change within the basement. However, even with the lack of fluid movement in the basement, Figure 2-12c and 2.13d show that there is noticeable plastic strain accumulation for the weaker elements along the fault. For this specific case shown in Figure 2-12, the fault Young's modulus and Poisson's ratio are 6.86e7 kPa and 0.16, respectively.

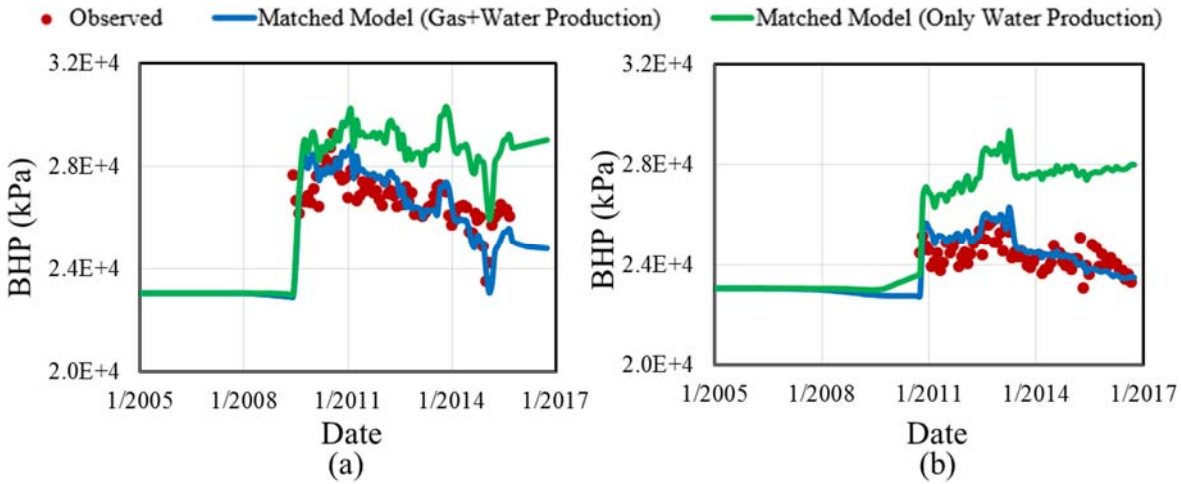

Figure 2-11. Comparison of injector BHP for the equivalent bottom hole total fluid rate (gas+water) vs water rate only for (a) Injector 1 and (b) Injector 2.

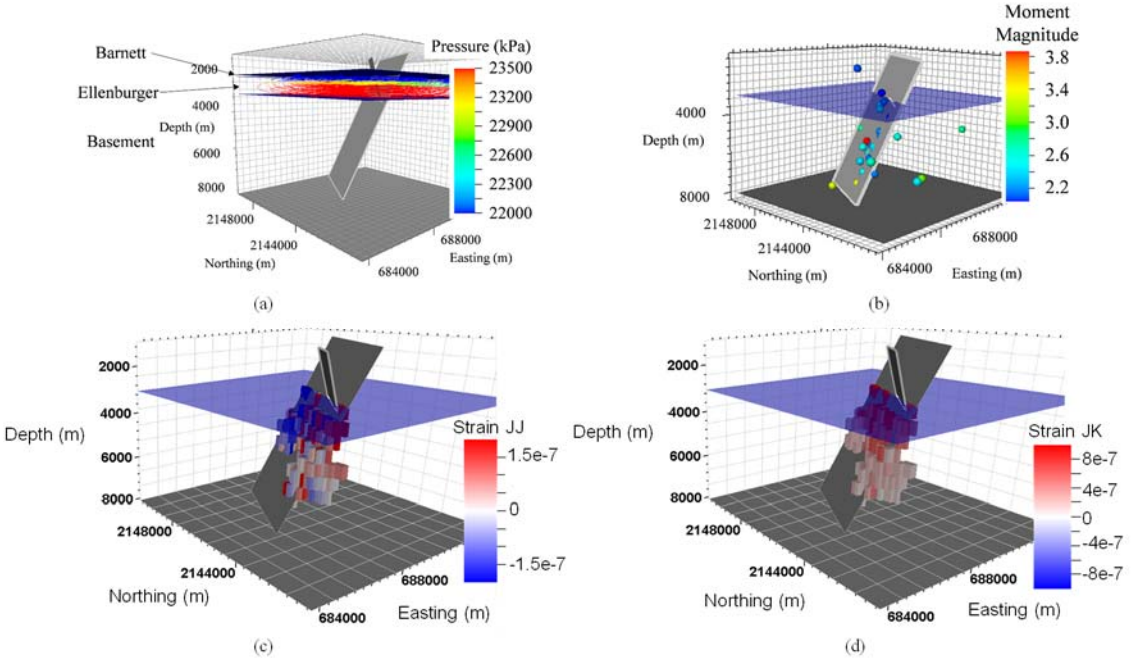

Figure 2-12. (a) Streamline flow visualization showing no fluid flow within the crystalline basement; (b) Seismic event locations; (c) The matched case plastic strain change JJ component and (d) The matched case plastic strain change JK component on January 1, 2014. The blue surface shows the top of the crystalline basement and the grey surface shows the primary Azle fault.

Plastic strain change accumulation is caused by the unbalanced loading on different sides of the fault as shown in Figure 2-13. On the northwest side of the main fault, there are two injectors and 20 producers active at various times during the simulation study. The overall net reservoir volume (cumulative injection volume minus cumulative production volume) at the end of the simulation history is approximately 3.5×10^6 m^3. On the other side of the fault, there are 50 active producers at various times during the simulation study, but no injectors. The overall net reservoir volume is approximately -8.1×10^6 m^3. Even though the reservoir is not completely compartmentalized by the fault

(Hornbach et al., 2015), the difference of net reservoir volume change on different sides of the fault creates an unbalanced loading on the basement. The unbalanced loading is evident from the pressure contours displayed on the streamlines in Figure 2-13c. As suggested in previous studies (McGarr et al., 2002; Ellsworth, 2013; National Research Council, 2013), change in loading conditions on faults due to fluid extraction and/or injection and associated stress changes can result in earthquakes, even with no direct hydrologic connection. This unbalanced loading can accumulate sufficient plastic strain on the weaker elements of the basement, resulting in stress fields capable of causing the observed earthquakes in the area. The mechanism of unbalanced loading is sensitive to the local imbalance of pressure within the Ellenburger across the Azle fault. The pressure imbalance is controlled by the local injection and production.

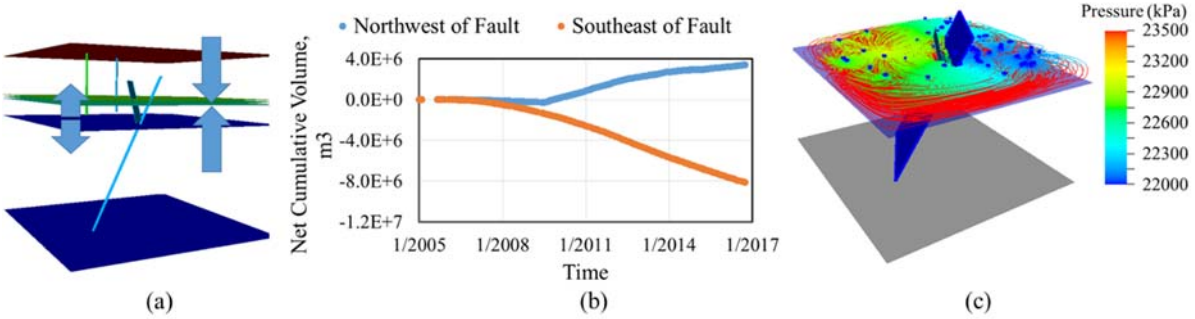

Figure 2-13. A schematic diagram for the unbalanced loading on different sides of the Azle fault; (b) The difference of net cumulative volume (injection volume – production volume) at different sides of the fault; (c) Streamline flow visualization showing pressure imbalance at different sides of the fault.

To further validate our observations, we perform a quantitative analysis to examine the relative contributions of pore pressure change and poroelastic stress change on the Coulomb failure stress change, $\Delta\tau$ (Chang and Segall, 2016a)

$$\Delta\tau = \Delta\tau_s + \mu\left(\Delta \mathrm{p} + \Delta\sigma\right) = \mu\Delta \mathrm{p} + \left(\Delta\tau_s + \mu\Delta\sigma\right), \tag{2.8}$$

where $\Delta\tau_s$ is the change in the shear stress, $\Delta\sigma$ is the change in normal stress calculated on the fault, $\Delta \mathrm{p}$ is the change in pore pressure and μ is the friction coefficient.

Figure 2-14 shows the change in pore pressure versus the change in poroelastic stress towards the top of the crystalline basement (3.3 km depth). The poroelastic stress changes clearly dominate in the basement with no noticeable change in pore pressure. Even though the low-permeability faults in the basement are not in pressure communication with the Ellenburger formation, the poroelastic stresses transmitted to the basement can trigger seismicity without elevated pore pressure in the basement fault.

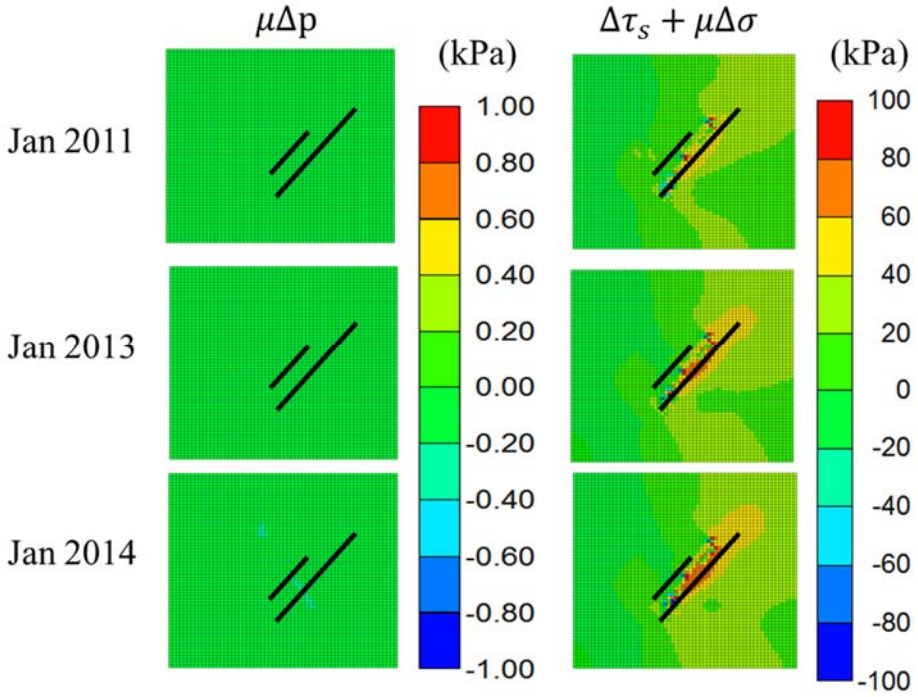

Figure 2-14. Pore pressure change and poroelastic stress change over time at the top of the crystalline basement (at 3.3 km depth). Please note the difference in scales in figure.

2.6. Conclusions

Geomechanical poroelastic interactions have significant impact on the seismicity observed in the Azle area, North Texas. Unbalanced loading on different sides of the main Azle fault appear to generate an accumulation of plastic strain change in the basement, most likely leading to stresses capable of causing the observed earthquakes in the area. Unlike previous studies, our results indicate that the pore pressure does not increase within the basement fault, and that pore pressure increase may not be sufficient to explain the seismicity near the Azle area.

An integrated evaluation of the gas and water production due to hydrocarbon recovery shows that the cumulative gas production is almost an order of magnitude larger than the water production, when corrected to reservoir volumes. The equivalent bottom hole fluid rate (combining reservoir withdrawal from both water and gas) used in this study suggests a reduction in Ellenburger pore pressure that is consistent with the observed well head pressure trends. We do not see fluid movement or a pressure increase in the crystalline basement, although there is plastic strain accumulation for the weaker elements along the fault in the basement. The accumulation of strain change is caused by the unbalanced loading on different sides of the fault. To the northwest of the main fault, there are two injectors and 20 producers, leading to an overall increase of net reservoir volume of approximately 3.5×10^6 m^3. To the southeast of the fault, there are 50 producers and an overall net decrease of approximately 8.1×10^6 m^3. Although the reservoir is not completely compartmentalized by the fault, this difference of net reservoir volume change on different sides of the fault creates an unbalanced loading to the basement.

A quantitative analysis shows that the poroelastic stress changes dominate in the basement with no noticeable change in pore pressure. Even though the low-permeability faults in the basement are not in pressure communication with the Ellenburger formation, the poroelastic stresses transmitted to the basement can trigger seismicity without elevated pore pressure.

3. DETAILED FAULT MODELING AND IMPLICATIONS ON SEISMICITY

3.1. Overview

To model the mechanisms, location and magnitude of seismic fault slips in response to fluid production and injection in the Azle area, we built a workflow to couple 3-D finite difference and finite element simulations to evaluate the fault slips of the critically stressed faults. The finite difference simulation is calibrated with the historical rate and pressure data of the nearby wells and the calibrated results are used to update the pressure field for the finite element simulation. The finite element simulation calculates the stress field and the fault displacement based on the imported pressure field from the finite difference simulation. One distinguishing feature of this study is the detailed fault modeling. The faults geometry is constrained by the regional high resolution seismic picks provided by the operator and the faults are modeled as discontinuous surfaces. Thus, the fault slips can be explicitly computed. Furthermore, we can evaluate the magnitude and location of the fault displacement and assess the fault dissipated energy. The simulation results suggest that the fault displacement can occur in the basement formation where there is no direct pressure communication with injection or production wells. The indirect poroelastic stress transfer seems to be the dominant cause for the fault activation in the basement. Performing pore pressure simulation by itself may not be sufficient to infer the fault slips and evaluate induced seismicity risks. The radiated energy from the observed seismic events is only 20% of the dissipated energy from the simulation, showing that not all energy is released seismically. This coupled workflow allows us to perform a

systematic parameter sensitivity analysis on the location, timing, and magnitude of the fault slips and the evolvement of the dissipated energy for future use.

3.2. Introduction

Earthquakes in unusual locations have received considerable attention in the US due to the concern that human activities could cause damaging earthquakes. It has been understood that earthquakes can be induced by human activities which alter the pore pressure and stress/strain response in the subsurface. These activities include but not limited to impoundment of reservoirs, mining, hydrocarbon extraction, and injection of fluids into underground formations. In particular, the potential association between waste water disposal wells and earthquakes has become an important topic of discussion due to the relation of this activity with the development of tight shale reservoir by hydraulic fracturing.

Induced and triggered earthquakes are controlled by how fluid pressure alters the in situ stress on faults in the subsurface. These stresses can be resolved using two different approaches: (1) a fluid-solid decoupled process where the normal stress on the fault is impacted by the changes in the fault zone pore pressure (e.g., Terzaghi effective stress law) or (2) a fluid-solid coupled process (e.g., Biot's theory of linear poroelasticity). Pore pressure modeling studies show that the presence of critically stressed faults within the target injection formation or the basement is likely to be activated by injection related pore pressure increase (Zhang et al., 2013; Keranen et al., 2014; Gono et al., 2015; Hornbach et al., 2015). Many of the models neglect poroelastic stress changes associated with

injection and/or production, assuming that direct pore pressure changes are the determining factor for fault activation. However, indirect poroelastic stress/strain change may perturb faults without direct pore pressure change in the faults. Fluid injection or extraction can induce seismicity by altering the stress/strain field of adjacent formations due to poroelastic coupling (Segall, 1989; Segall and Lu, 2015; Chen et al., 2018; Chen et al., 2020). Specifically, Chen et al. (2020) suggests that the unbalanced loading due to the differential in fluid extraction and injection on different sides of the critically stressed fault appears to be the cause of observed seismicity in the Azle area. They models the faults as a set of fault cells with distinct flow and geomechanical properties and the seismic moment is calculated based on the deformation of the fault cells. One potential improvement is to include a more detailed fault modeling to incorporate the natural behavior of fault slips. In this study, we generate the fault model using the seismic picks provided by the operator. After that, we use the fault model to build the finite difference and finite element simulation models. The faults are described as discontinuous surfaces in the finite element simulation. We develop the workflow to couple the two simulation models. The calibrated pressure field from the finite difference model is imported to the finite element model to explicitly simulate the fault displacement and the corresponding energy released.

3.3. Methodology

We develop a coupled fluid flow and geomechanical simulation workflow to model the pressure and stress/strain field near the critically stressed fault in the Azle area. The coupling workflow is under quasi-static assumption. Thus, inertial effects will not be

considered and dynamic fault modeling is out of the scope of this study. In this workflow, fluid flow and geomechanical equations are solved numerically using the finite difference (FD) and the finite element (FE) schemes, respectively and they interact with each other through a sequential coupling. Pore pressure obtained by the FD model (CMG) will be passed into the FE model (ABAQUS®). The FE model will provide detailed geomechanical output including 3D stress/strain field as well as the fault slips. After establishing the workflow, we can analyze the Azle fault slip behavior and the corresponding energy released and compare it with the observed seismicity events.

Faults are modeled as discontinuous surfaces with interface elements. One of the advantages of describing faults as discontinuous surfaces is that displacement along the fault surfaces can be explicitly computed. Then, the seismic moment, M_0, can be calculated as:

$$M_0 = G\bar{u}S, \tag{3.1}$$

where G is shear modulus, $\bar{u}$ is average slip distance and S is the rupture area.

3.4. Detailed Fault and Geologic Modeling

To evaluate the fault slip behavior and its corresponding seismicity risks, the detailed fault simulation model is required. In this study, high resolution seismic fault picks are provided by the operator to build the detailed fault model. The raw seismic fault picks are shown in Figure 3-1. The seismic fault picks agree well with the seismic hypocenter locations interpreted by the Southern Methodist University seismic catalogs (Hornbach et al., 2015; DeShon et al., 2018).

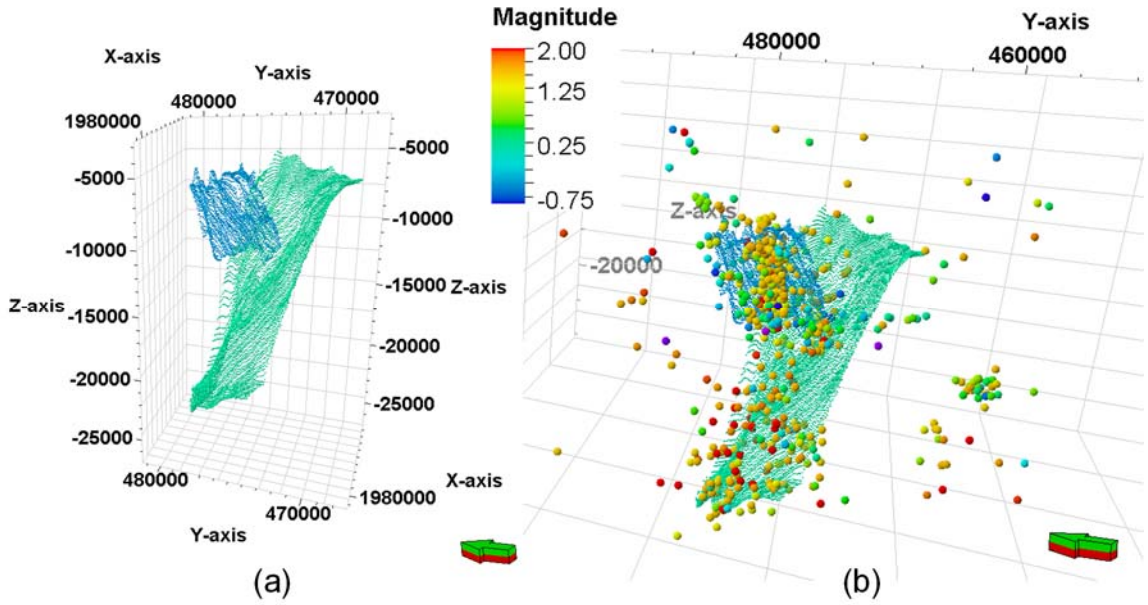

Figure 3-1. (a) Raw seismic fault picks provided by the operator (blue for antithetic fault and green for main fault) and (b) raw seismic fault picks overlap with seismic event hypocenter locations. Blue dots are the antithetic fault and green dots are the main fault. Colored dots are the seismic hypocenters.

To build simulation fault models, we first convert the seismic fault picks to the fault surfaces in Petrel. The initial fault surfaces can be very unsmooth with large curvature changes as they try to honor every single point from the seismic picks shown in Figure 3-2a. This unsmooth surface can cause serious meshing and convergence issues, especially when the faults are modeled as discontinuous surfaces in the FE simulation. Thus, we perform a series of surface smoothing and trimming to generate the smooth fault surfaces in Figure 3-2b. This smooth fault surfaces are used as the base geometry for the FD and the FE simulation faults.

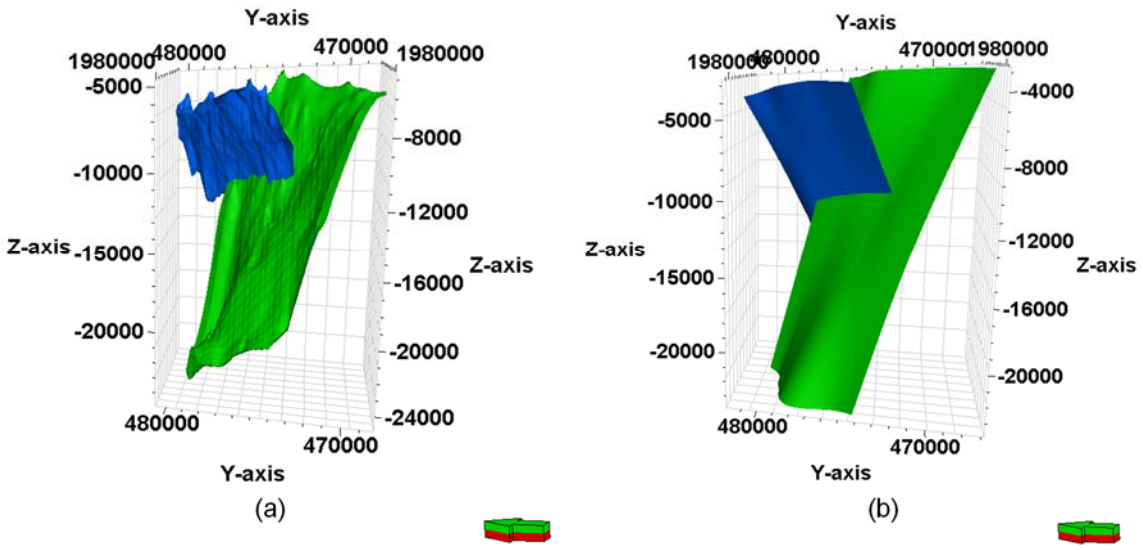

Figure 3-2. (a) Raw seismic fault picks provided by the operator and (b) raw seismic fault picks overlap with seismic event hypocenter locations. Blue surface is the antithetic fault and green surface is the main fault.

For the FD (CMG) model, we use the structural grid with zig-zag fault. For the ABAQUS model, we build the fault based on the real fault geometry. Thus, fault surface curvature change (strike and dip change) can be captured and modeled in the FE simulation. The difference in fault strike and dip represent the difference of initial stress state at different location of the fault surfaces. The fault strike and dip histograms are shown in Figure 3-3. The initial stress state and the slip tendency for the main fault are shown in Figure 3-4. The slip tendency is defined as the effective shear stress divided by the effective normal stress. Note that there is no cohesion for this FE simulation approach. In this study, the fault friction coefficient is 0.7 (Hennings et al., 2019). Thus, the fault region with the slip tendency closer to 0.7 is in a more critically stressed state than the region with the smaller slip tendency.

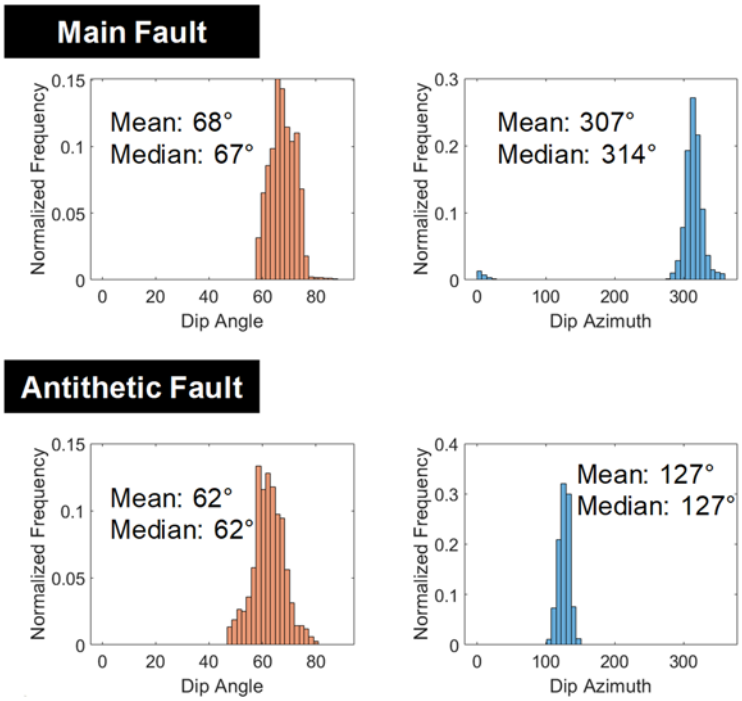

Figure 3-3. The strike (dip azimuth) and dip histogram for the main fault and the antithetic fault.

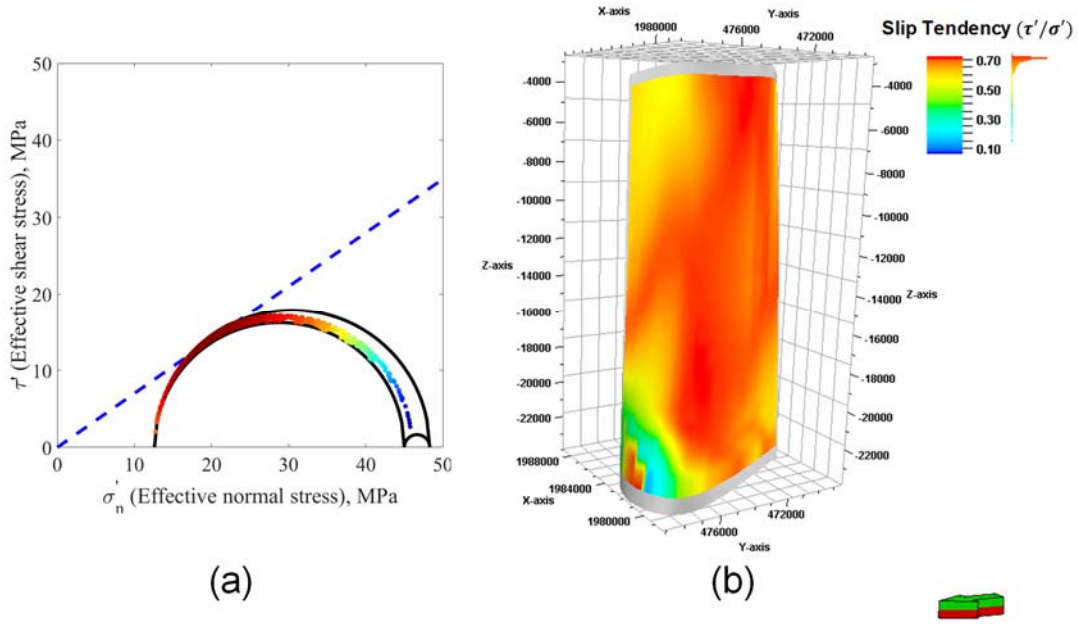

Figure 3-4. (a) The initial stress state and the slip tendency for the main fault.

Figure 3-5 shows the main simulation fault in each simulation model. Note that we cannot directly generate mesh in ABAQUS using Petrel exported fault surfaces. An intermediate step from Petrel to SolidWorks is required to generate the mesh and the simulation fault model in ABAQUS.

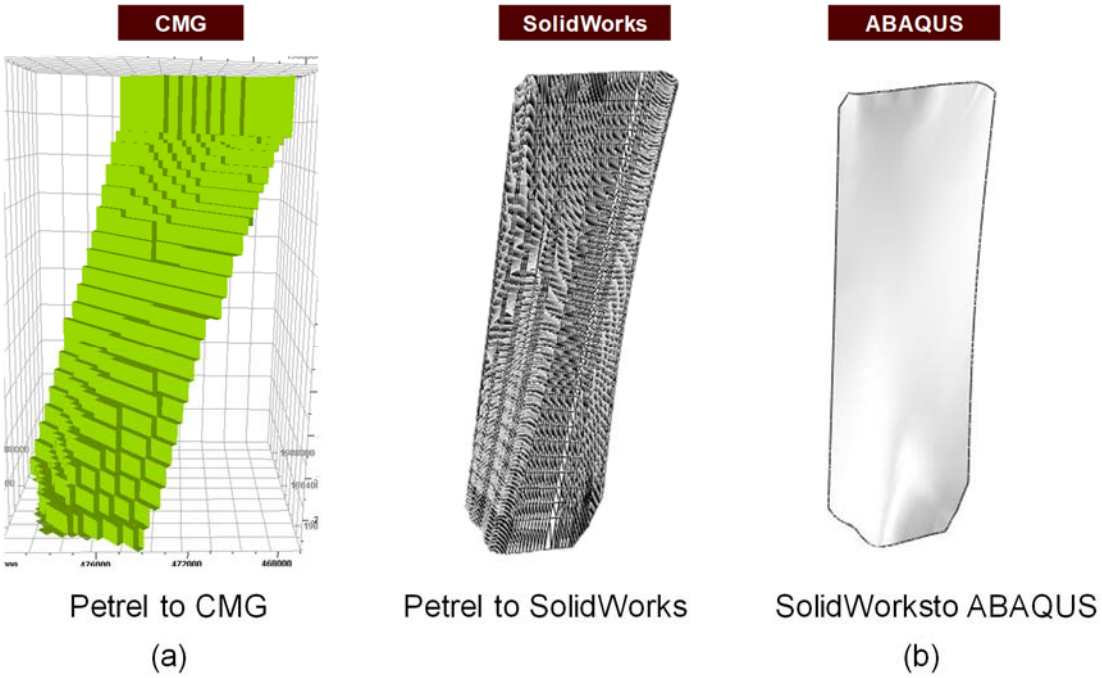

Figure 3-5. Simulation fault models in (a) the FD (CMG) simulation and in (b) the FE (ABAQUS) simulation.

The seismic horizon picks are also provided by the operator as shown in Figure 3-6a. The seismic horizon picks do not cover the entire simulation area and therefore extrapolation is required to get the horizons for the entire simulation region. The maximum depth difference of the seismic horizon picks is around 100 meter. Thus, flat horizons using the average depth of the seismic horizon picks are used to build both CMG and ABAQUS models. Using flat horizons can significantly simplify and accelerate the mesh generation step in ABAQUS without sacrificing much accuracy. The geologic model is

shown in Figure 3-6b. The top of Marble Falls is at 1702m depth, the top of Barnett is at 1801m depth, the top of Ellenburger is at 1890m depth, and the top of basement is at 3007m depth. The bottom of the basement is at 8500m depth. This depth is almost 1000m deeper than the deepest recorded seismic event to avoid any boundary effect.

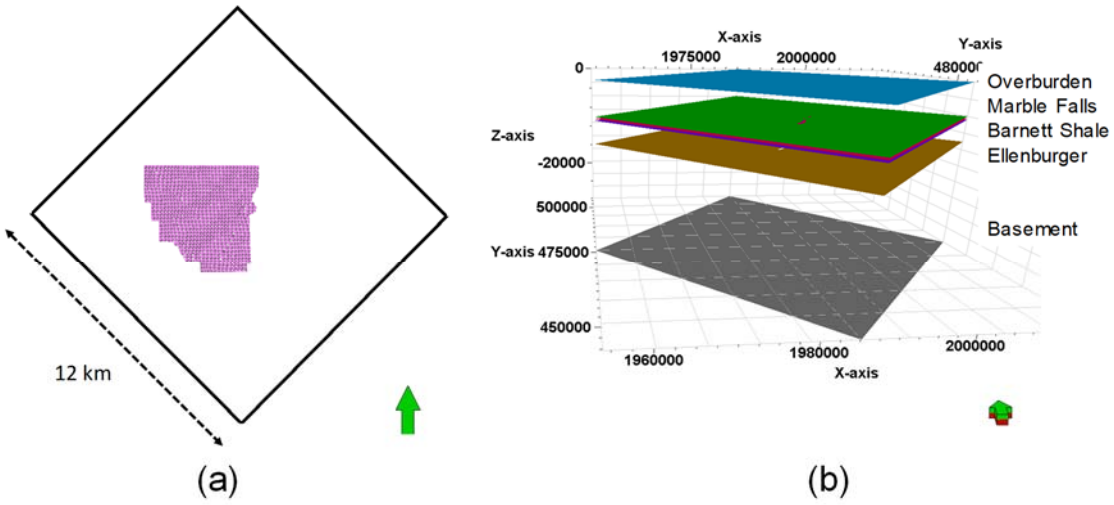

Figure 3-6. (a) Top view of the seismic Ellenburger horizon picks (pick) and the simulation model boundary and (b) geologic model using flat horizons.

3.5. CMG Simulation Model and Calibration

The CMG model includes 70 producers and 2 injectors. The top view of the well and fault locations are shown in Figure 3-7. 28 out of the 70 producers are operated by XTO, where high resolution rate (gas and water) and well head pressure (THP) data are available for this study. The gas and water rate data for the rest of the producers are available in the Drillinginfo database (Drillinginfo, 2018). Injection rate and well head pressure data are both available through Railroad Commission of Texas (2018a). The field production history is shown in Figure 3-8.

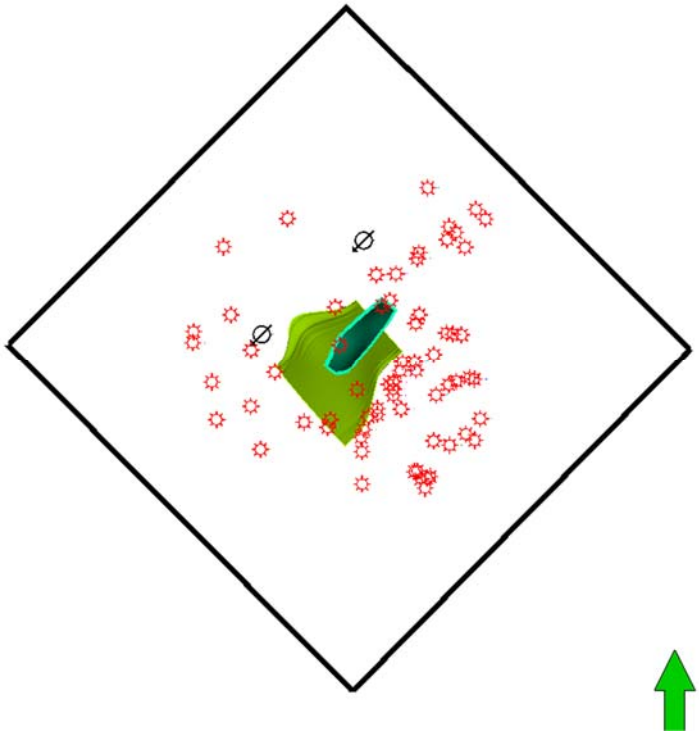

Figure 3-7. Top view of the well and fault locations.

Figure 3-8. Field production and injection history.

For the CMG simulation, all the wells are under the bottom-hole fluid rate constraints. The history matching misfit objective function is the sum of 3 individual objective functions: the injector BHP, XTO producers' THP, and the cumulative gas production for each producer. The misfit function is given by:

$$obj = \omega_{BHP} obj_{BHP} + \omega_{THP} obj_{THP} + \omega_{CumGas} obj_{CumGas}, \tag{3.2}$$

where ω is the weight for each objective function.

Since the injectors here inject only water, the injector BHP can be easily computed from THP. The injector BHP misfit is given by:

$$obj_{BHP} = \log\left(\sum_{j=1}^{Nwell} \sqrt{\sum_{i=1}^{Ntime} (BHP_{i,j}^{obs} - BHP_{i,j}^{cal})^2}\right), \tag{3.3}$$

where Nwell is the total number of injection wells, Ntime is the total number of data points for each well, superscript obs indicates observed data, and superscript cal indicates calculated value from the simulation.

Because multi-phase (gas and water) flow occurs in the pipe. We use the commercial software Prosper® to build the wellbore model and import the wellbore model to CMG. Thus, the simulated THP is calculated during the simulation run. The XTO producer THP misfit is given by:

$$obj_{THP} = \log\left(\sum_{j=1}^{Nwell} \sqrt{\sum_{i=1}^{Ntime} (THP_{i,j}^{obs} - THP_{i,j}^{cal})^2}\right), \tag{3.4}$$

where Nwell is the total number of XTO production wells, Ntime is the total number of data points for each well.

The producer cumulative gas production misfit is given by:

$$obj_{CumGas} = \log(\sum_{j=1}^{Nwell} \sqrt{\sum_{i=1}^{Ntime} (CumGas_{i,j}^{obs} - CumGas_{i,j}^{cal})^2}), \quad (3.5)$$

where Nwell is the total number of production wells, Ntime is the total number of data points for each well. Note that we take log-transformation of all objective functions to prevent the overall objective function being dominated by any particular objective function with significantly higher misfit values.

Before performing the history matching, we first run sensitivity analysis to identify the "heavy hitters" for the history matching objective function. The sensitivity tornado plot is shown in Figure 3-9. Fracture permeability has the largest impact on the history matching function because it influence the producer BHP and therefore producer THP. KvKh influences the amount of water production from the underlying Ellenburger formation. Barnett initial water saturation influences the production gas water ratio. Ellenburger permeability impacts the injector BHP. These parameters will be tuned during the history matching process to reduce the model misfit.

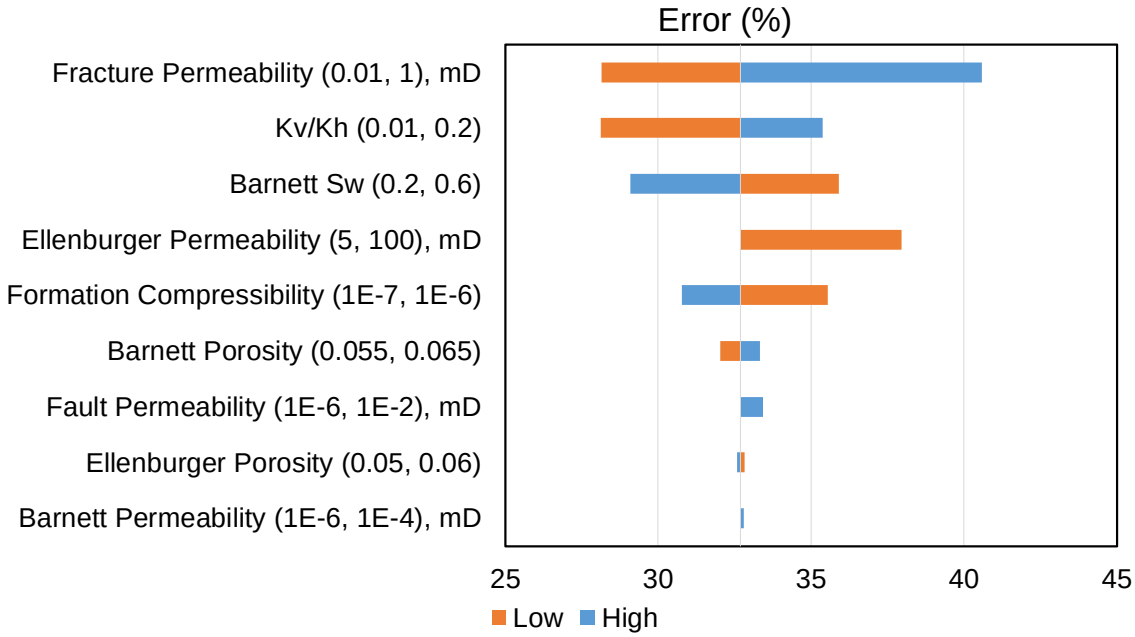

Figure 3-9. Sensitivity of history match misfit objective function to various reservoir parameters.

After identifying the parameters with high influence on the objective function, we perform history matching using CMG CMOST. CMG Designed Exploration and Controlled Evolution (DECE) optimizer is used to reduce history match objective function. It is an iterative optimization algorithm that include a designed exploration stage and then a controlled evolution stage. In the exploration stage, it explores the entire search space in a designed random manner. In the evolution stage, it improves solution quality using statistical analyses to reduce the possibility of poor solutions being picked again. Meanwhile, it checks rejected candidates from time to time to avoid the possibility of being trapped in local minimum.

The history result is shown in Figure 3-10. The base case history matching error is about 33%. The history matching error quickly decreases over the first 150 simulations

and stabilizes at around 23% for the rest of the simulation runs. We then check individual well response to make sure the simulated results match well with the observed data. Figure 3-11 shows the simulated and observed BHP responses for two of the injectors. The optimal solution matches well with the historical data. It shows a higher simulated BHP than that of the base case. Figure 3-12 shows the simulated and observed cumulative gas production for four of the production wells. Again, the optimal solution matches well with the observed data, showing a lower simulated cumulative gas production than the base case estimate. Figure 3-13 shows the simulated and observed THP for two of the XTO wells. The THP misfit is reduced for the optimal model compared to the base case. However, we do not achieve the same quality of the match as the injector BHP and the cumulative gas production. One reason is the error introduced by the wellbore model. The multi-phase gas-water pipe flow is a highly complex process. Model calibration may be required at the wellbore level but it is not in the scope of this study. Thus, a lower weight is assigned to the THP misfit so it has less impact on the history match objective function. Overall, the optimal solution achieves reasonable matches with the observed data.

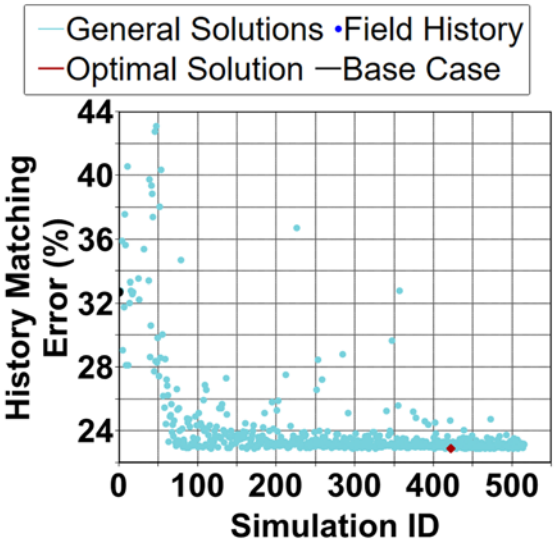

Figure 3-10. History matching error over simulation evolution.

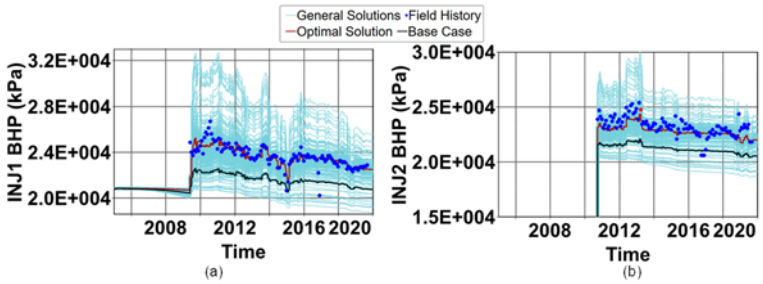

Figure 3-11. Simulated vs. observed BHP for (a) injector 1 and (b) injector 2.

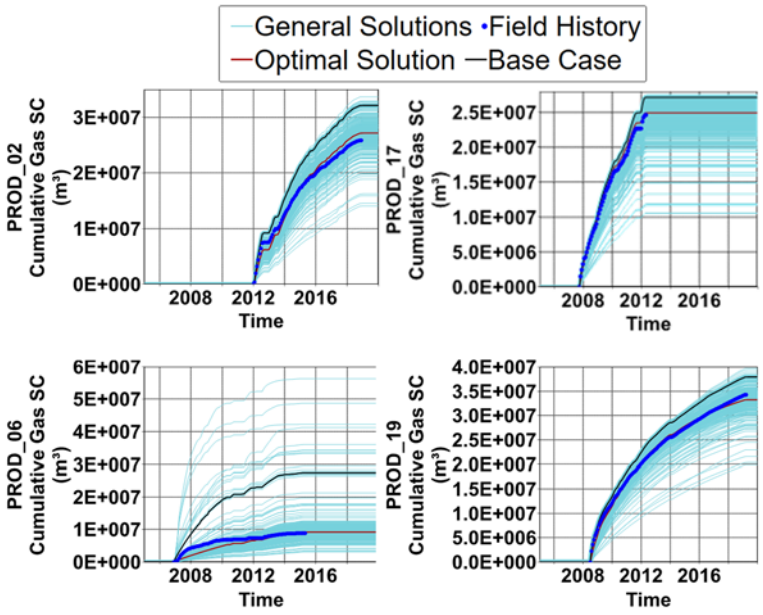

Figure 3-12. Simulated vs. observed cumulative gas production for example production wells.

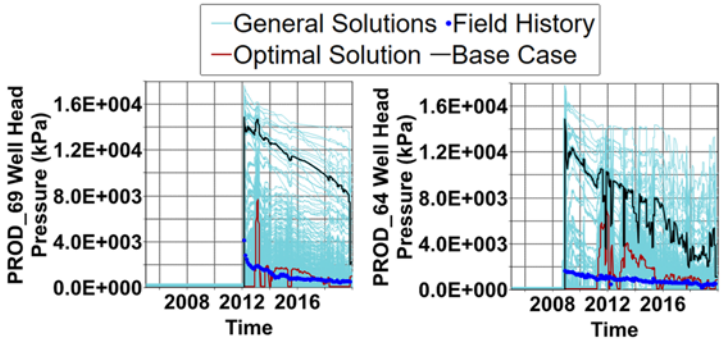

Figure 3-13. Simulated vs. observed THP for example XTO producers.

We further analyze the parameter uncertainty range before and after the history matching using histogram in Figure 3-14. All the parameter uncertainty ranges are reduced after the history matching. Barnett initial water saturation is calibrated to higher values to allow more water entering the wellbore to match the cumulative gas production and XTO well THP. Ellenburger permeability is calibrated to lower values to increase the injector

BHP to match the observed BHP. KvKh is calibrated to higher values to allow more vertical pressure communication.

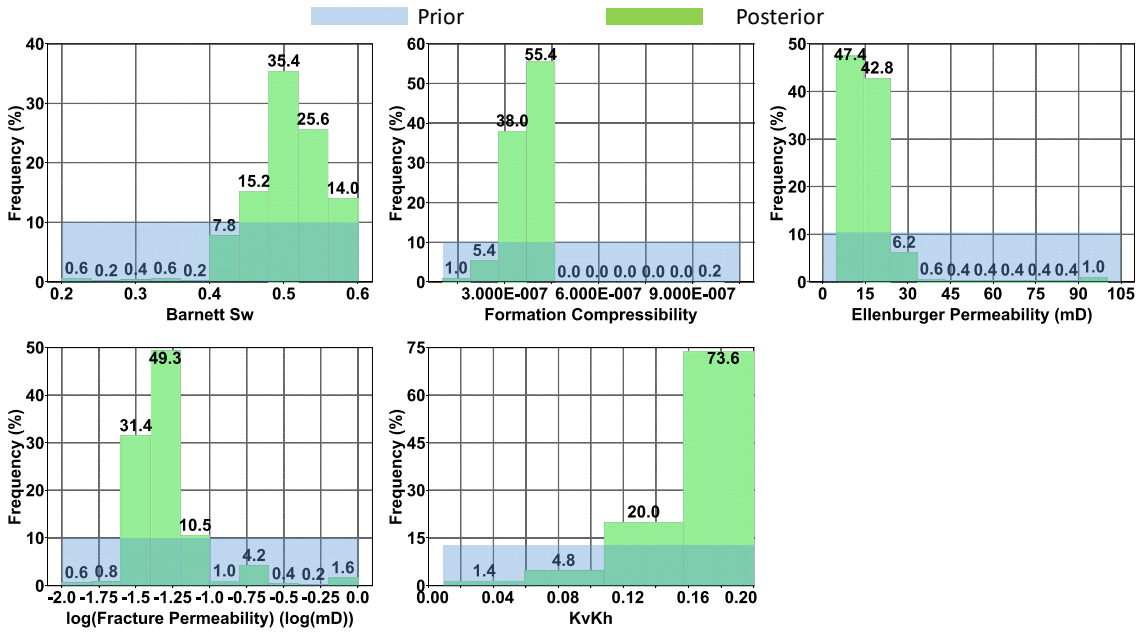

Figure 3-14. Simulated vs. observed THP for example XTO producers.

After history matching, we look at the pressure distribution (Figure 3-15) at the middle of the Ellenburger (2500 m). This is the formation that experiences the most pressure change. In 2010, within a year after injection started, we observe pressure difference between the two sides of the fault. In 2014, we see the maximum pressure imbalance about 1,000 kPa on different sides of the fault. This is the time when most of the Azle seismic events were recorded. From 2014 to 2018, the pressure imbalance stays at about the same level and no more seismic event was recorded in this region. These pressure distribution results are used as input for the ABAQUS simulation to model the fault slips and the corresponding energy released.

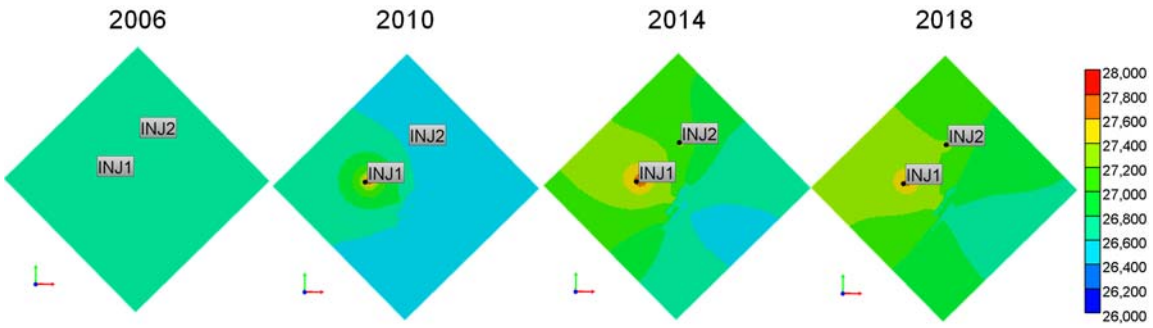

Figure 3-15. Calibrated model pressure distribution over time at the middle of the Ellenburger formation (2500 m).

3.6. ABAQUS Model and Geomechanical Response

Unlike the zig-zag Azle faults used in the CMG model, the ABAQUS simulation models the Azle faults as discontinuous surfaces (Figure 3-16). We first build the model skeleton using the horizon tops and the fault planes (Figure 3-16a). We then create the mesh (Figure 3-16b). This model consists of 104,848 nodes and 98,010 cells. Figure 3-16c is the Northwest side of the model cut by the antithetic fault plane. Figure 3-16d is the Southeast side of the model cut by the main fault plane. The total vertical stress gradient is 26.01 MPa/km, the total maximum horizontal stress is 26.01 MPa/km, the total minimum horizontal stress is 14.20 MPa/km, and the pore pressure gradient is 10.65 MPa/km (Hennings et al., 2019).

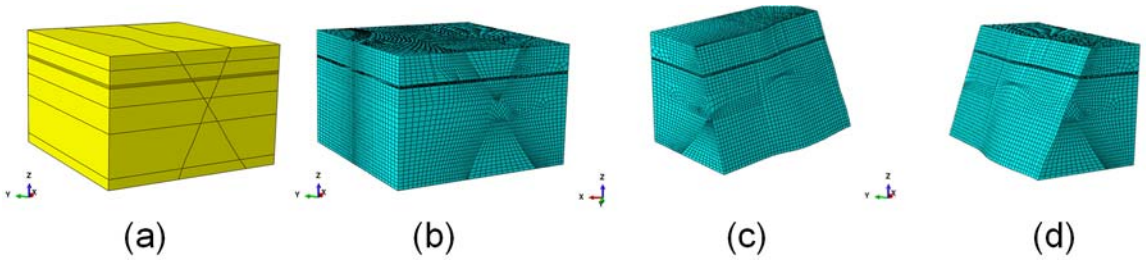

Figure 3-16. (a) Skeleton of the ABAQUS model. (b) ABAQUS model meshing. (c) Northwest side of the model cut by the antithetic fault plane. (d) Southeast side of the model cut by the main Azle fault plane.

After calibrating the model using rate and pressure data, the matched model pressure is processed and imported to the FE ABAQUS model. We then calculate the stress distribution and the fault slips based on the pressure input. Figure 3-17 shows the plastic fault slips at different times. In 2006, when there is no injection, most of the plastic slips occur in the Ellenburger and the magnitude is relatively small. In 2010, within a year after injection, the modeled slips propagate downward to the basement. After that, the modeled slips then continue to propagate downward. In 2014, when most of the earthquakes were observed, we see the deepest plastic slips in the model is at roughly 7000m.

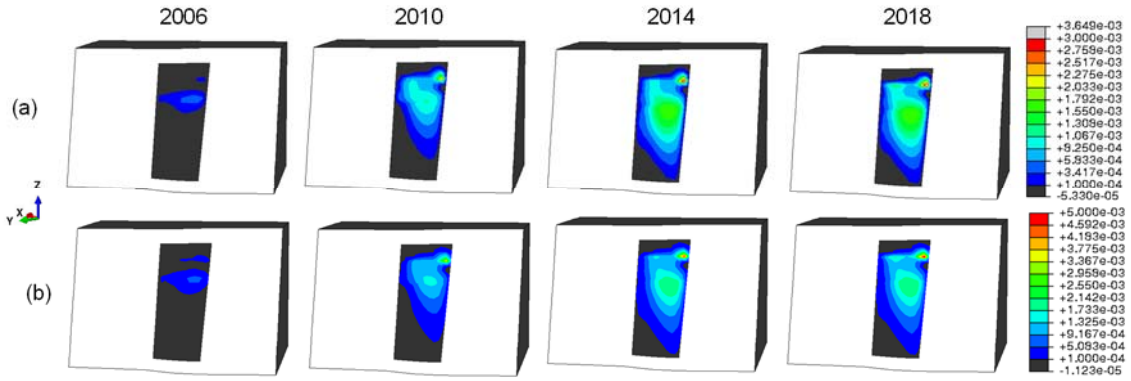

Figure 3-17. Calibrated model plastic slips of the main fault over time: (a) in the vertical direction and (b) in the horizontal direction.

We also examine the slip and pressure behavior versus depth along the middle of the fault. Figure 3-18a and Figure 3-18b show the pressure change and the slip behavior along the path shown in the red arrow in Figure 3-18c. We see no pressure change along the fault path in the basement formation throughout the simulation period. Figure 3-18b shows that most of the slips occur in the Ellenburger formation prior to 2010. In 2010, shortly after injection starts, the slips propagate downward to the basement formation. Slips continue to propagate downward and the slips reach the peak in 2014. This is the time when most of the seismic events were recorded. There is not much slip from 2014 to 2018. Since most of the slips in the basement occur without noticeable pressure change, the indirect poroelastic stress transfer is the driving mechanism for the recorded earthquake in the Azle area.

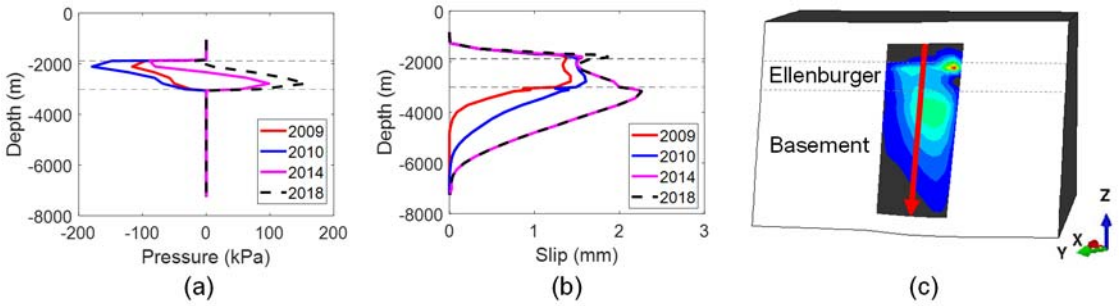

Figure 3-18. (a) Pressure change along the middle of the main fault. (b) Slip along the middle of the main fault. (c) The fault path for (a) and (b).

Besides the fault slips, we also calculate the dissipated energy from the plastic fault slips and compare it with the radiated energy from seismic events in the region. The radiated energy is calculated as:

$$M_w = \frac{2}{3}\log(E_s) - 3.2\,, \tag{3.6}$$

where E_s is the radiated energy and M_w is the seismic moment magnitude. The radiated energy from the observed Azle seismic event magnitude and the dissipated energy from the ABAQUS model is shown in Figure 3-19. The total radiated energy is roughly 20% of the calculated dissipated energy. This may occur because not all the dissipated energy is released seismically. The dissipated energy evolves more smoothly compared the abrupt release of the radiated energy in a short period of time. Matching the timing and the slope of the radiated energy release is not included in this study. Further analysis may be required to perform sensitivity analysis and history match the timing and slope of the dissipated energy.

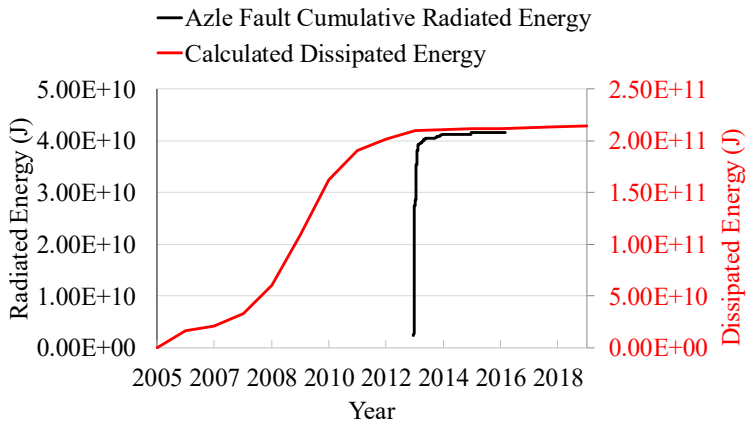

Figure 3-19. Cumulative radiated energy from the observed Azle seismic events and dissipated energy from ABAQUS simulation model.

3.7. Conclusions

We have successfully constructed the detailed geometric Azle fault models using XTO seismic fault picks in Petrel. The geometric fault models are converted to the simulation fault models used in both the finite difference CMG simulation and the finite element ABAQUS simulation.

We have built the simulation models in the finite difference fluid flow simulation in CMG and the finite element geomechanical simulation in ABAQUS using the corresponding detailed fault simulation models. We have developed the workflow to couple the flow and geomechanical simulation.

The CMG model has been calibrated using injector BHP, cumulative gas production, and XTO producer THP. The calibrated pressure is imported to the ABAQUS model to explicitly model the Azle fault slips and the dissipated energy associated with the slips.

The ABAQUS model shows that the Azle fault slips can occur at the location where there is no pressure change. The observed radiated energy from the Azle seismic events is about 20% of the dissipated energy calculated from the plastic slips. Further investigation is undergoing to reconcile the differences between the dissipated and radiated energy of the Azle site.

4. THE IMPACT OF CLUSTERING SPACING ON MULTI-FRACTURED WELL PERFORMANCE*

4.1. Overview

A major outstanding challenge in developing unconventional wells is determining the optimal cluster spacing. The spacing between perforation clusters influences hydraulic fracture geometry, drainage volume, production rates, and the estimated ultimate recovery (EUR) of a well. This paper systematically examines the impact of cluster spacing in the Eagle Ford shale wells by calibrating fracture geometry and fracture/reservoir properties using field injection and production data and evaluating the optimal cluster spacing under different reservoir conditions.

We explore a sequential technique to evaluate and optimize cluster spacing using a controlled field test at the Eagle Ford field. This study first identifies the fracture geometry by history matching the field injection treatment pressure. Using the rapid Fast Marching Method based flow simulation and Pareto-based multi-objective history matching, we match the well drainage volume and the cumulative production to calibrate the fracture and SRV properties. The impact of cluster spacing on the EUR are examined using the calibrated models. We run injection and production forecasts for various cluster spacing to investigate optimal completion under different reservoir conditions.

* Part of this section is reprinted with permission from "The Impact of Cluster Spacing on Multi-Fractured Well Performance" by Chen, R., X. Xue, A. Datta-Gupta, H. Yu, and N. Kalyanaraman,. (2019), paper SPE-197103-MS presented at the SPE Liquids-Rich Basins Conference - North America, 7-8 November, Odessa, Texas, USA. Copyright [2019] Society of Petroleum Engineers.

The unique set of injection and production data used for this study includes two horizontal wells completed side by side. The well with tighter cluster spacing has larger drainage volume and better production performance. This is because of the increased fracture complexity in spite of the impact of stress shadow effects leading to shorter fractures. The calibrated models suggest that most of the fractures are planar in the Eagle Ford shale. The well with wider cluster spacing tends to develop longer fractures but the well with tighter cluster spacing has better stimulated reservoir volume with enhanced permeability, thus resulting in better drainage volume and production performance. From the optimization runs under different reservoir conditions, our results seem to indicate that when natural fractures are present or when stress anisotropy is high with no natural fractures, the wells with tighter cluster spacing tend to outperform the wells with wider cluster spacing. However, severe stress shadow effect is observed when stress anisotropy is low with no natural fractures, likely making tighter cluster spacing wells less favorable.

The calibrated fracture geometries and properties with a unique set of Eagle Ford field data explain the performance variation for completions using different cluster spacing within the reservoir and provides insight into optimal cluster spacing under different reservoir conditions (low vs high stress anisotropy and with/without natural fractures).

4.2. Introduction

Multi-stage hydraulic fracturing is an integral part of unconventional shale reservoir development. A major outstanding challenge in designing a multi-stage hydraulic fracturing job is to determine the optimal cluster spacing. The current trend of

optimal fracturing design has been reducing cluster spacing while increasing fluid and proppant usage (Evans et al., 2018; Pioneer Natural Resources Company, 2018). Many simulation works also suggest an improved well performance using a tighter cluster spacing design (Cipolla et al., 2009; Lolon et al., 2009; Zhu et al., 2017). However, researchers also found that if the cluster spacing is below some threshold values, the well productivity may decrease (Miller et al., 2011). Therefore, it is crucial to understand the characteristics of fracture networks under different cluster spacing designs and their impacts on production performance.

There have been many efforts to characterize fracture networks and understand the impact of cluster spacing. Weng et al. (2011) developed Unconventional Fracture Model (UFM) that can simulate complex hydraulic fracture network propagation in formation with pre-existing closed natural fractures, and explicitly model hydraulic injection into a fracture network with multiple propagation branches. Park and Kim (2016) employed a semi-analytical approach to solve flow equation numerically and geomechanics analytically to model hydraulic fracture propagation. Zhu et al. (2018) and Zhang and Zhu (2019a) interpreted the distributed temperature data of horizontal wells to characterize the complex fracture networks and understand the impact of cluster spacing on the fracture geometry. Zhou et al. (2016) investigated the optimal cluster spacing under the impact of the induced stress from other hydraulic fractures. Roussel et al. (2012) developed a mechanical stress perturbation model to identify the optimum spacing for fractures to remain transverse under stress shadow effects. Simpson et al. (2016) integrated field treatment pressure data from hydraulic fracturing and well production data to investigate

stress shadow effects and generate fracture geometry. Wu et al. (2017) developed fracture propagation model to study the uneven fracture growth introduced by fracture stress shadowing. These studies focus on modeling the poroelastic stress field altered by the hydraulic fracture treatment and the hydraulic fracture geometry resulting from the altered stress field. However, its impact on well production performance is not well understood. There have been previous efforts to integrate production forecast with fracture propagation to build a more comprehensive workflow. Park et al. (2019) altered the rock dilation and compaction table to characterize the reservoir and the hydraulic fractures using both the injection and the production data. However, all the fractures are assumed to be planar. Suarez and Pichon (2016) modeled explicitly the hydraulic fracture geometry and coupling it directly to a production simulator to optimize well completion design. Xiong et al. (2018) used an integrated completion and production simulation workflow to history match the existing well with wider cluster spacing and to forecast well performance with reduced cluster spacing completion. These studies provide valuable insights about how fracture geometry and properties can affect well production. However, it may be an untenable assumption that the calibrated parameters from production history matching in one fracture geometry can be directly applied to another fracture geometry. Thus, the impact of tighter cluster spacing may not be well analyzed.

In this study, we explore the impact of cluster spacing on multi-fractured horizontal well performance using a unique set of Eagle Ford well data. The data set consists of two horizontal wells that were completed side by side at the same depth. Thus, the impact of geologic variation is minimized. The well spacing is 1200 ft, so there is

minimum impact of well interference on fracture propagation and production performance. Therefore, we can focus on studying the impact of different cluster spacing designs. One well was completed using a wider cluster spacing of 50 ft with less fluid and proppant while the other well was completed using a tighter cluster spacing of 20 ft with more fluid and proppant. Both injection and production data are provided by the operator and the objective is to understand the impact of tighter cluster spacing on fracture geometry and production performance. To achieve the goal, we first conduct history matching of the field injection treatment pressure to characterize fracture geometry using a commercial model, Mangrove®. Second, we history match well production response to characterize fracture and stimulated reservoir volume (SRV) properties. Finally, we analyze the features in the calibrated fracture geometry and properties of the two wells to examine the impact of cluster spacing on fracture propagation and production. The calibrated models suggest that the well with tighter cluster spacing tends outperform the well with wider cluster spacing because of increased fracture complexity leading to better stimulated reservoir volume quality, despite having shorter and less permeable fractures.

4.3. Geologic and Well Data

The Eagle Ford geologic model used in this study was provided by the operator. It contains 4 different formation: Austin Chalk, Upper Eagle Ford, Lower Eagle Ford, and Buda as shown in Figure 4-1. The average thickness is about 450 ft. The pay zones are Upper and Lower Eagle Ford and the average pay thickness is around 270 ft. Austin Chalk and Buda are included to serve as the geomechanical boundaries and provide additional zones that hydraulic fractures can propagate into. The flow and geomechanical properties

are also included in the model as shown in Figure 4-2. The summary of property ranges is shown in Table 4.1. The permeability is homogeneous by zone, while the porosity, Young's Modulus, and Poisson's Ratio are spatially heterogeneous.

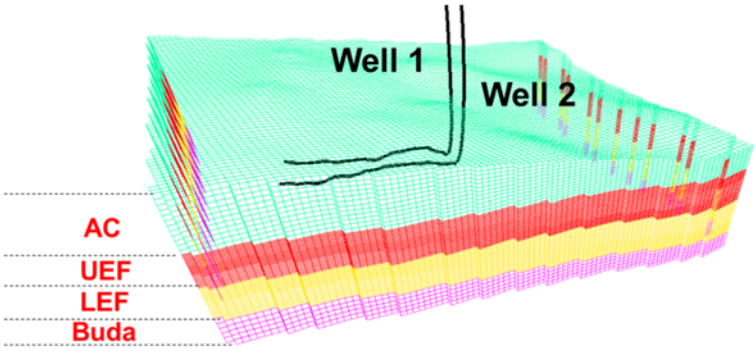

Figure 4-1. Schematic diagram of the reservoir geologic model and the corresponding well location.

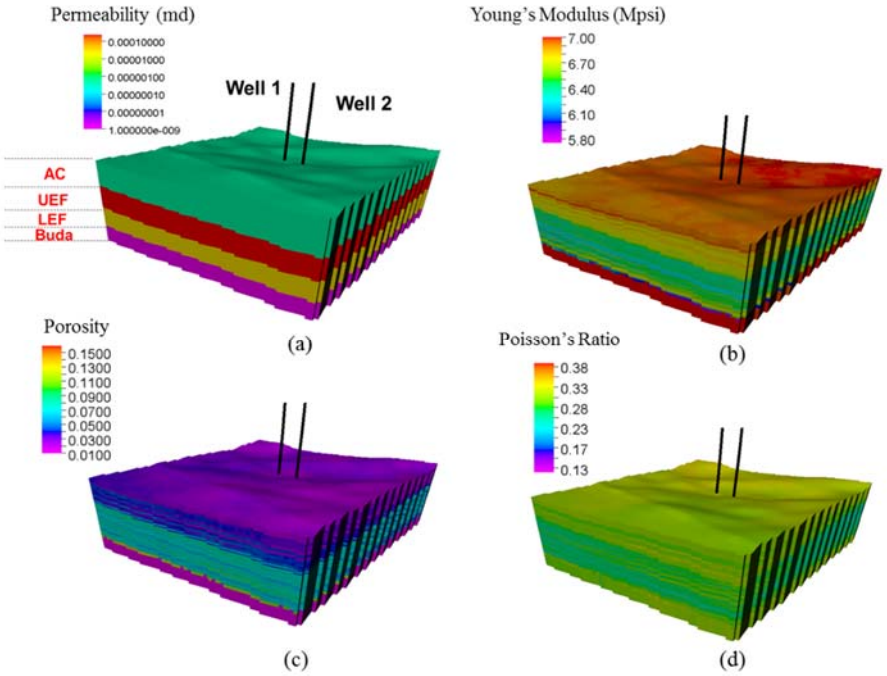

Figure 4-2. Flow and goemechanical properties of the model: (a) Permeability (b) Young's Modulus (c) Porosity (d) Poisson's Ratio.

Table 4.1. Summary of property ranges in different formations.

Property	Austin Chalk	Upper Eagle Ford	Lower Eagle Ford	Buda
Permeability (nd)	0.5	230	30	0.001
Porosity	0.01-0.05	0.01-0.09	0.01-0.11	0.01-0.16
Young's Modulus (Mpsi)	6.58-7.03	5.99-6.87	6.09-6.91	5.75-7.13
Poisson's Ratio	0.27-0.34	0.21-0.34	0.21-0.31	0.12-0.38
Average Thickness (ft)	110	130	140	70

Two horizontal wells are completed side by side in the upper Eagle Ford formation. The well spacing is 1200 ft and it is sufficiently large to prevent well interference. The summary of the two well completion information provided by the operator is shown in Table 2.1. Both wells use the same total number of perforations per stage. Well 2 has a much tighter cluster spacing compared to well 1 and well 2 also uses more fluid and more proppants. Both wells use the same type of fracturing fluid and proppant to reduce the impact of the fluid and proppant selection. This is a unique field pilot test to investigate the influence of tighter cluster spacing on the fracture propagation and production performance in the Eagle Ford field.

Table 4.2. Summary of the completion data for the two wells.

Well Name	Well 1	Well 2
Cluster Spacing (ft)	50	20
Cluster Count per Stage	5	10
Number of Stages	26	31
Number of Perforations per Cluster	6	3
Mass of Proppant (lb)	10,000,000	13,000,000
Type of Proppant	100 Mesh, 40/70 White	100 Mesh, 40/70 White
Volume of Fluid (bbl)	150,000	350,000
Type of Fracturing Fluid	Slickwater, HCL 7.5, 8# vis-link	Slickwater, HCL 7.5, 8# vis-link

4.4. Fracture Geometry Calibration Using Injection Treatment Pressure

We first need to calibrate the fracture geometry using the injection treatment pressure. The operator provided the wellhead treatment pressure of a typical stage. As suggested in the previous literature, there is typically no fracture interference between stages in the Eagle Ford formation (Simpson et al., 2016). Thus, the calibrated parameters from the single stage history matching can be used to propagate fractures for all other stages. Mangrove® is used as the forward fracture propagation simulator. It uses Unconventional Fracture Model (UFM) to model hydraulic fracture geometry under the impact of reservoir structure, geomechanical containment, local natural fracture network, and stress shadow (Kresse et al., 2011; Weng et al., 2011; Suarez and Pichon, 2016).

To calibrate the fracture geometry, we need to minimize the misfit of injection treatment pressure as follows:

$$obj = \log\left(\sum_{j=1}^{2}\sqrt{\sum_{i=1}^{Ntime}(ITP_{i,j}^{obs} - ITP_{i,j}^{cal})^2}\right) \tag{4.1}$$

where N_{time} is the total number of pressure data observation times, *ITP* is the injection treatment pressure, the superscript *obs* indicates the observed data, and the superscript *cal* indicates the calculated value from Mangrove®.

Table 4.3. Base case properties for fracture propagation.

Parameter	Value
Minimum Horizontal Stress	0.85 psi/ft
Stress Anisotropy (S_{Hmax}/S_{Hmin})	1.4
Leak-off Coefficient	7.5e-4 ft/min^1/2
Fracture Height H_f	450 ft
Young's Modulus	Spatially Heterogeneous
Poisson's Ratio	Spatially Heterogeneous

Before history matching, we first run sensitivity analysis to determine the parameters that have the highest impact on the misfit function in Eq. (4.1). These parameters will be altered in the calibration step to match the observed injection treatment pressure. Figure 4-3 shows the sensitivity of the injection treatment pressure misfit to different parameters. The most sensitive parameters are the fracture height and the leak off coefficient multiplier, followed by the minimum horizontal stress gradient. For the manual injection pressure history matching, the fracture height and the leak off coefficient multiplier are altered because they are the heavy hitters with high uncertainty in the field.

The minimum horizontal stress gradient has much lower uncertainty because it can be measured using mini-frac test in the field. Thus, it is not included in the history matching.

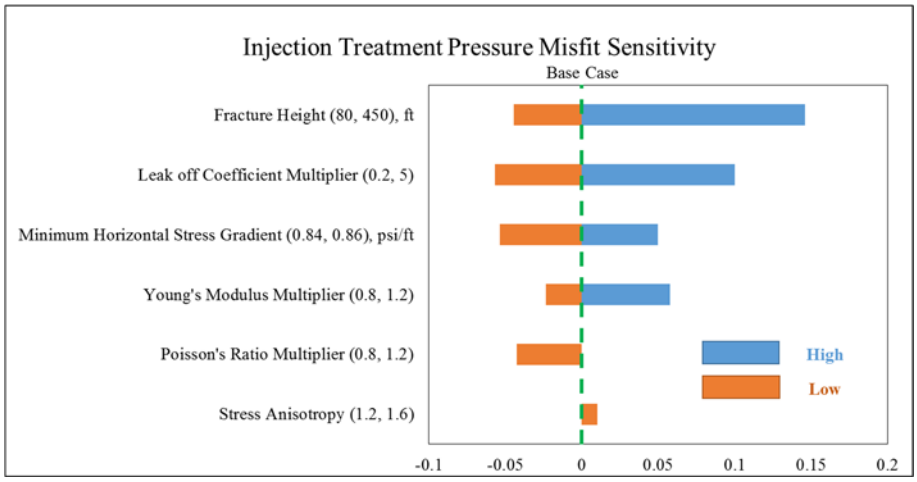

Figure 4-3. Injection treatment pressure misfit sensitivity.

Injection Treatment Pressure Misfit						
Leak off Coefficient Multiplier \ Fracture Height (ft)	50	100	150	200	250	450
0.2	24	12	9	13	14	15
1	16	8	9.5	13	14	16
2	13	4	10	13.5	14.5	16
3	13	4.5	11	14	15	17
4	12	8	12	14.6	15	18
5	12	11	13	15	17	22

Figure 4-4. Manual history matching matrix.

Figure 4-4 provides the manual history matching matrix for the injection treatment pressure misfit. Using the matrix, we can explore the plausible solution space and identify an initial estimate on what parameter combination can achieve relative low misfit values.

If we focus on the dark green low misfit region, we can see that the fracture height should be around 100 ft and the leak off coefficient multiplier should be between 2 and 3. After obtaining this initial estimate, we conduct a fine-tuning of the two parameters near the dark green region to further reduce the misfit. Figure 4-5 shows the initial results of the injection treatment pressure for well 1 and 2 where there is a large discrepancy between observed data and simulation results. Figure 4-6 shows the final matched results of the two wells. After the injection treatment pressure history matching, we generate 3 fracture models with fracture heights of 80, 100 and 120ft with different leak-off coefficient multipliers. The three models are used as the starting point of the production data history matching. The three different fracture models are shown in Figure 4-7. All three fracture models suggest that the hydraulic fractures are mostly planar and well 1 with wide cluster spacing tends to develop longer fractures. The fracture geometry is fixed for the following production history matching.

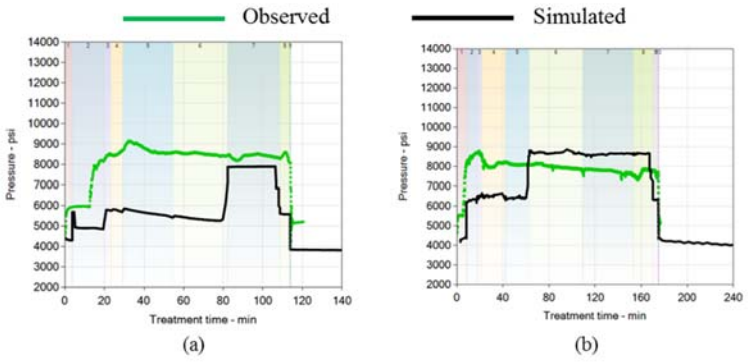

Figure 4-5. Initial results of the injection treatment pressure (a) Well 1 (b) Well 2.

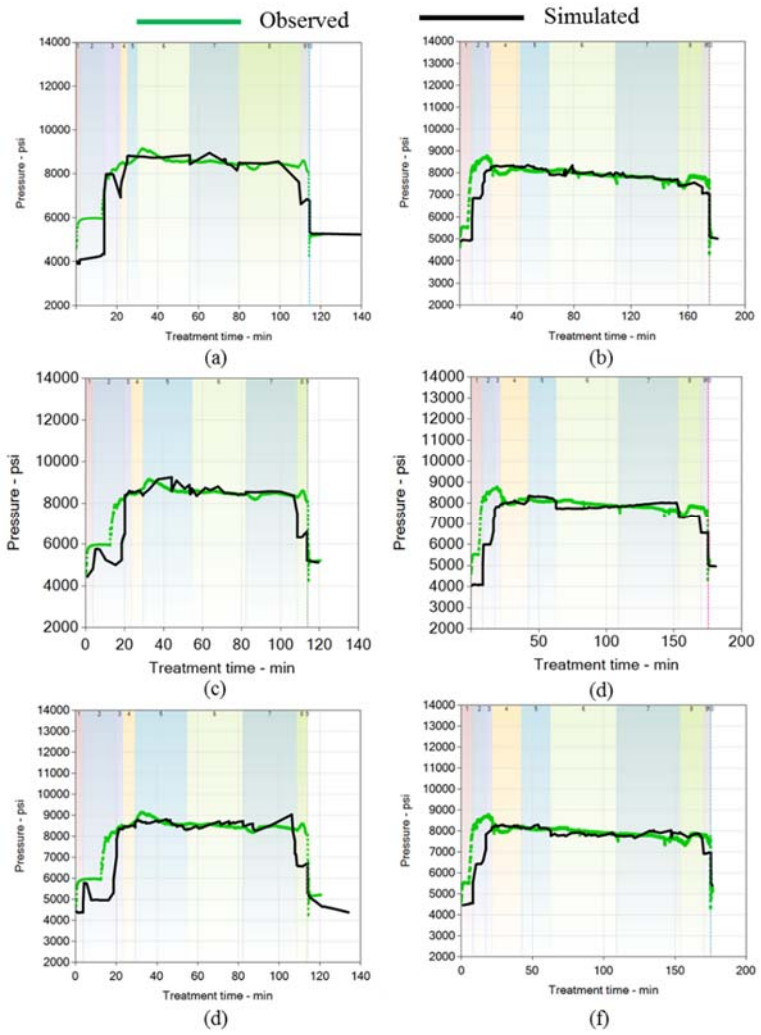

Figure 4-6. Matched results of the injection treatment pressure (a) Well 1 Hf=120ft Leak-off Multiplier=2 (b) Well 2 Hf=120ft Leak-off Multiplier=2 (c) Well 1 Hf=100ft Leak-off Multiplier=2.6 (d) Well 2 Hf=100ft Leak-off Multiplier=2.6 (e) Well 1 Hf=80ft Leak-off Multiplier=3 (f) Well 2 Hf=80ft Leak-off Multiplier=3.

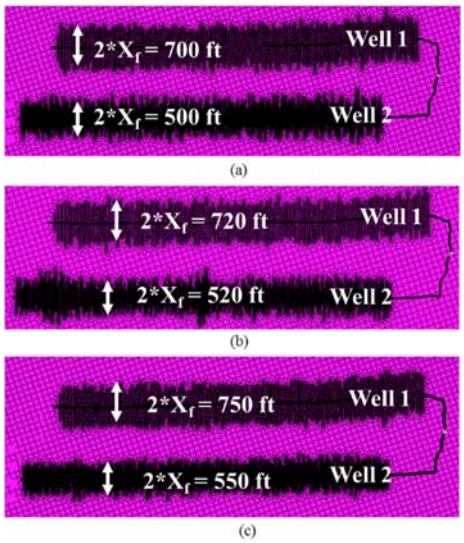

Figure 4-7. Fracture models after fracture geometry calibration (a) Hf=120ft (b) Hf=100ft (c) Hf=80ft.

4.5. Fracture and Reservoir Property Calibration Using Production Response

We use the Fast Marching Method (FMM) based flow simulation as the forward simulation tool for the production history matching (Zhang et al., 2016). It transforms the 3-D flow equation into equivalent 1-D flow equation along the diffusive time of flight (DTOF) coordinate and the flow equation can be efficiently solved on the 1-D DTOF coordinate (King et al., 2016; Zhang et al., 2016; Iino et al., 2017). It has been shown in previous studies that the computation speed-up and accuracy of the FMM-based flow simulation are particularly well-suited for field scale history matching and optimization problems (Cui et al., 2016; Iino et al., 2017; Iino and Datta-Gupta, 2018; Xue et al., 2019; Zhang and Zhu, 2019b). In this study, the three-phase production and the bottomhole pressure data for both wells are available for 1 year as shown in Figure 4-8. Although the operator used a more aggressive pressure depletion strategy for well 1, well 2 has a better

production performance. Both wells have high water production at the early time from the flow back fluids.

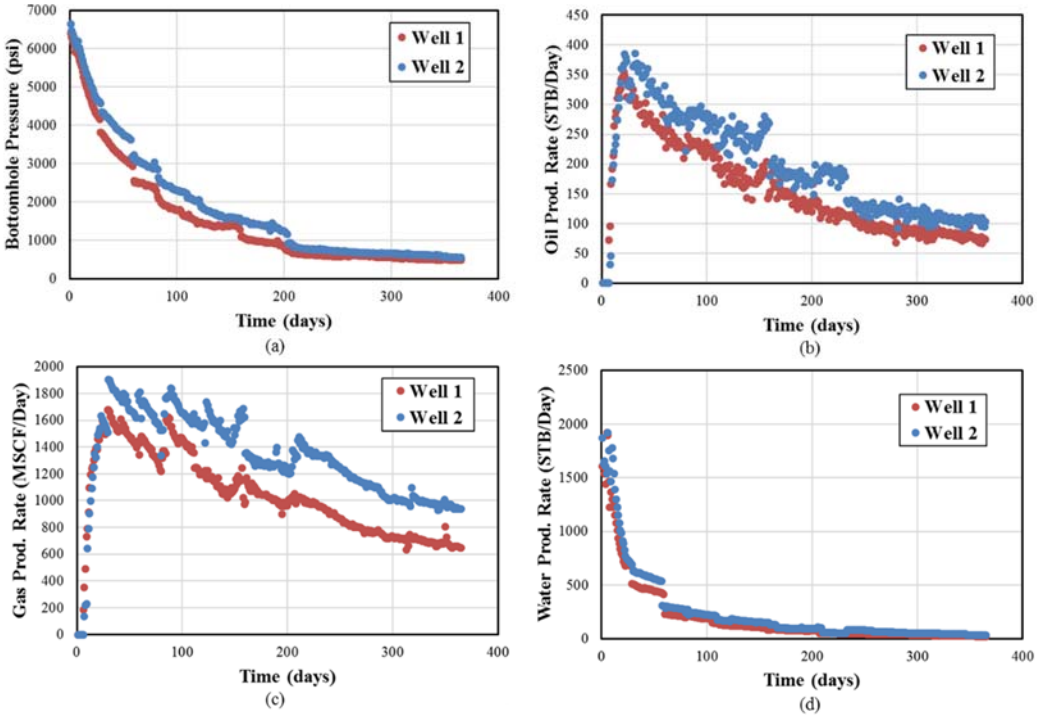

Figure 4-8. Two wells production data (a) Bottomhole pressure (b) Oil production rate (c) Gas production rate (d) Water production rate.

With the production response, we can calculate the well drainage volume based on the concept of the rate normalized pressure (RNP) (Song and Ehlig-Economides, 2011). The RNP approximation represents the production behavior that would be observed if the well were produced at a constant reference rate. The well drainage volume can be calculated using the following equation (Xue et al., 2018)

$$\frac{1}{V_d(t_e)} \approx c_t \frac{d}{dt_e}\left(\frac{\Delta p_{wf}(t_e)}{q_w(t_e)}\right) \tag{4.2}$$

where V_d is the drainage volume, P_{wf} is the bottomhole flowing pressure, q_w is the well flow rate, and t_e is the material balance time defined as

$$t_e = \frac{Q(t)}{q_w(t)} \tag{4.3}$$

where Q is the cumulative production.

The well drainage volume comparison of the two wells is shown in Figure 4-9. Well 2 not only has better production performance, it also has a higher drainage volume.

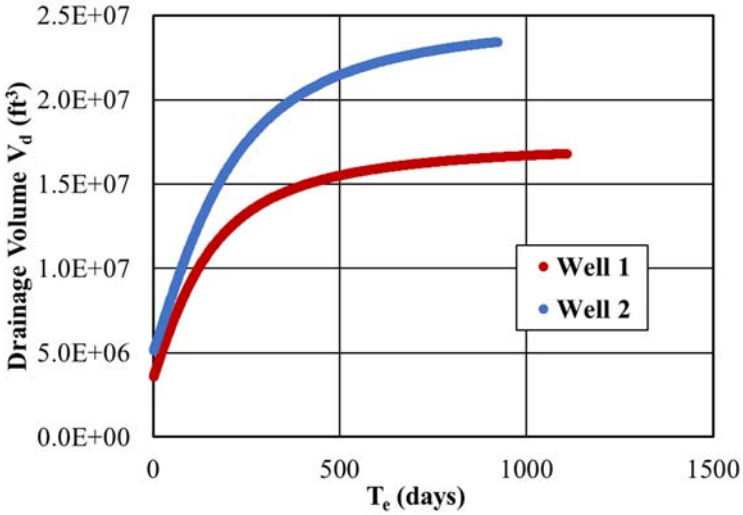

Figure 4-9. Drainage volume comparison of the two wells.

The initial models for production history matching are based on three fracture (permeability/porosity) models generated by the calibration of the injection phase modeling as discussed before. Since the hydraulic fractures do not penetrate into Austin Chalk and Buda for all three fracture models, only the upper and lower Eagle Ford formations are included in the production simulation. Figure 4-10 (a) shows the 3D view of the simulation model. The simulation model has approximately 1 million grid cells. It

is a gas condensate reservoir and the fluid PVT is provided by the operator. Figure 4-10 (b) gives the top view for the fracture model of 100-ft fracture height. The black boxes are the stimulated reservoir volume (SRV) regions created around each well. The SRV regions are used to model the complex fracture networks beyond the explicit hydraulic fractures (Mayerhofer et al., 2010). The SRV properties can be tuned during the calibration process to history match the production response (Iino et al., 2017; Park and Janova, 2019). The maximum fracture conductivity per fracture stage is shown in Figure 4-11. The colors tell what SRV regions each fracture stage belongs to.

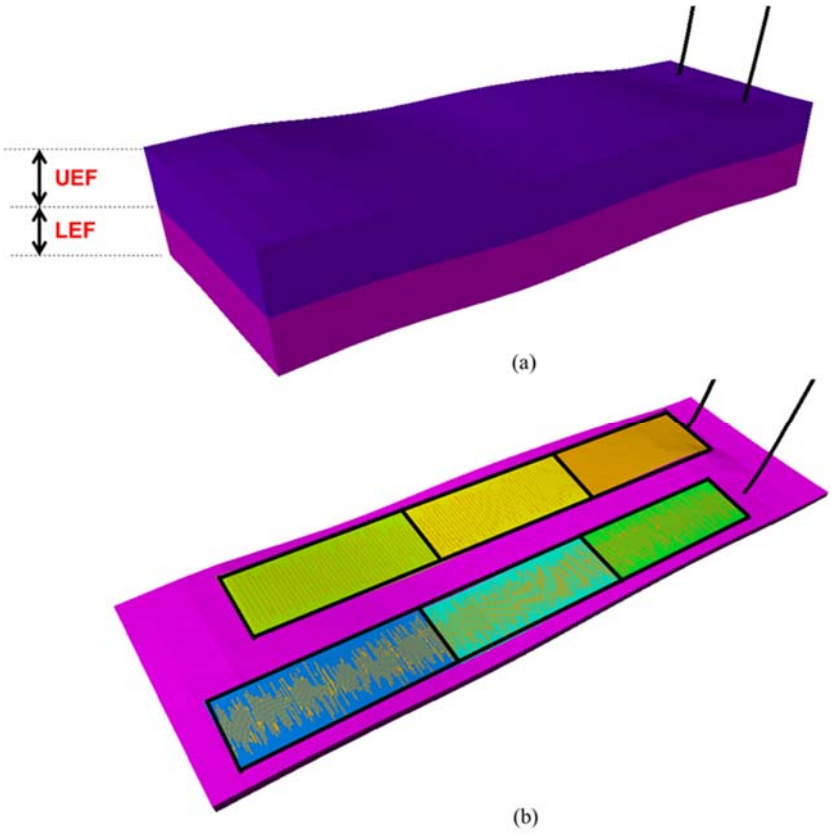

Figure 4-10. Base case simulation model of H_f=100ft (a) 3D view (b) top view hydraulic fracture.

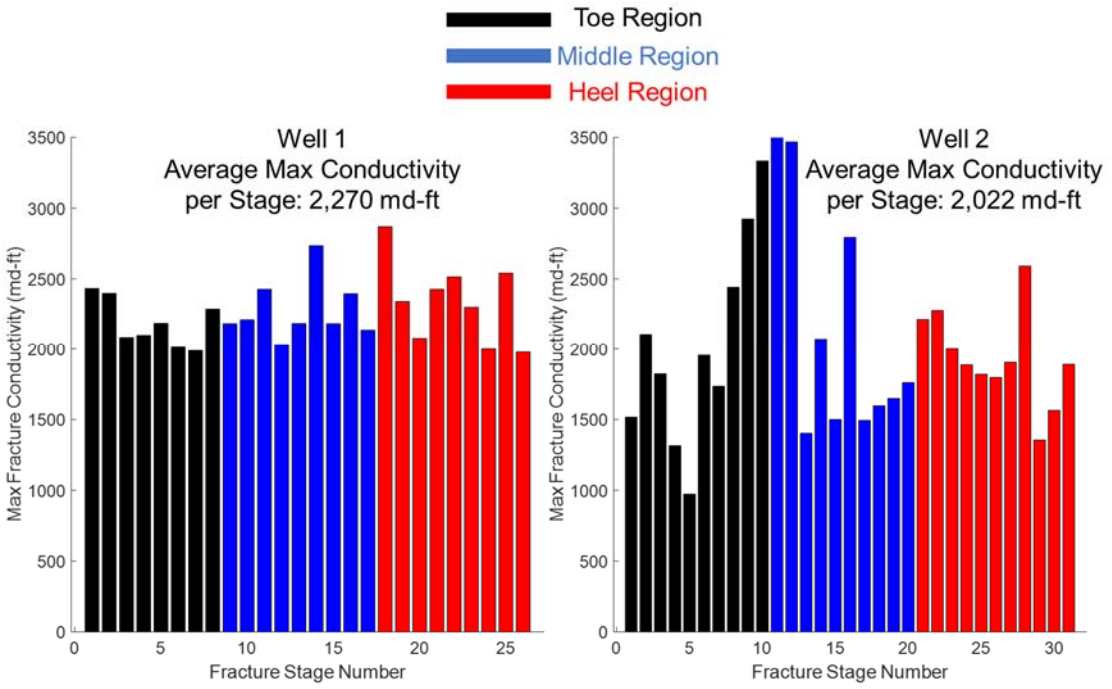

Figure 4-11. Maximum hydraulic fracture conductivity per stage for both wells.

For the production history matching, we minimize two misfit functions: cumulative production misfit and drainage volume misfit. The cumulative production misfit can be defined as

$$obj1 = \ln\left|\Delta\text{Cum\_oil}\right| + \ln\left|\Delta\text{Cum\_water}\right| + \ln\left|\Delta\text{Cum\_gas}\right| \tag{4.4}$$

where Δ represents the differences between simulation and observe data at each time step:

$$\left|\Delta y\right| \equiv \sqrt{\frac{1}{N_t}\sum_{i=1}^{N_t}\left|y_i^{\text{sim}} - y_i^{\text{obs}}\right|^2} \tag{4.5}$$

where N_t represents the total number of time steps and y_i represents cumulative oil, water and gas production of a given time.

The drainage volume misfit is given as:

$$obj2 = \ln\left|\Delta DV\right| \tag{4.6}$$

For the drainage volume misfit, the observed drainage volume is calculated using Eq. (4.2) as shown in Figure 4-9. The advantage of including drainage volume as an objective function is that often time there are a lot of noises in the raw production data. The drainage volume is smoother and it contains more information about reservoir heterogeneity. The simulated drainage volume can be obtained using the FMM-based black oil simulation as shown in Figure 4-12 (Iino et al., 2017). First, we calculate the multi-phase diffusivity on each grid block. Second, using the multi-phase diffusivity as an input parameter, we run the FMM to calculate the DTOF on each grid block. Third, we accumulate pore volume using DTOF as a spatial coordinate. Then, we convert the DTOF (τ) to physical time using the relation $t = \frac{\tau^2}{4}$ (Xie et al., 2015).

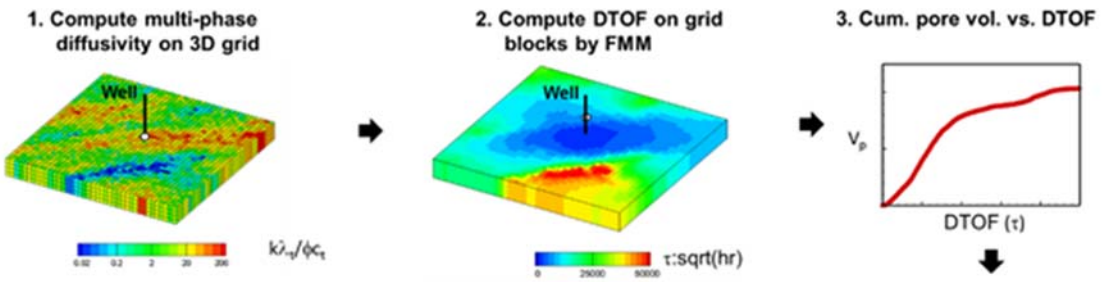

Figure 4-12. Drainage volume calculation using the FMM-based simulation reprinted from Iino et al. (2017).

Before we run the production response history matching, we first perform sensitivity study of the two misfit functions to identify the heavy hitters. The parameter range for production history matching is shown in Table 4.4. The results of sensitivity analyses are shown in Figure 4-13. For the cumulative production sensitivity, the fracture

related properties have a substantial impact. Also, the SRV permeability and water saturation are shown to be very important. For the drainage volume sensitivity, the heavy hitters are the fracture permeability SRV permeability, SRV porosity, and water saturation and the fracture model. Summarizing the sensitivity analyses, the hydraulic fracture permeability, hydraulic fracture compaction, SRV permeability, SRV porosity, water saturation, and the permeability/porosity model from injection calibration are heavy hitters and they will be altered during the production history matching.

Table 4.4. Production history matching parameter.

Regions	Uncertain parameters	Low	Base	High
Reservoir	Permeability/porosity model number	1	2	3
Hydraulic Fracture	Porosity multiplier	0.5	1	2
	Permeability multiplier	0.01	1	100
	S_{wi}	0.2	0.4	1.0
	Compaction table	1	4	7
SRV	Porosity multiplier	0.5	1	2
	Permeability multiplier	0.01	1	100
	S_{wi}	0.2	0.4	1
Matrix	Porosity multiplier	0.8	1	1.2
	Permeability multiplier	0.01	1	100

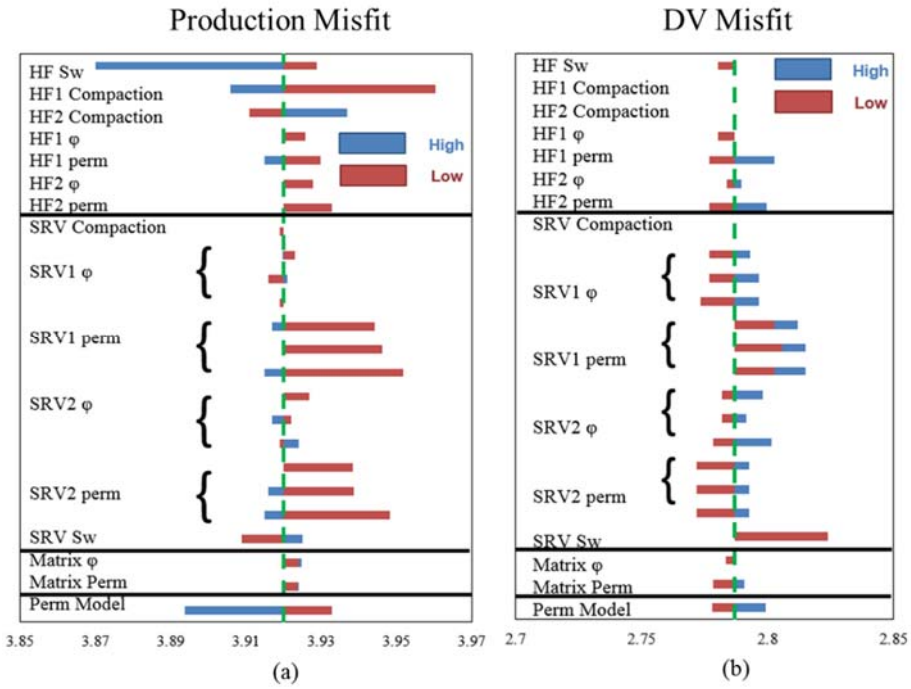

Figure 4-13. Sensitivity analyses for (a) cumulative production misfit and (b) drainage volume misfit. HF: hydraulic fracture, numeric number: well number, φ: porosity, perm: permeability, SRV: stimulated reservoir volume, Sw: water saturation, perm model: permeability models generated from Mangrove®.

In this history matching, we use the population size of 120 and run for 50 generations. Figure 4-14 shows the drainage volume misfit and production misfit before and after the history matching. For generation 1, the solutions are scattered as GA is exploring the entire solution space. For generation 50, the solutions move towards the bottom left, indicating misfit reduction of both misfit functions. In generation 50, we can clearly see a Pareto front, indicating the trade-off between the two objective functions.

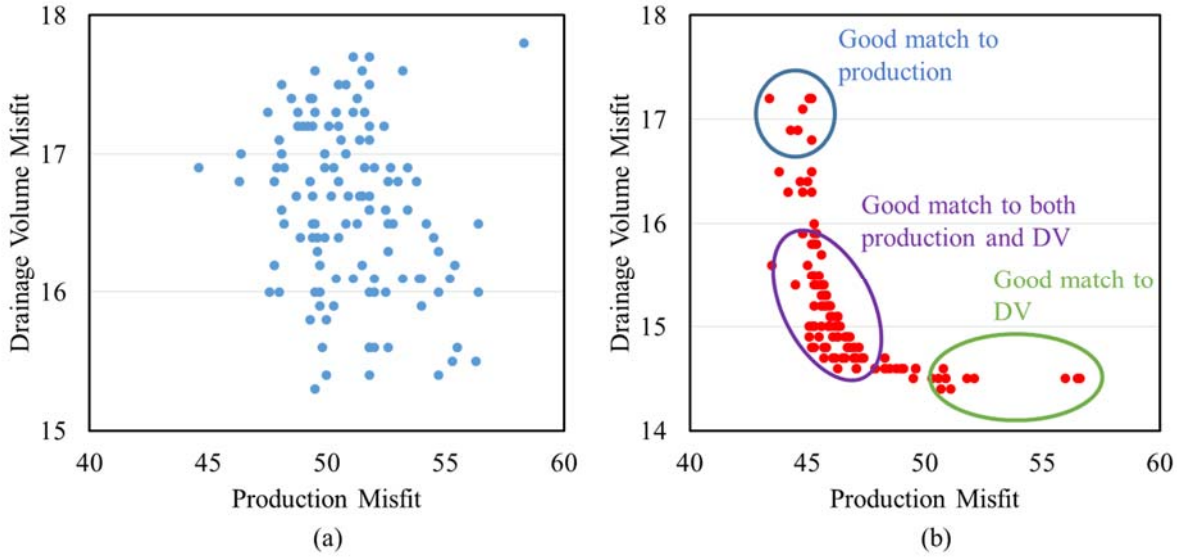

Figure 4-14. Drainage volume misfit and production misfit for (a) Generation 1 and (b) Generation 50.

Figure 4-15 and Figure 4-16 compare the observed data and simulation results for well 1 and well 2. As expected, the results from generation 1 are scattered. After the history matching, the selected solutions show good match for both the observed drainage volume and cumulative production with some variations in both history matching period and the validation period. Since GA is a stochastic optimization algorithm, multiple models are obtained after history matching instead of a single best model.

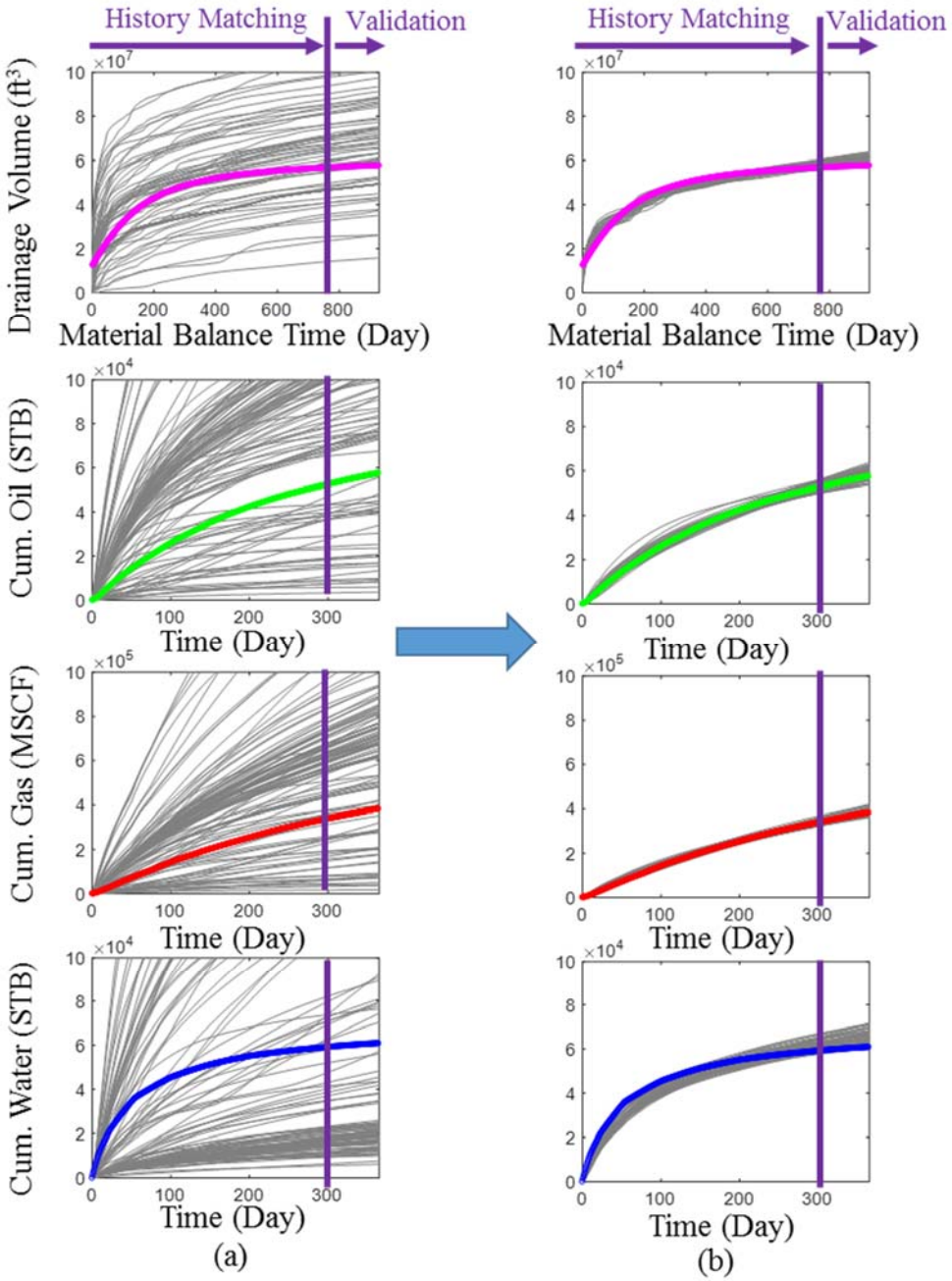

Figure 4-15. Comparison of observed data (color line) and simulated results (grey line) for well 1 (a) Generation 1 (b) Selected results using threshold from Generation 50.

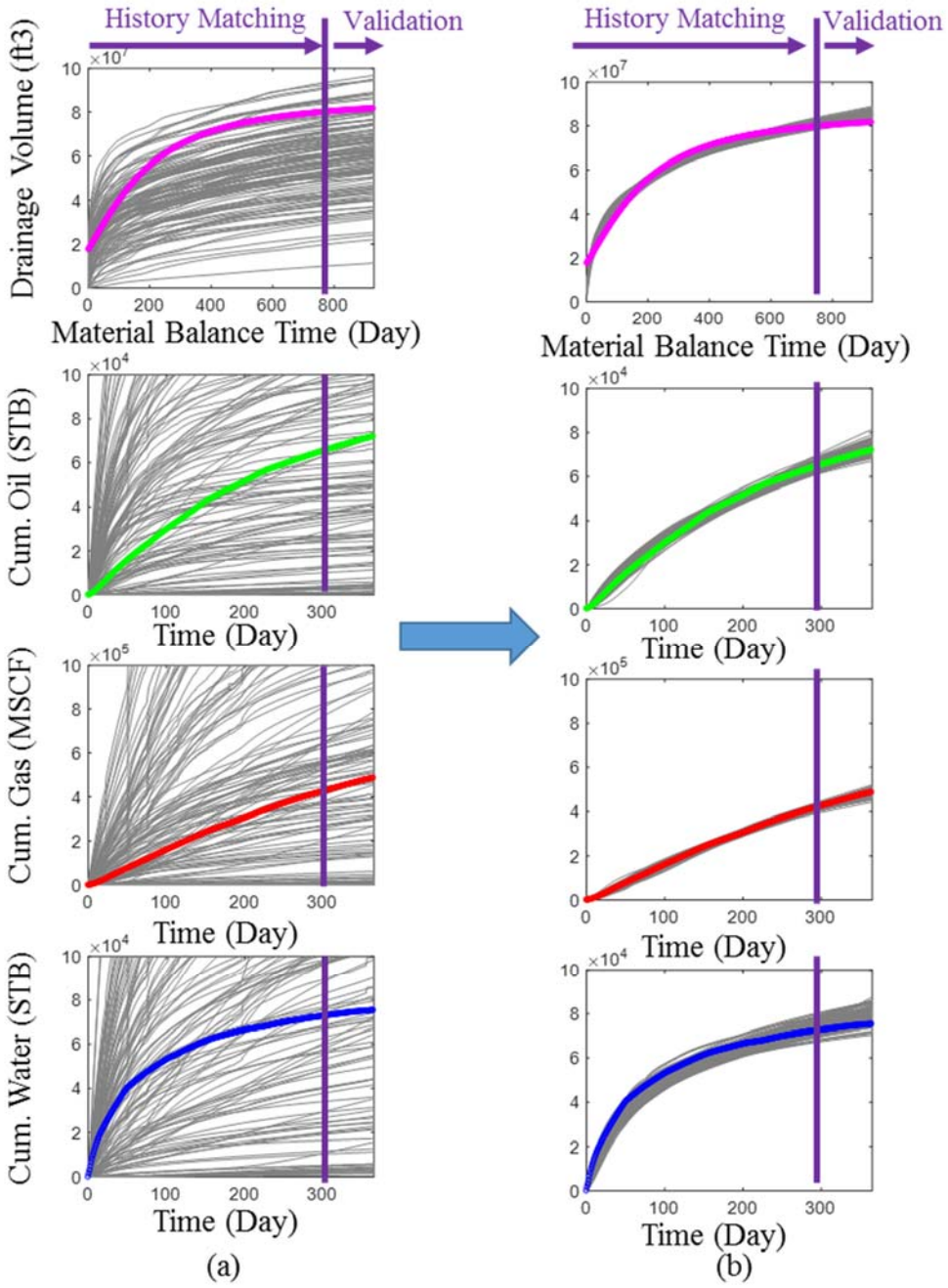

Figure 4-16. Comparison of observed data and simulated results for well 2 (a) Generation 1 (b) Selected results using threshold from Generation 50.

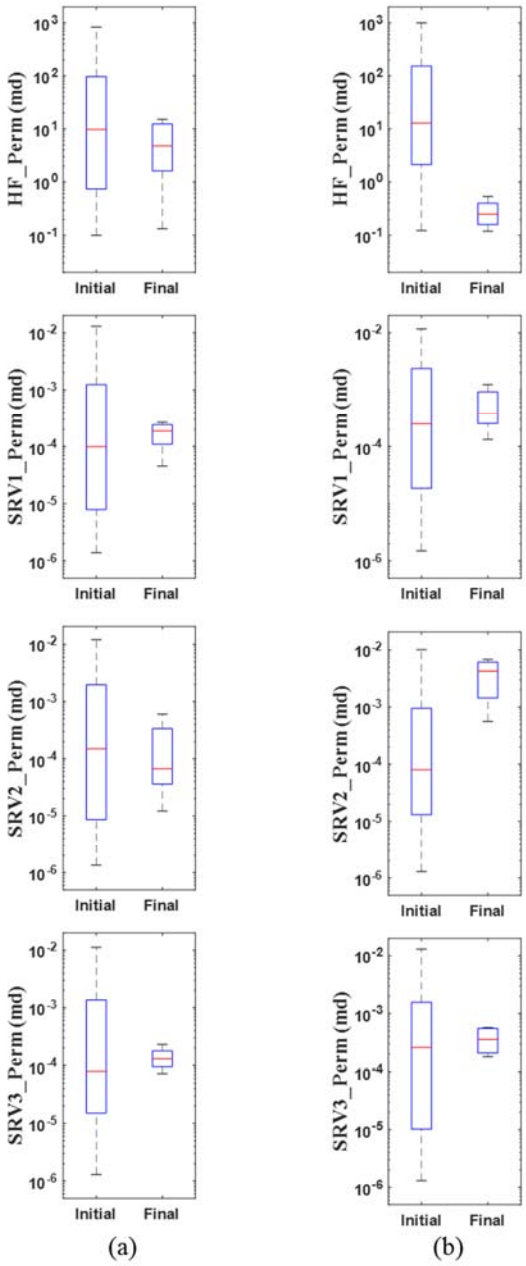

Figure 4-17. Permeability uncertainty ranges before and after the history matching 50 (a) Well 1 (b) Well 2

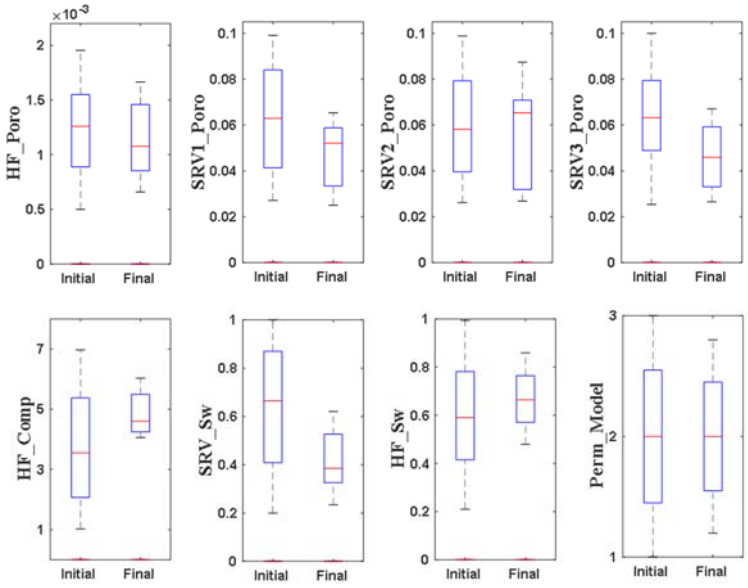

Figure 4-18. Parameters ranges before and after the history matching for Well 1.

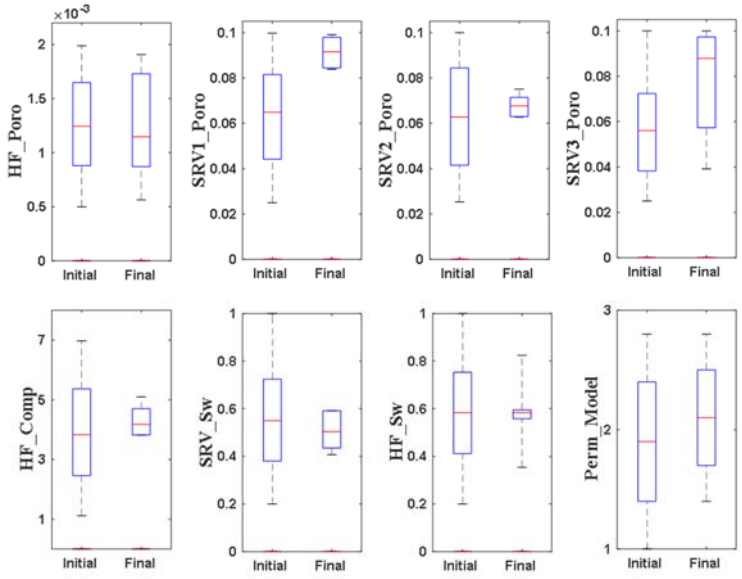

Figure 4-19. Parameters ranges before and after the history matching for Well 2.

We further analyze the parameter uncertainty ranges for well 1 and well 2 using boxplots before and after the history matching. Figure 4-17 focus on the permeability of

the fracture and the SRV region. Well 2 with tighter cluster spacing has lower fracture permeability but higher SRV permeability as compared to well 1. The tighter cluster spacing completion is more likely to introduce a more severe stress shadowing effect, resulting in the low fracture permeability. However, the tighter cluster spacing design creates more complex fracture networks near the hydraulic fractures. This enhanced permeability networks are captured as better SRV permeability by the history matching. Thus, despite having shorter and less permeability fractures, well 2 has better SRV permeability, leading to larger drainage volume and better production performance. Figure 4-18 and Figure 4-19 show the other parameters uncertainty range before and after the history matching for well 1 and well 2. For most of the parameters, the uncertainty ranges are reduced significantly after the history matching.

4.6. Flow Diagnostic Plot

In our previous study by Xue et al. (2018), we developed several novel diagnostic plots to characterize the reservoir and fracture systems. In this study, we follow our previous method to understand the flow regimes of the two Eagle Ford wells. We generate the pressure contour maps of a set of fractures planes for Well 2 in Figure 4-20 and the flow diagnostic plots (Figure 4-21). In the diagnostic plots, the drainage volume Vd can be calculated using Eq. (4.2) and the $w(\tau)$ function is the first derivative of drainage volume over τ, which indicates how fast the drainage volume increases. This $w(\tau)$ function can give us the information such as fracture surface area and flow regimes. The drainage volume and $w(\tau)$ function can be linked using Eq. (4.7) (Xue et al., 2018). After calculating the drainage volume Vd, we invert for the $w(\tau)$ function using a piecewise

constant representation. The detailed methodology to invert the w(τ) function from the drainage volume can be found in our previous study (Xue et al., 2018).

$$V_d(t) = \int_0^{\infty} d\tau \cdot w(\tau) e^{-\frac{\tau^2}{4t}} \tag{4.7}$$

The w(τ) diagnostic plot agrees with the observations from the pressure contours. At early time, the w(τ) function increases at a higher rate, indicating the fracture flow as shown in Figure 4-20 (a). At intermediate time, the w(τ) function increases at a slower rate, indicating the combination of the formation linear flow and the partial completion flow as shown in Figure 4-20 (b). At late time, the w(τ) function decreases indicating fracture interference as shown in Figure 4-20 (c). We also compare the w(τ) plots for both wells in Figure 4-22. Well 2 has a higher w(τ) function compared well 1, indicating a larger fracture surface area. Since well 2 uses a tighter cluster spacing design, it tends to develop a more complex fracture network, leading to a larger fracture surface area.

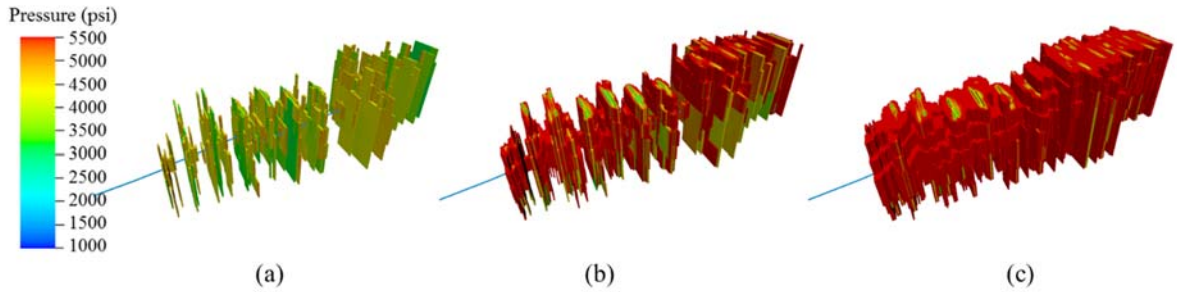

Figure 4-20. Pressure contours from the side view of the fracture plane for well 2 (a) at early time fracture flow (b) immediate time partial completion (c) late time fracture interference.

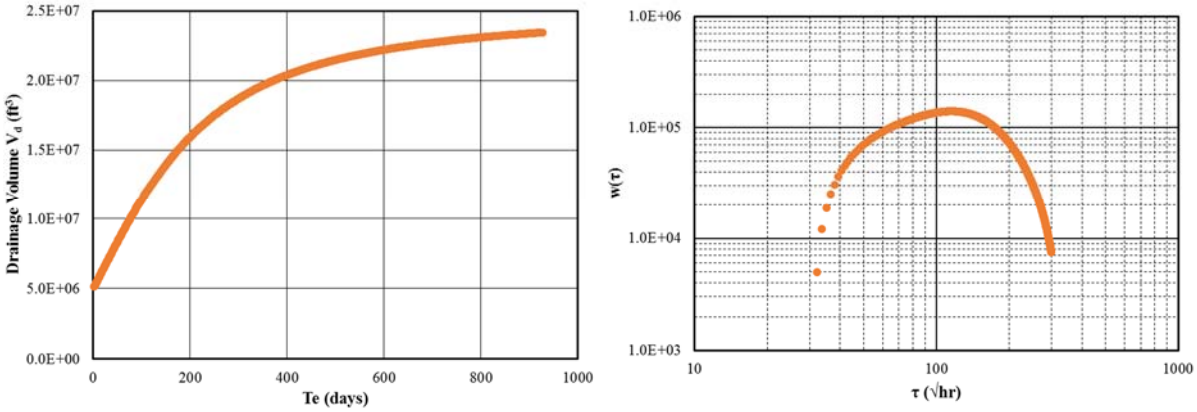

Figure 4-21. Flow diagnostic plots for well 2.

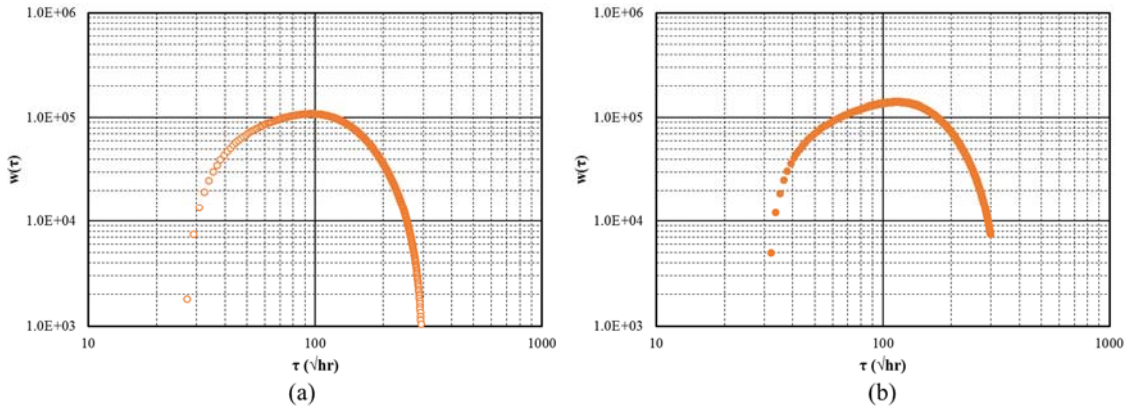

Figure 4-22. *w(τ)* flow diagnostic plots for (a) well 1 and (b) well 2.

4.7. Conclusions

We utilize a commercial fracture propagation model Mangrove® and the Fast Marching Method (FMM) based black oil simulation as the forward simulators to conduct a field injection-to-production history matching. The field data used in this history matching study is designed to understand the impact of tighter cluster spacing on the fracture and well performance. We analyze the history matching results to examine the impact of tighter cluster spacing on the fractures and well performance. Some key conclusions are summarized as follows:

- We demonstrate the feasibility of the history matching workflow using Mangrove® and the FMM-based black oil simulation in Eagle Ford field case study.
- The injection phase history matching shows that most fractures are planar in Eagle Ford because of the high stress anisotropy. The well with tighter cluster spacing tends to develop shorter fractures.
- The production phase history matching shows that the well with tighter cluster spacing has smaller fracture permeability but better SRV permeability in Eagle Ford. The better SRV quality results in better drainage volume and production performance.
- The tighter cluster spacing completion is more favorable in the Eagle Ford formation because there is minimal fracture interference.

5. CONCLUSIONS

Coupled fluid flow and geomechanical simulation have wide applications on evaluating the complex phenomena associated with pressure and stress/strain throughout the life cycle of the unconventional shale development. In this dissertation, we apply coupled fluid flow and geomechanical simulation to reveal the mechanisms of induced seismicity, to predict the seismicity risks, and to understand the characteristics of hydraulic fractures under different completion designs.

First, we use 3-D fluid flow and poroelastic simulation models to review the driving mechanism of the induced seismicity in the Azle area. The results suggest no fluid movement or pressure increase in the crystalline basement, although there is plastic strain accumulation for the weaker elements along the fault in the basement. The accumulation of plastic strain change appears to be caused by the unbalanced loading on different sides of the fault due to the differential in fluid injection and production. Even though the low-permeability faults in the basement are not in pressure communication with the Ellenburger formation, the poroelastic stresses transmitted to the basement can trigger seismicity without elevated pore pressure.

Second, we build a detailed Azle fault model using the high resolution seismic picks provided by the operator. A finite difference flow simulation model (CMG) and a finite element geomechanical model (ABAQUS) are built using the detailed fault model. We develop the workflow to couple the two simulations to explicitly model fault slips and dissipated energy in the Azle site. The results suggest that the slips can occur at the

location where there is no pressure change. The radiated energy from observed seismic events is about 20% of the dissipated energy calculated from the simulation results.

Third, we use the coupled simulation to investigate the impact of cluster spacing on hydraulic fracture design using the Eagle Ford field data. The results suggest that most fractures are planar in Eagle Ford because of the high stress anisotropy. The well with tighter cluster spacing tends to develop shorter fractures. The well with tighter cluster spacing has better SRV permeability in the Eagle Ford, leading to better drainage volume and production performance. The tighter cluster spacing completion is more favorable in the Eagle Ford formation because there is minimal fracture interference.

REFERENCES

Ahmed, T., 2018, Reservoir Engineering Handbook: Gulf Professional Publishing.

Aki, K., and P. G. Richards, 2002, Quantitative Seismology: University Science Books.

Ansari, A. M., N. D. Sylvester, O. Shoham, and J. P. Brill, 1990, A Comprehensive Mechanistic Model for Upward Two-Phase Flow in Wellbores: Presented at SPE Annual Technical Conference and Exhibition, 23-26 September, New Orleans, Louisiana, USA. SPE-20630-MS.

Beggs, D. H., and J. P. Brill, 1973, A Study of Two-Phase Flow in Inclined Pipes: Journal of Petroleum Technology, **25**, 607-617.

Bittencourt, A. C., and R. N. Horne, 1997, Reservoir Development and Design Optimization: Presented at SPE Annual Technical Conference and Exhibition , 5-8 October, San Antonio, Texas, USA. SPE-38895-MS.

Bradley, H. B., 1987, Petroleum Engineering Handbook: Society of Petroleum Engineers.

Breiman, L., J. Friedman, C. J. Stone, and R. A. Olshen, 1984, Classification and Regression Trees: Taylor & Francis.

Castiñeira, D., B. Jha, and R. Juanes, 2016, Uncertainty Quantification and Inverse Modeling of Fault Poromechanics and Induced Seismicity: Application to a Synthetic Carbon Capture and Storage (CCS) Problem: Presented at 50th US Rock Mechanics/Geomechanics Symposium, 26-29 June, Houston, Texas, USA. ARMA-2016-151.

Chang, K. W., and P. Segall, 2016a, Injection-Induced Seismicity on Basement Faults Including Poroelastic Stressing: Journal of Geophysical Research: Solid Earth, **121**, 2708-2726.

Chang, K. W., and P. Segall, 2016b, Seismicity on Basement Faults Induced by Simultaneous Fluid Injection–Extraction: Pure and Applied Geophysics, **173**, 2621-2636.

Chang, K. W., and H. Yoon, 2018, 3-D Modeling of Induced Seismicity Along Multiple Faults: Magnitude, Rate, and Location in a Poroelasticity System: Journal of Geophysical Research: Solid Earth, **123**, 9866-9883.

Chen, N. H., 1979, An Explicit Equation for Friction Factor in Pipe: Industrial & Engineering Chemistry Fundamentals, **18**, 296-297.

Chen, R., X. Xue, A. Datta-Gupta, H. Yu, and N. Kalyanaraman, 2019, The Impact of Cluster Spacing on Multi-Fractured Well Performance: Presented at SPE Liquids-Rich Basins Conference - North America, 7-8 November, Odessa, Texas, USA. SPE-197103-MS.

Chen, R., X. Xue, J. Park, A. Datta-Gupta, and M. J. King, 2020, New Insights into the Mechanisms of Seismicity in the Azle Area, North Texas: Geophysics, **85**, EN1-EN15.

Chen, R., X. Xue, C. Yao, A. Datta-Gupta, M. J. King, P. Hennings, and R. Dommisse, 2018, Coupled Fluid Flow and Geomechanical Modeling of Seismicity in the Azle Area North Texas: Presented at SPE Annual Technical Conference and Exhibition, 24-26 September, Dallas, Texas, USA. SPE-191623-MS.

Cipolla, C. L., E. Lolon, M. J. Mayerhofer, and N. R. Warpinski, 2009, Fracture Design Considerations in Horizontal Wells Drilled in Unconventional Gas Reservoirs: Presented at SPE Hydraulic Fracturing Technology Conference, 19-21 January, The Woodlands, Texas, USA. SPE-119366-MS.

Computer Modeling Group, 2016, Stars User Guide (Version 2016.10): Computer Modeling Group Ltd.

Cui, J., C. Yang, D. Zhu, and A. Datta-Gupta, 2016, Fracture Diagnosis in Multiple-Stage-Stimulated Horizontal Well by Temperature Measurements with Fast Marching Method: SPE Journal, **21**, 2289-2300.

Dahm, T., and F. Krüger, 2014, Topic Moment Tensor Inversion and Moment Tensor Interpretation, New Manual of Seismological Observatory Practice (Nmsop-2): Potsdam: Deutsches GeoforschungZentrum GFZ.

Dake, L. P., 1983, Fundamentals of Reservoir Engineering: Elsevier.

DeShon, H. R., C. T. Hayward, P. O. Ogwari, L. Quinones, O. Sufri, B. Stump, and M. Beatrice Magnani, 2018, Summary of the North Texas Earthquake Study Seismic Networks, 2013–2018: Seismological Research Letters, **90**, 387-394.

Drillinginfo, 2018, Drillinginfo Production, https://info.drillinginfo.com/, accessed May 1, 2018.

Economides, M. J., A. D. Hill, C. Ehlig-Economides, and D. Zhu, 2013, Petroleum Production Systems: Pearson Education.

Ellsworth, W. L., 2013, Injection-Induced Earthquakes: Science, **341**, 1225942.

Evans, S., S. Siddiqui, and J. Magness, 2018, Impact of Cluster Spacing on Infill Completions in the Eagle Ford: Presented at SPE/AAPG/SEG Unconventional Resources Technology Conference , 23-25 July, Houston, Texas, USA. URTEC-2899323-MS.

Ewing, T. E., 1991, The Tectonic Framework of Texas: Bureau of Economic Geology, University of Texas at Austin.

Fan, Z., P. Eichhubl, and J. F. Gale, 2016, Geomechanical Analysis of Fluid Injection and Seismic Fault Slip for the Mw4. 8 Timpson, Texas, Earthquake Sequence: Journal of Geophysical Research: Solid Earth, **121**, 2798-2812.

Fanning, J. T., 1896, A Practical Treatise on Hydraulic and Water-Supply Engineering: D. Van Nostrand Company.

Frohlich, C., H. DeShon, B. Stump, C. Hayward, M. Hornbach, and J. I. Walter, 2016, A Historical Review of Induced Earthquakes in Texas: Seismological Research Letters, **87**, 1022-1038.

Frohlich, C., C. Hayward, B. Stump, and E. Potter, 2011, The Dallas–Fort Worth Earthquake Sequence: October 2008 through May 2009: Bulletin of the Seismological Society of America, **101**, 327-340.

Goldberg, D. E., 1989, Genetic Algorithms in Search, Optimization and Machine Learning: Addison-Wesley Longman Publishing Co., Inc.

Gono, V., J. E. Olson, and J. F. Gale, 2015, Understanding the Correlation between Induced Seismicity and Wastewater Injection in the Fort Worth Basin: Presented

at 49th U.S. Rock Mechanics/Geomechanics Symposium, , 28 June-1 July, San Francisco, California, USA. ARMA-2015-419.

Govier, G. W., and K. Aziz, 1972, The Flow of Complex Mixtures in Pipes: Van Nostrand Reinhold Company.

Hennings, P., A. Savvaidis, M. Young, E. Rathje, M. Babazadeh, T. Borgfeldt, R. Chen, A. Datta-Gupta, H. DeShon, P. Eichhubl, Z. Fan, C. Frohlich, V. Gono, J. Kim, M. King, C. Lemons, T. Mukherjee, J.-P. Nicot, J. Olson, J. Park, J. Walter, X. Xue, H. Yoon, B. Young, and G. Zalachoris, 2016, Report on House Bill 2 (2016-17) Seismic Monitoring and Research in Texas, http://www.beg.utexas.edu/files/texnet-cisr/Report%20Assets/TexNet-Report-2016.pdf, accessed 2 September 2019.

Hennings, P. H., J. E. Lund Snee, J. L. Osmond, H. R. DeShon, R. Dommisse, E. Horne, C. Lemons, and M. D. Zoback, 2019, Injection-Induced Seismicity and Fault-Slip Potential in the Fort Worth Basin, Texas: Bulletin of the Seismological Society of America, **109**, 1615-1634.

Hornbach, M. J., H. R. DeShon, W. L. Ellsworth, B. W. Stump, C. Hayward, C. Frohlich, H. R. Oldham, J. E. Olson, M. B. Magnani, and C. Brokaw, 2015, Causal Factors for Seismicity near Azle, Texas: Nature communications, **6**, 6728.

Hornbach, M. J., M. Jones, M. Scales, H. R. DeShon, M. B. Magnani, C. Frohlich, B. Stump, C. Hayward, and M. Layton, 2016, Ellenburger Wastewater Injection and Seismicity in North Texas: Physics of the Earth and Planetary Interiors, **261**, 54-68.

Iino, A., and A. Datta-Gupta, 2018, Optimizing CO2 and Field Gas Injection Eor in Unconventional Reservoirs Using the Fast Marching Method: Presented at SPE Improved Oil Recovery Conference, 14-18 April, Tulsa, Oklahoma, USA. SPE-190304-MS.

Iino, A., A. Vyas, J. Huang, A. Datta-Gupta, Y. Fujita, N. Bansal, and S. Sankaran, 2017, Efficient Modeling and History Matching of Shale Oil Reservoirs Using the Fast Marching Method: Field Application and Validation: Presented at SPE Western Regional Meeting, 23-27 April, Bakersfield, California, USA. SPE-185719-MS.

Kanamori, H., 1977, The Energy Release in Great Earthquakes: Journal of geophysical research, **82**, 2981-2987.

Keranen, K. M., M. Weingarten, G. A. Abers, B. A. Bekins, and S. Ge, 2014, Sharp Increase in Central Oklahoma Seismicity since 2008 Induced by Massive Wastewater Injection: Science, **345**, 448-451.

King, M. J., Z. Wang, and A. Datta-Gupta, 2016, Asymptotic Solutions of the Diffusivity Equation and Their Applications: Presented at SPE Europec featured at 78th EAGE Conference and Exhibition, 30 May-2 June, Vienna, Austria. SPE-180149-MS.

Kresse, O., C. Cohen, X. Weng, R. Wu, and H. Gu, 2011, Numerical Modeling of Hydraulic Fracturing in Naturally Fractured Formations: Presented at 45th U.S. Rock Mechanics / Geomechanics Symposium, 26-29 June, San Francisco, California, USA. ARMA-11-363.

Lee, W. J., and R. A. Wattenbarger, 1996, Gas Reservoir Engineering: Society of Petroleum Engineers.

Lele, S. P., S. Y. Hsu, J. L. Garzon, N. DeDontney, K. H. Searles, G. A. Gist, P. F. Sanz, E. A. Biediger, and B. A. Dale, 2016, Geomechanical Modeling to Evaluate Production-Induced Seismicity at Groningen Field: Presented at Abu Dhabi International Petroleum Exhibition & Conference, 7-10 November, Abu Dhabi, UAE. SPE-183554-MS.

Lolon, E., C. Cipolla, L. Weijers, R. E. Hesketh, and M. W. Grigg, 2009, Evaluating Horizontal Well Placement and Hydraulic Fracture Spacing/Conductivity in the Bakken Formation, North Dakota: Presented at SPE Annual Technical Conference and Exhibition, 4-7 October, New Orleans, Louisiana, USA. SPE-124905-MS.

Loucks, R. G., R. M. Reed, S. C. Ruppel, and D. M. Jarvie, 2009, Morphology, Genesis, and Distribution of Nanometer-Scale Pores in Siliceous Mudstones of the Mississippian Barnett Shale: Journal of Sedimentary Research, **79**, 848-861.

Lund Snee, J. E., and M. D. Zoback, 2016, State of Stress in Texas: Implications for Induced Seismicity: Geophysical Research Letters, **43**, 10,208-214.

Mayerhofer, M. J., E. Lolon, N. R. Warpinski, C. L. Cipolla, D. W. Walser, and C. M. Rightmire, 2010, What Is Stimulated Reservoir Volume?: SPE Production & Operations, **25**, 89-98.

McCain, W. D., 1990, The Properties of Petroleum Fluids: PennWell Books.

McGarr, A., D. Simpson, L. Seeber, and W. Lee, 2002, Case Histories of Induced and Triggered Seismicity: International Geophysics Series, **81**, 647-664.

Miller, C. K., G. A. Waters, and E. I. Rylander, 2011, Evaluation of Production Log Data from Horizontal Wells Drilled in Organic Shales: Presented at North American Unconventional Gas Conference and Exhibition, 14-16 June, The Woodlands, Texas, USA. SPE-144326-MS.

Mishra, S., and A. Datta-Gupta, 2017, Applied Statistical Modeling and Data Analytics: A Practical Guide for the Petroleum Geosciences: Elsevier.

National Research Council, 2013, Induced Seismicity Potential in Energy Technologies: National Academies Press.

Park, H. Y., A. Datta-Gupta, and M. J. King, 2015, Handling Conflicting Multiple Objectives Using Pareto-Based Evolutionary Algorithm During History Matching of Reservoir Performance: Journal of Petroleum Science and Engineering, **125**, 48-66.

Park, J., A. Iino, A. Datta-Gupta, J. Bi, and S. Sankaran, 2019, Rapid Modeling of Injection and Production Phases of Hydraulically Fractured Shale Wells Using the Fast Marching Method: Presented at SPE/AAPG/SEG Unconventional Resources Technology Conference, 22-24 July, Denver, Colorado, USA. URTEC-2019-339-MS.

Park, J., and C. Janova, 2019, SRV Characterization and Optimum Lateral Well Spacing Study of Two-Well Pad in Midland Basin: Presented at SPE/AAPG/SEG Unconventional Resources Technology Conference, 22-24 July, Denver, Colorado, USA. URTEC-2019-93-MS.

Park, J., and J. Kim, 2016, Importance of Fluid Compressibility and Multi-Phase Flow in Numerical Modeling of Hydraulic Fracture Propagation: Presented at 50th U.S. Rock Mechanics/Geomechanics Symposium, 26-29 June, Houston, Texas, USA. ARMA-2016-444

Park, J., J. Kim, and D. Zhu, 2016, Assessment of Potential Fault Activation in Tarim Basin During Hydraulic Fracturing Operations by Using Rigorous Simulation of Coupled Flow and Geomechanics: Presented at SPE Asia Pacific Hydraulic Fracturing Conference, 24-26 August, Beijing, China. SPE-181811-MS.

Pioneer Natural Resources Company, 2018, Pioneer Natural Resources Company Reports Third Quarter 2018 Financial and Operating Results, http://investors.pxd.com/news-releases/news-release-details/pioneer-natural-resources-company-reports-third-quarter-2018, accessed 2019/02/06 2018.

Pollastro, R. M., D. M. Jarvie, R. J. Hill, and C. W. Adams, 2007a, Geologic Framework of the Mississippian Barnett Shale, Barnett-Paleozoic Total Petroleum System, Bend Arch-Fort Worth Basin, Texas: AAPG bulletin, **91**, 405-436.

Pollastro, R. M., D. M. Jarvie, R. J. Hill, and C. W. Adams, 2007b, Geologic Framework of the Mississippian Barnett Shale, Barnett-Paleozoic Total Petroleum System, Bend Archfort Worth Basin, Texas: AAPG bulletin, **91**, 405-436.

Quinones, L. A., H. R. DeShon, M. B. Magnani, and C. Frohlich, 2018, Stress Orientations in the Fort Worth Basin, Texas, Determined from Earthquake Focal Mechanisms: Bulletin of the Seismological Society of America, **108**, 1124-1132.

Railroad Commission of Texas, 2015a, Proposal for Decision, Oil and Gas Docket No. 09-0296410, https://www.rrc.state.tx.us/media/31022/09-96410-sho-pfd.pdf, accessed 2 September 2019.

Railroad Commission of Texas, 2015b, Proposal for Decision, Oil and Gas Docket No. 09-0296411, https://www.rrc.state.tx.us/media/31023/09-96411-sho-pfd.pdf, accessed 2 September 2019.

Railroad Commission of Texas, 2018a, H10 Filing System, http://webapps.rrc.state.tx.us/H10/h10PublicMain.do, accessed 1 May 2018.

Railroad Commission of Texas, 2018b, Online Research Queries, https://www.rrc.texas.gov/about-us/resource-center/research/online-research-queries/, accessed 7 November 2018.

Reasenberg, P. A., and R. W. Simpson, 1992, Response of Regional Seismicity to the Static Stress Change Produced by the Loma Prieta Earthquake: Science, **255**, 1687-1690.

Romero, C., and J. Carter, 2001, Using Genetic Algorithms for Reservoir Characterisation: Journal of Petroleum Science and Engineering, **31**, 113-123.

Roussel, N. P., R. Manchanda, and M. M. Sharma, 2012, Implications of Fracturing Pressure Data Recorded During a Horizontal Completion on Stage Spacing Design: Presented at SPE Hydraulic Fracturing Technology Conference, 6-8 February, The Woodlands, Texas, USA. SPE-152631-MS.

Sanz, P. F., S. P. Lele, K. H. Searles, S. Y. Hsu, J. L. Garzon, J. A. Burdette, W. E. Kline, B. A. Dale, and P. D. Hector, 2015, Geomechanical Analysis to Evaluate

Production-Induced Fault Reactivation at Groningen Gas Field: Presented at SPE Annual Technical Conference and Exhibition, , 28-30 September, Houston, Texas, USA. SPE-174942-MS.

Schwab, D. R., T. S. Bidgoli, and M. H. Taylor, 2017, Characterizing the Potential for Injection-Induced Fault Reactivation through Subsurface Structural Mapping and Stress Field Analysis, Wellington Field, Sumner County, Kansas: Journal of Geophysical Research: Solid Earth, **122**, 132-154.

Segall, P., 1989, Earthquakes Triggered by Fluid Extraction: Geology, **17**, 942-946.

Segall, P., J. R. Grasso, and A. Mossop, 1994, Poroelastic Stressing and Induced Seismicity near the Lacq Gas Field, Southwestern France: Journal of Geophysical Research: Solid Earth, **99**, 15423-15438.

Segall, P., and S. Lu, 2015, Injection-Induced Seismicity: Poroelastic and Earthquake Nucleation Effects: Journal of Geophysical Research: Solid Earth, **120**, 5082-5103.

Simpson, M. D., R. Patterson, and K. Wu, 2016, Study of Stress Shadow Effects in Eagle Ford Shale: Insight from Field Data Analysis: Presetned at 50th U.S. Rock Mechanics/Geomechanics Symposium, 26-29 June, Houston, Texas, USA. ARMA-2016-190.

Song, B., and C. A. Ehlig-Economides, 2011, Rate-Normalized Pressure Analysis for Determination of Shale Gas Well Performance: Presented at North American Unconventional Gas Conference and Exhibition, 14-16 June, The Woodlands, Texas, USA. SPE-144031-MS.

Stein, R. S., 1999, The Role of Stress Transfer in Earthquake Occurrence: Nature, **402**, 605-609.

Suarez, M., and S. Pichon, 2016, Combining Hydraulic Fracturing Considerations and Well Spacing Optimization for Pad Development in the Vaca Muerta Shale: Presented at SPE/AAPG/SEG Unconventional Resources Technology Conference, 1-3 August, San Antonio, Texas, USA. URTEC-2436107-MS.

Sullivan, E. C., K. J. Marfurt, A. Lacazette, and M. Ammerman, 2006, Application of New Seismic Attributes to Collapse Chimneys in the Fort Worth Basin: Geophysics, **71**, B111-B119.

Syms, F., 2011, Technical Issues Related to Hydraulic Fracturing and Fluid Extraction/Injection near the Comanche Peak Nuclear Facility in Texas, https://www.nrc.gov/docs/ML1131/ML11314A197.pdf, accessed 2 September 2019.

Taitel, Y., D. Barnea, and A. Dukler, 1982, A Film Model for the Prediction of Flooding and Flow Reversal for Gas-Liquid Flow in Vertical Tubes: International Journal of Multiphase Flow, **8**, 1-10.

Vermeer, P. A., and R. De Borst, 1984, Non-Associated Plasticity for Soils, Concrete and Rock: Heron, **29**, 1-64.

Weng, X., O. Kresse, C. E. Cohen, R. Wu, and H. Gu, 2011, Modeling of Hydraulic Fracture Network Propagation in a Naturally Fractured Formation: Presented at SPE Hydraulic Fracturing Technology Conference, 24-26 January, The Woodlands, Texas, USA. SPE-140253-MS.

Wu, K., J. Olson, M. T. Balhoff, and W. Yu, 2017, Numerical Analysis for Promoting Uniform Development of Simultaneous Multiple-Fracture Propagation in Horizontal Wells: SPE Production & Operations, **32**, 41-50.

Xie, J., C. Yang, N. Gupta, M. J. King, and A. Datta-Gupta, 2015, Depth of Investigation and Depletion in Unconventional Reservoirs with Fast-Marching Methods: SPE Journal, **20**, 831-841.

Xiong, H., W. Wu, and S. Gao, 2018, Optimizing Well Completion Design and Well Spacing with Integration of Advanced Multi-Stage Fracture Modeling & Reservoir Simulation - A Permian Basin Case Study: Presented at SPE Hydraulic Fracturing Technology Conference and Exhibition, 23-25 January, The Woodlands, Texas, USA. SPE-189855-MS.

Xue, X., C. Yang, T. Onishi, M. J. King, and A. Datta-Gupta, 2019, Modeling Hydraulically Fractured Shale Wells Using the Fast Marching Method with Local Grid Refinements LGRs and Embedded Discrete Fracture Model EDFM: SPE Journal. SPE-193822-PA.

Xue, X., C. Yang, J. Park, V. K. Sharma, A. Datta-Gupta, and M. J. King, 2018, Reservoir and Fracture-Flow Characterization Using Novel Diagnostic Plots: SPE Journal, **24**, 1-248.

Yin, J., H. Y. Park, A. Datta-Gupta, M. J. King, and M. K. Choudhary, 2011, A Hierarchical Streamline-Assisted History Matching Approach with Global and Local Parameter Updates: Journal of Petroleum Science and Engineering, **80**, 116-130.

Zhai, G., and M. Shirzaei, 2018, Fluid Injection and Time-Dependent Seismic Hazard in the Barnett Shale, Texas: Geophysical Research Letters, **45**, 4743-4753.

Zhang, S., and D. Zhu, 2019a, Efficient Flow Rate Profiling for Multiphase Flow in Horizontal Wells Using Downhole Temperature Measurement: Presented at International Petroleum Technology Conference, 26-28 March, Beijing, China. IPTC-19138-MS.

Zhang, S., and D. Zhu, 2019b, Inversion of Downhole Temperature Measurements in Multistage Fracture Stimulation in Horizontal Wells in Unconventional Reservoirs: SPE Production & Operations.

Zhang, Y., N. Bansal, Y. Fujita, A. Datta-Gupta, M. J. King, and S. Sankaran, 2016, From Streamlines to Fast Marching: Rapid Simulation and Performance Assessment of Shale-Gas Reservoirs by Use of Diffusive Time of Flight as a Spatial Coordinate: SPE Journal, **21**, 1883-1898.

Zhang, Y., M. Person, J. Rupp, K. Ellett, M. A. Celia, C. W. Gable, B. Bowen, J. Evans, K. Bandilla, P. Mozley, T. Dewers, and T. Elliot, 2013, Hydrogeologic Controls on Induced Seismicity In crystalline Basement Rocks Due to Fluid Injection into Basal Reservoirs: Groundwater, **51**, 525-538.

Zhou, Z., G. Q. Zhang, D. Zhou, Y. Wang, and H. Dong, 2016, Analysis of Shale Gas Hydraulic Fracture Induced Stress and Optimization of Perforation Cluster Spacing: Presented at ISRM International Symposium - EUROCK 2016, 29-31 August, Ürgüp, Turkey. ISRM-EUROCK-2016-191.

Zhu, D., D. Hill, and S. Zhang, 2018, Using Temperature Measurements from Production Logging/Downhole Sensors to Diagnose Multistage Fractured Well Flow Profile: Presented at SPWLA 59th Annual Logging Symposium, 2-6 June, London, UK. SPWLA-2018-PP.

Zhu, J., J. Forrest, H. Xiong, and A. Kianinejad, 2017, Cluster Spacing and Well Spacing Optimization Using Multi-Well Simulation for the Lower Spraberry Shale in Midland Basin: Presented at SPE Liquids-Rich Basins Conference - North America, 13-14 September, Midland, Texas, USA. SPE-187485-MS.

Zoback, M. D., A. Kohli, I. Das, and M. W. McClure, 2012, The Importance of Slow Slip on Faults During Hydraulic Fracturing Stimulation of Shale Gas Reservoirs: Presented at SPE Americas Unconventional Resources Conference, 5-7 June, Pittsburgh, Pennsylvania USA. SPE-155476-MS.

APPENDIX A

PARETO OPTIMIZATION AND GENETIC ALGORITHM BACKGROUND

Dominance relationships among different solutions form the basis of Pareto optimization. For a minimization problem involving n objectives defined by objective functions f_n, solution a dominates over solution b if all objectives functions evaluated at solution a are not greater than those of b, and at least one objective function of a is strictly smaller than the corresponding objective function evaluated at solution b (Park et al., 2015).

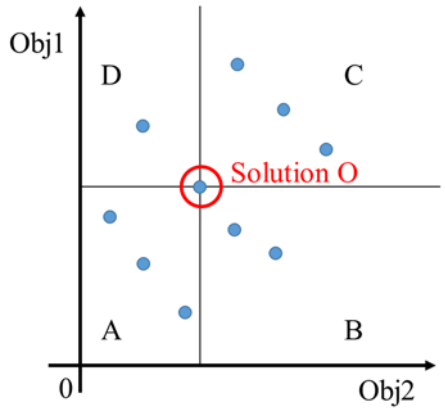

Figure A-1. Dominance concept demonstrated using solution O.

The dominance concept can be graphically demonstrated in Figure A-1. For a two-objective optimization problem, we have solution *O* shown in the red circle. We draw vertical and horizontal lines crossing solution *O* to divide the entire solution space into four regions. In region A, both *obj1* and *obj2* of all three solutions are smaller than those of solution *O.* Thus, solutions in region A are better solutions and dominate solution *O.* Both *obj1* and *obj2* of solutions in region C are larger than those of solution *O,* so solutions

in region C are dominated by solution *O*. In regions B and D, solutions have one objective smaller but the other objective larger than that of solution *O*. Thus, there is no dominance relationship between region B and D solutions and solution *O*.

Similar exercise can be performed on every solution to obtain the overall ranking of the solution. In Figure A-2, a set of solutions which are not dominated by any other solutions are classified as rank 1 solutions. When rank 1 solutions are excluded from the solution space, the same exercise is performed in the new solution space to obtain rank 2 solutions. Then, both rank 1 and rank 2 solutions are excluded to obtain the next rank level of non-dominated solutions. The process is continued until all solutions are assigned a rank level (Park et al., 2015).

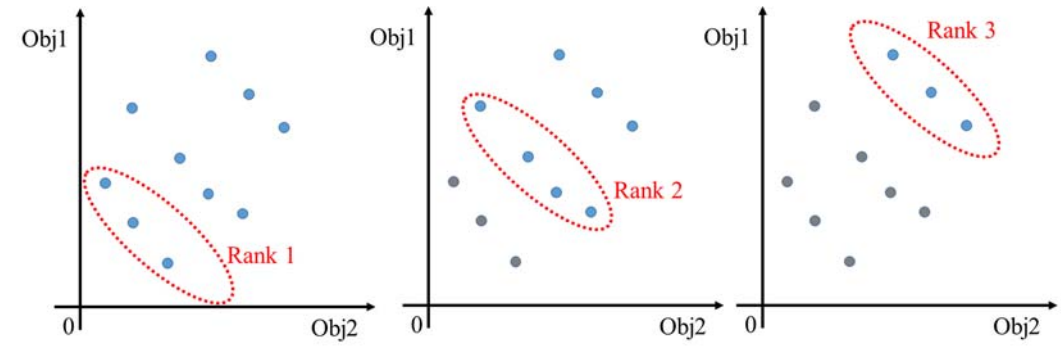

Figure A-2. Solution ranking demonstration.

The solution ranking exhibits the following features: (1) solutions on the same rank or same Pareto front are equally optimal, (2) the lower rank solutions are more competitive than the higher rank ones for a minimization problem, and (3) trade-offs of the front reveal potential conflict between objectives.

The genetic algorithm (GA) is one of the evolutionary methods for solving optimization problems (Goldberg, 1989). It imitates biological principles of evolution – natural selection and survival of the fittest. It has been extensively applied to history matching problems (Bittencourt and Horne, 1997; Romero and Carter, 2001; Yin et al., 2011; Iino et al., 2017; Park et al., 2019).

In the genetic algorithm, a population of candidate solutions to an optimization problem evolves toward better solutions. Each candidate solution has a set of properties which can be mutated and altered. At the initialization step, the population is generated randomly, providing the range of possible solutions (the search space). During each successive generation, a portion of the existing population is selected to breed a new generation. Individual solutions are selected through a fitness-based process, where fitter solutions (as measured by a fitness function) are more likely to be selected. Certain selection methods rate the fitness of each solution and preferentially select the best solutions. The next step is to generate a second generation population of solutions from those selected through a combination of genetic operators: crossover (also called recombination), and mutation. For each new solution to be produced, a pair of "parent" solutions is selected for breeding from the pool selected previously. By producing a "child" solution using the above methods of crossover and mutation, a new solution is created which typically shares many of the characteristics of its "parents". New parents are selected for each new child, and the process continues until a new population of solutions of appropriate size is generated. These processes ultimately result in the next generation population that is different from the initial generation. Generally the average

fitness will have increased by this procedure for the population, since only the best organisms from the first generation are selected for breeding, along with a small proportion of less fit solutions. These less fit solutions ensure genetic diversity within the genetic pool of the parents and therefore ensure the genetic diversity of the subsequent generation of children.

APPENDIX B

TUBING HEAD PRESSURE (THP) TO BOTTOM HOLE PRESSURE (BHP)

The THP to BHP calculation is routine in the petroleum engineering literature (Govier and Aziz, 1972; Beggs and Brill, 1973; Chen, 1979; Taitel et al., 1982; Bradley, 1987; Ansari et al., 1990; Economides et al., 2013). The calculation below follows Economides et al. (2013). Since both Azle injection wells are wastewater disposal wells, a single-phase incompressible flow model will be used. The Reynolds number needs to be calculated to determine if the flow is laminar or turbulent

$$N_{re} = \frac{D u \rho}{\mu}, \tag{B-1}$$

where D is the wellbore diameter, u is the average velocity, ρ is the fluid density, and μ is the fluid viscosity. If N_{re} is larger than 2100 (Economides et al., 2013), it is turbulent flow. Otherwise, it is laminar flow.

The overall pressure drop between the well head and the bottom hole consists of three parts: potential energy, kinetic energy, and frictional pressure drop

$$\Delta p = \Delta p_{PE} + \Delta p_{KE} + \Delta p_F . \tag{B-2}$$

Since there is no change in the inner diameter of the disposal well and thus no change in the velocity of the fluid $\Delta p_{KE} = 0$. Δp_{PE} accounts for the pressure change due to the weight of the column of fluid. Since the injected fluid is water, the potential energy change is low and it can be calculated as:

$$\Delta p_{PE} = \frac{g}{g_c} \rho \Delta Z , \tag{B-3}$$

where ΔZ is the difference in elevation. The frictional pressure drop Δp_F can be obtained from the Fanning equation (Fanning, 1896):

$$\Delta p_F = \frac{2 f_f \rho u^2 L}{g_c D}, \tag{B-4}$$

where u is the velocity and f_f is the Fanning friction factor:

$$f_f = \begin{cases} \dfrac{16}{N_{re}}, N_{re} < 2100 \\ \dfrac{1}{-4\log\left(\dfrac{\epsilon}{3.7065} - \dfrac{5.0452}{N_{re}} * \log\left(\dfrac{\epsilon^{1.1098}}{2.8257} + \left(\dfrac{7.149}{N_{re}}\right)^{0.8981}\right)\right)^2}, N_{re} > 2100 \cdot \end{cases} \tag{B-5}$$

APPENDIX C

GAS PRODUCTION CALCULATION

In this paper, we convert gas production at the surface condition to the reservoir condition, a routine calculation in reservoir engineering (Dake, 1983; McCain, 1990; Lee and Wattenbarger, 1996; Economides et al., 2013; Ahmed, 2018). The surface gas rate for 70 wells can be obtained from Railroad Commission of Texas (2018b). The total cumulative production in both surface and reservoir conditions are shown in Figure C-1. A sample calculation for reservoir gas withdrawal rates is provided below.

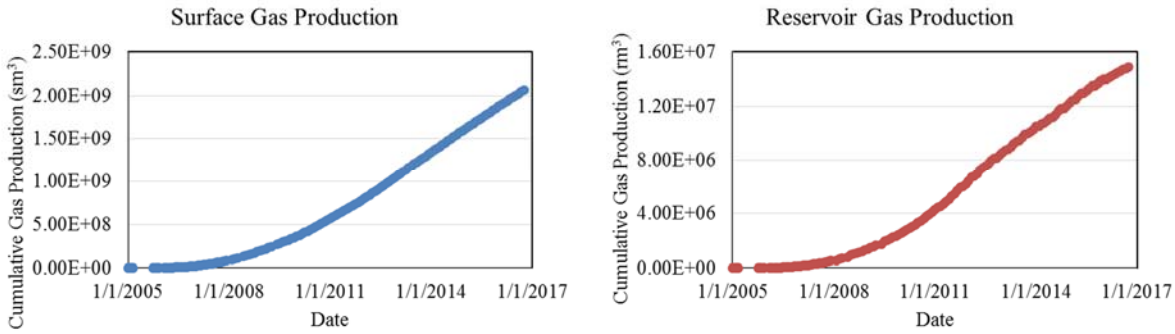

Figure C-1. Cumulative gas production for 70 wells at surface and reservoir conditions.

The gas formation volume factor, B_g, defined as the ratio of the volume of gas at the reservoir temperature and pressure to the volume at the standard temperature and pressure, can be calculated by rearranging the real gas equation (Dake, 1983):

$$B_g = \frac{V_{res}}{V_{sc}} = \frac{\mathrm{p}_{sc} zT}{Z_{sc} T_{sc} \mathrm{p}_{res}}. \tag{C-1}$$

The standard condition pressure and temperature are:

$$\mathrm{p}_{sc} = 101\, kPa\,(14.7\, psi) \tag{C-2}$$

$$T_{sc} = 15.7\,°C\,(520°R) \tag{C-3}$$

We use a pressure gradient of 10.2kPa/m (0.45psi/ft) and a geothermal gradient of 0.0219°C/m (12°F/1000ft) (Syms, 2011). The average depth for Barnett is 2100m (6888ft). We can then calculate reservoir pressure and temperature.

$$p_{res} = 21374\,kPa\,(3100\,psi) \tag{C-4}$$

$$T_{res} = 62\,°C\,(603°R) \tag{C-5}$$

The only unknown is the gas compressibility factor, Z, which requires the gas composition. The gas composition is shown in Table C-1 (Pollastro et al., 2007a).

Table C-1. Gas composition and critical pressure and temperature calculation.

	C_1	C_2	C_3	CO_2	N_2	Mixture
Gas Composition	93.7	2.6	0	2.7	1	
Critical Temperature (°R)	343.30	549.90	666.10	547.80	227.40	
Critical Pressure (psi)	666.00	708.00	616.00	1071.60	493.10	
$y_i T_c$	321.67	14.30	0	14.79	2.27	353.0
$y_i P_c$	624.04	18.41	0	28.93	4.93	676.3

Knowing the gas compressibility, we estimate the Z-factor to be 0.82 (McCain, 1990). Substituting back into equation. C-1,

$$B_g = 0.00451 \frac{rm^3}{sm^3}, \tag{C-6}$$

where rm^3 is cubic meter in reservoir conditions and sm^3 is cubic meter in standard conditions.

In our simulation, B_g is a dynamic parameter based on the calculated BHP and Figure C-2.

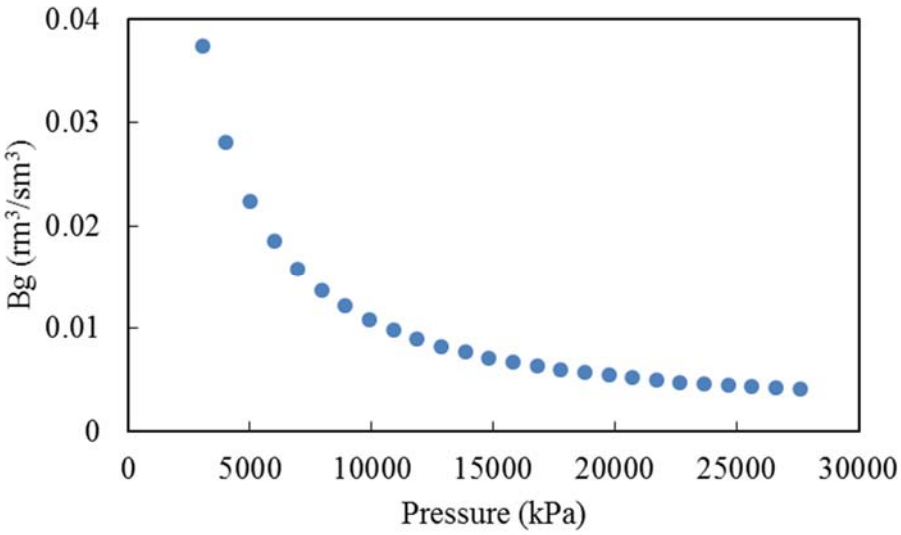

Figure C-2. Gas formation volume factor generated from commercial PVT simulator.